THE ASTROPHYSICAL JOURNAL, 502:16–47, 1998 July 20
© 1998. The American Astronomical Society. All rights reserved. Printed in U.S.A.

REOBSERVATION OF CLOSE QSO GROUPS: THE SIZE EVOLUTION AND SHAPE OF Lyα FOREST ABSORBERS[1]

ARLIN P. S. CROTTS[2] AND YIHU FANG
Department of Astronomy, Columbia University, 538 West 120th Street, New York, NY 10027; arlin@astro.columbia.edu, fang@astro.columbia.edu
Received 1996 December 30; accepted 1998 March 2

ABSTRACT

In order to study the size and shape of the absorbers that lie in front of the QSOs, in particular the Lyα forest, we present an analysis of 785 absorption lines in the spectra of five QSOs in close groupings: a pair (LB 9605: 1517+2357 at $z = 1.834$ and LB 9612: 1517+2356 at $z = 1.903$, with a separation of 102″ between them) and a triplet (KP 76: 1623+2651A at $z = 2.467$, KP 77: 1623+2653 at $z = 2.526$, and KP 78: 1623+2651B at $z = 2.605$, with separations of 127″, 147″, and 177″ between pairs 76:78, 76:77, and 77:78, respectively). Both of these QSO groups have been observed before, but these data represent a drastic increase in signal-to-noise ratio and/or wavelength coverage over earlier data and provide a qualitatively different view of the nature of the absorbers. The pair samples a scale critical in determining the size upper bound of Lyα absorbers, with significant leverage in redshift compared to previous studies. In the case of the triplet, this represents the spatially densest sample of Lyα forest absorbers ever studied and an almost ideally suited probe of the shape of absorbers. We observe a significant number of Lyα lines in common between the triplet sight lines, for lines stronger than rest equivalent width $W_0 > 0.4$ Å (and no detected metal lines) and velocity differences up to 200 km s^{-1}, corresponding to a two-point correlation function $\xi = 1.88^{+0.78}_{-0.50}$ on scales of 0.5–0.8 h^{-1} Mpc with $\langle z \rangle = 2.14$ and inconsistent at the 99.999% level with the absence of any clustering. These data also show that a significant fraction of the $W_0 > 0.4$ Å Lyα forest absorbers spans all three sight lines to the KP triplet, indicating that the strong-lined absorbers are consistent with nearly round shapes, chosen from a range of possible cylinders of different elongations. This may be inconsistent with results from hydrodynamic/gravitational simulations of H I in the early Universe, indicating that the theoretical counterparts of Lyα forest clouds are long and filamentary. Furthermore, there is a probable correlation of W_0 with Δv suggestive of the clouds being flattened and expanding with the Hubble flow in their long dimension, as would be indicative of sheets or filaments. This is supported by the uniformity of line strengths between the three sight lines for $W_0 > 0.4$ Å. We conclude, tentatively, that the $W_0 > 0.4$ Å Lyα forest objects are sheetlike. In contrast, the weaker lines, 0.2 Å $> W_0 >$ 0.4 Å, show no evidence of spanning the sight lines of these groups but have sizes significantly larger than the luminous portions of galaxies and C IV absorbers as revealed by closer separation QSO pairs. When the LB sight-line pair is included with other pairs at different redshifts and sight-line separations, one finds no strong evidence for evolution of Lyα absorber size with redshift. We also show that there is no evidence of large-scale structure in the Lyα forest consistent with ionization of H II by foreground QSOs as seen in the spectrum of background QSOs (the "foreground proximity effect"). Finally, we see a marginal detection of the sight-line two-point cross-correlation function for C IV lines $\xi = 2.05^{+1.82}_{-1.21}$ over scales of 0.5–1 h^{-1} Mpc. This is significantly weaker than ξ measured by autocorrelation along single sight lines for 200 km s$^{-1} < \Delta v <$ 600 km s^{-1}, suggesting that most of the latter signal may be due to the internal motions within absorbers that are smaller than 0.5 h^{-1} Mpc.

Subject headings: early universe — galaxies: distances and redshifts — large-scale structure of universe — quasars: absorption lines

1. INTRODUCTION

The past several years have seen rapid advances in our understanding of the Lyα forest. In part progress is based on the unprecedented spectroscopic capabilities of the Hubble and Keck telescopes, but advances have also been made using 4 m class telescopes in measuring the size of the clouds. The size and shape is crucial in establishing the spatial number density of the cloud population, the ionization state of the absorbers, their mass, and hence their contribution to the mass density of the Universe. Beyond more uncertain lensed QSO Lyα size limits (Foltz et al. 1984; Smette et al. 1992, 1995), the first definite indication of large absorber size came from observations of the 9″.5 separation, $z = 2.050$ QSO pair 1343+2640A/B (corresponding to a sight-line separation of 39–40 h^{-1} kpc proper distance, with $h = H_0/100$ km s^{-1} Mpc^{-1} and $q_0 = \frac{1}{2}$), indicating an absorber radius of 100–200 h^{-1} kpc (Crotts et al. 1994, hereafter Paper I; Bechtold et al. 1994, hereafter Paper II; Dinshaw et al. 1994). Subsequent observations of the lower redshift pair Q0107−0234/0107−0235 ($z = 0.952$, 0.956, separation = 301–364 h^{-1} kpc proper distance) suggested an even larger absorber size, and at lower redshift (Dinshaw et al. 1995). A treatment of previously published, higher redshift pairs (Shaver & Robertson 1983; Crotts 1989; Elowitz, Green, & Impey 1995) at separations larger than that of 1343+2640 revealed that absorbers must be either

[1] Based in part on observations made with the NASA/ESA *Hubble Space Telescope*, obtained from the data archive at the Space Telescope Science Institute, which is operated by AURA, Inc., under NASA contract NAS 5-26555.

[2] Guest observer at the Kitt Peak National Observatory, National Optical Astronomy Observatories, operated by AURA, Inc., for the NSF.

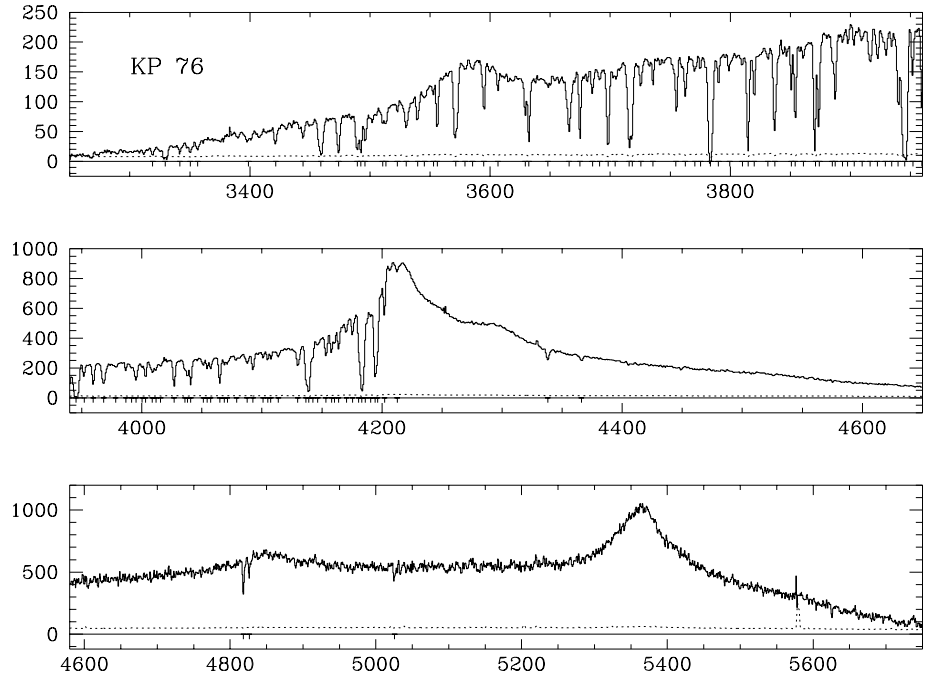

FIG. 1.—Spectrum (in units proportional to photoelectrons as a function of wavelength in Å) for Q1623+2651A (KP 76). The detected absorption lines are indicated by tick marks extending downward from the "counts = 0" line, and the dashed line indicates the standard deviation in counts per wavelength bin (typically 0.76 Å bin^{-1} in the top two panels and 0.72 Å bin^{-1} in the bottom panel).

nonspherical, clustered, or drawn from a distribution that is nonuniform in radius (Fang et al. 1996; hereafter Paper III) and also indicated the need for further data, either for these pairs or for new ones (yet to be discovered). This approach is exploited in the current work, in § 4.4.

The sizes of the absorbers imply that they contain a significant fraction of the baryons in the Universe (Fang & Crotts 1994; Rauch & Haehnelt 1996; Paper III). Thus, they might be analyzed in detail using hydrodynamic/gravitational simulations of the early Universe (Zhang, Anninos, & Norman 1995; Katz et al. 1996; Miralda-Escudé et al. 1996). Indeed, the size of the absorbers is key to identifying the corresponding objects in the simulations (see, e.g., Cen et al. 1994, dealing with ~20 kpc proper diameter clouds, in contrast to Miralda-Escudé et al. 1996, dealing with clouds 100 kpc wide and 1 Mpc long). One outcome of these simulations is also the possibility of predicting the shape of the clouds, which can be compared to QSO triplet data to provide a crucial test of the models, in § 4.5. Paper III also suggested that the shape of Lyα clouds

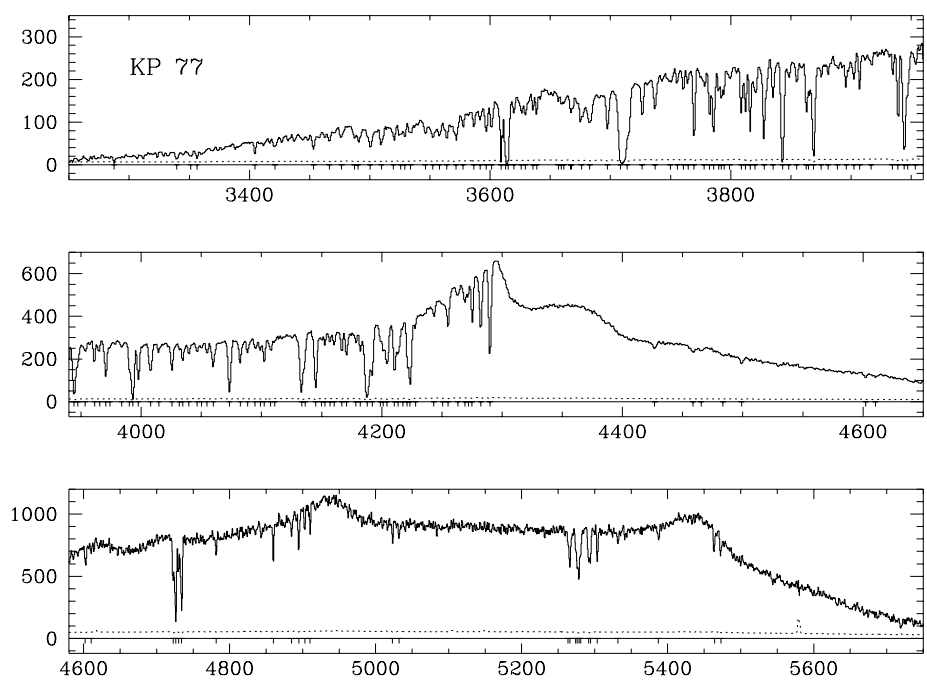

FIG. 2.—Spectrum for Q1623+2653 (KP 77), shown as for Fig. 1

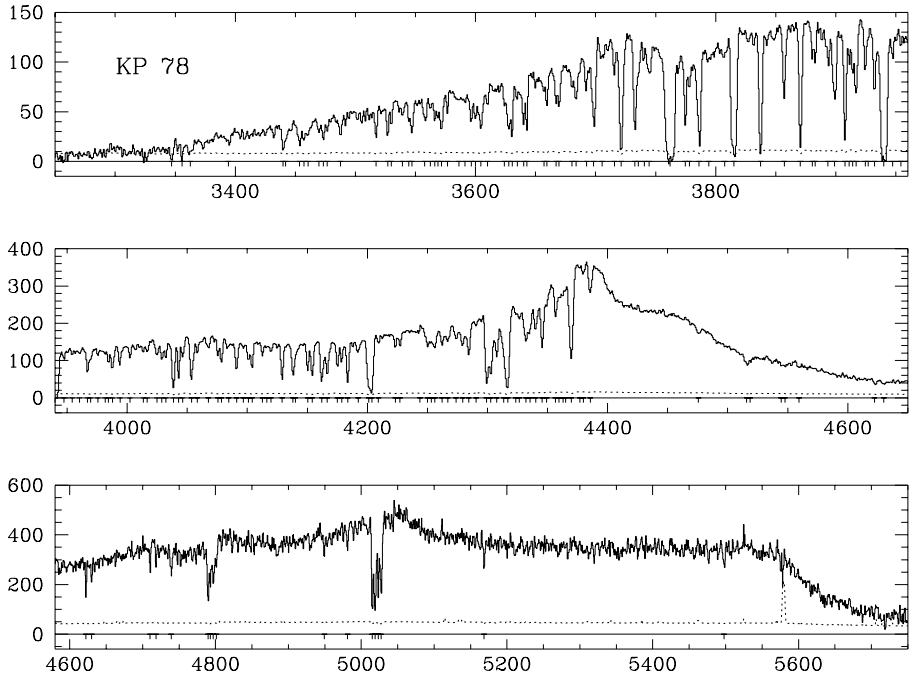

FIG. 3.—Spectrum for Q1623+265B (KP 78), shown as for Fig. 1

might be studied directly using QSO triplets. We present a measure of the absorber shape using triple sight lines in order to facilitate this comparison.

Several theoretical papers have touched or even concentrated on structure on small scales in the Lyα forest as measured by double sight lines. Charlton et al. (1995) suggest a number of tests sensitive to the shape of Lyα clouds probed by pairs of sight lines. These include a test of the correlation of the two neutral hydrogen column densities ($N_{\rm H\,I}$) in the case in which lines in different sight lines correspond in redshift, a test based on $N_{\rm H\,I}$ of the detected line in the case of an anticoincidence, in which only one line is detected at a given redshift, and a method for learning about the velocity field in the clouds by measuring the velocity differences between sight lines. These tests are constructed for comparison to idealized models of cloud shape and kinematics. Miralda-Escudé et al. (1996) perform a detailed hydrodynamical/gravitational numerical simulation of collapsing structure and gas reaction. For sight-line pairs passing through their model's volume, they calculate a

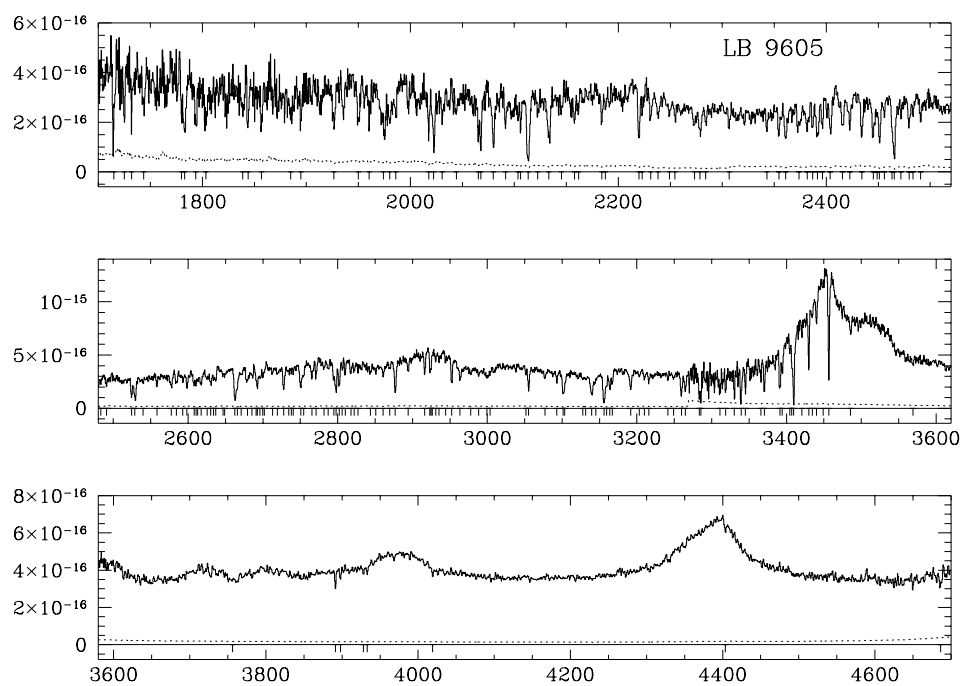

FIG. 4.—Spectrum for 1517+2357 (LB 9605), flux calibrated in units of ergs s^{-1} cm^{-1}, but otherwise shown as for Fig. 1. The wavelength interval per bin ranges from 0.36 Å below 2230 Å, to 0.51 Å for 2230 Å $< \lambda <$ 3270 Å, 0.49 Å for 3270 Å $< \lambda <$ 3594 Å, and 0.76 Å above 3594 Å.

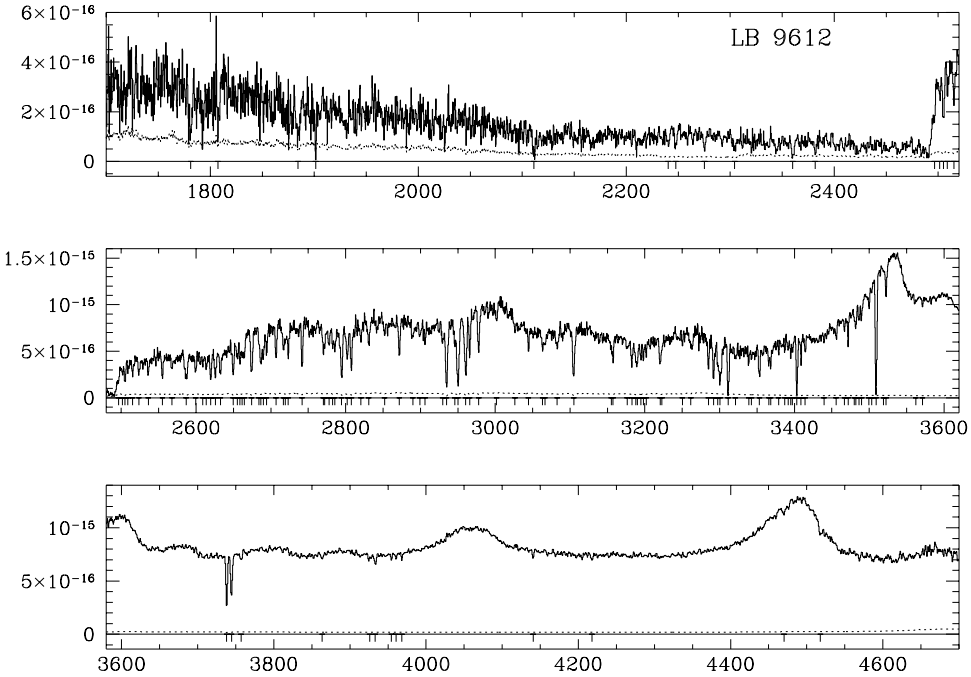

FIG. 5.—Spectrum for 1517+2357 (LB 9612), shown as for Fig. 4

correlation coefficient describing the similarity of absorption between sight lines as a function of transverse spatial separation and line-of-sight velocity difference. Cen & Simcoe (1997) investigate the shapes of clouds within simulations like those of Miralda-Escudé et al., calculating the shapes of clouds at different density contrast levels as well as their effective size. They propose a test based on the correlation between velocity differences between coincident lines versus the sight-line separation for pairs. They also present the spatial two-point correlation function for Lyα clouds of various densities (and presumably line strengths) and study the function's redshift evolution and consider statistics based upon whether absorption lines produced by sight lines passing through their model volume arise in identical or different clouds (which is difficult to test empirically in absorption spectra). Charlton et al. (1997) study model simulations (Zhang et al. 1995) analogous to those of Miralda-Escudé et al. and Cen & Simcoe. They compute size and shape measures analogous to those treated empirically in Paper III, including the variation of inferred spherical (or disklike) cloud size as a function of pair sight-line separation, and the related statistic of line coincidence/anticoincidence ratio as a function of sight-line separation. They also recast the tests from Charlton et al. (1995) in terms in this simulation, as opposed to simplified cloud models. We will apply several of the preceding tests, as well as others that we develop, in § 4.8.

Multiple sight lines are also highly valuable in probing large-scale structure, in that sight lines separated by transverse distances smaller than the structure should show large correlations with each other on these scales, since they pierce the same features. This remedies the problems of searching for voids with single sight lines (Carswell & Rees 1987; Crotts 1987; Duncan, Ostriker, & Bajtlik 1989; Rauch et al. 1992) because multiple, well-sampled sight lines can provide a stronger test for voids by placing more absorbers in a void-sized volume than could possibly be obtained along a single sight line. We study this in § 4.3. Furthermore, the effect of a foreground QSO upon the H I distribution in front of another QSO should be significant if the physics of the "proximity effect" (Bajtlik, Duncan, & Ostriker 1989) is as simple as supposed. Some data exist on the foreground QSO proximity effect (Crotts 1989; Dobrzycki & Bechtold 1991; Fernández-Soto et al. 1995), but they are inconclusive and could easily be improved, as in § 4.2. Finally, large-scale structure can also be sought in the metal-line system distribution, and by cross-correlating multiple sight lines one circumvents the possible ambiguity between internal velocity structure caused by motions within a single absorber and true spatial clustering of spatially distinct objects. These problems are addressed in § 4.9.

2. OBSERVATIONS

Observations of all five QSOs were performed using the Ritchey-Chrétien (RC) Spectrograph and T2KB CCD on the Kitt Peak National Observatory's 4 m telescope on UT 1995 June 1–4, using the BL-420 and BL-450 gratings in second order for the 3170–4720 Å, 1.7 Å FWHM resolution setup and 4450–5750 Å, 1.4 Å FWHM resolution setup, respectively. Wavelengths are reduced to the vacuum heliocentric frame. For the Q1623+2651A, 1623+2653, 1623+2651B data (KP 76, 77, and 78 respectively), spectrophotometric calibration was too uncertain to use. *Hubble Space Telescope* (*HST*) observations of 1517+2356/1517+2357 (LB 9605 and LB 9612 respectively) were made using the Faint Object Spectrograph G190H and G270H setups as part of program GO 5320 of Foltz et al. (1994). Data were also obtained on LB 9605 and 9612 UT 1992 April 29–30 by Elowitz et al. (1995) at the KPNO 4 m telescope with the RC Spectrograph at 3210–3590 Å, and they kindly let us coadd their data with ours. This involved recalibrating the wavelength scale, as there appeared large shifts with respect to both the 1995 KPNO and *HST* wavelengths. This was accomplished in four ways: by reidentify-

ing lines in the ThAr comparison spectrum accompanying the 1992 KPNO data and by cross-correlating the overlapping portions of the QSO spectra in the *HST* and 1995 KPNO data with the 1992 KPNO data (and each other), as well as with the night sky spectra from the 1992 and 1995 KPNO data sets. These show disagreements as large as 60 km s^{-1}, so that over the region 3270–3340 Å, the wavelength calibration might be uncertain by amounts as large as this. The resulting spectra, for KP 76, 77, and 78, are shown in Figures 1, 2, and 3, and for LB 9605/9612 in Figures 4 and 5.

3. ANALYSIS

Continua were calculated and lines detected, deblended, and assigned identifications according to Crotts (1989). Deblending was performed using multiple Gaussian fits instead of Voigt profiles in nearly all cases, with the exception of resolved lines. We use a lower than usual signal-to-noise ratio (S/N) cutoff of 3.5 σ for line detections. We are confident of this approach because we are able to check our results for KP 77 against a high-S/N Keck HIRES spectrum of the object, the highest S/N part of a larger sample collected for the triplet (Crotts, Burles, & Tytler 1997). At a 3.5 σ cutoff for the KPNO data, no false detections are found over the 3900–5700 Å overlap between the two data sets. In fact the KPNO 4 m observations do a good job of detecting all obvious lines in the Keck spectrum (except for some very weak lines in the red KPNO 4 m spectrum past 4700 Å), while, of course, not resolving very close lines. We are fairly confident of our line lists, therefore, and expect approximately four lines out of our 785 to be false detections due to statistical fluctuations.

3.1. *Absorption Line Identification*

We try to be complete as possible in identifying metal-line systems, since stray metal lines might contaminate the statistical properties of Lyα samples, particularly if metal-line systems are redshift correlated. We follow the procedure of Crotts (1989) and list all "definite," "probable," and "possible" systems (the later denoted by " ? "), thereby dividing the systems into classes by probability of being reproduced in a random line list having the same global distribution as real QSO absorption lines.

We identify the following metal-line and Lyman series absorption line systems, detailed in the line lists (Tables 1–5) and listed by QSO below.

3.1.1. *KP 76*

This QSO is surprisingly lacking in absorption lines and systems. Only two well-established metal-containing systems are seen:

z_{ab} = *2.11226*.—This system shows strong Lyα, C IV, and Si III, as well as a firm Si IV doublet, plus Si II λ1260 and C II λ1334. Four of these eight lines occur beyond the Lyα forest.

z_{ab} = *2.24563*.—Very strong Lyα and Lyβ compose this system, along with weak C IV λ1548, Si III and C I λ1277. Lyα is significantly offset from the other lines, suggesting that it is contaminated by another line.

z_{ab} = *1.93778?, 2.40484?, and 2.44125?*.—KP 76 shows two Lyα/Lyβ pairs at $z = 2.40484$ and 2.44125, both with much weaker associated Si III λ1206, but it shows no detected C IV. There is a similar system at $z = 1.93778$, but Lyβ is below the short wavelength limit.

3.1.2. *KP 77*

z_{ab} = *0.88720*.—This is a strong system marked by many lines redward of the Lyα forest. It is peculiar that the Mn II lines are offset several hundred km s^{-1} from the five Fe II and four Mg II and Mg I lines. The Mg II doublet is mixed into a complex of structure near λ5285, but is the strongest contribution to this complex.

z_{ab} = *2.40060*.—Lyα is strong, as is C IV in this system, although the λ1550 line is confused with the Mg II doublet at $z_{ab} = 0.88720$. Weaker Lyβ, Si III λ1206, and a possible O VI doublet also support the system.

z_{ab} = *2.40602?*.—Further structure in the complex at 5285 Å is explained by a C IV doublet at $z_{ab} \approx 2.406$. A strong Lyα line sits at slightly higher redshift. The exact redshift of this system will benefit from higher resolution data on the complex mixing this and the last two systems.

z_{ab} = *1.87952, 1.97331, 2.05050, 2.05380, 2.16128, 2.24455 and 2.52900*.—These are all examples of C IV doublets appearing redward of the Lyα emission line, accompanied by strong Lyα at the same redshift. The $z_{ab} = 1.97331$ system also shows possible Si III λ1206. The $z_{ab} = 2.053$ C IV doublet's redshift sits on the blue wing of the corresponding Lyα line. The C IV doublet at $z_{ab} = 2.1616$ is blended with other lines and hence is less certain. The $z_{ab} = 2.52900$ system is at high enough redshift so that Lyβ and possible Fe lines are also detected.

z_{ab} = *2.44490 and 1.67130?*.—These are Lyman series systems with weak C IV λ1548. The $z_{ab} = 2.44490$ system is more definite having Lyβ and possible Lyγ as well as Lyα (the only Lyman series line at $z_{ab} = 1.67130$ appearing above the short wavelength cutoff).

z_{ab} = *2.40966?, 2.46345?, and 2.47424?*.—These are strong Lyα/Lyβ pairs, without other supporting lines.

3.1.3. *KP 78*

z_{ab} = *2.09428*.—This is a very strong, probably damped, Lyα absorber with strong detections of the C IV and Si IV doublets, Si III λ1206, C II λ1334, weaker Al II λ1670 and probable contributions from Si II λ1260 and Fe II λ1122. The Lyα centroid is offset about 80 km/s from the other lines.

z_{ab} = *2.23925*.—This system is defined by strong C IV and Si IV doublets as well as C II λ1334, plus possible contributions from C I λ1277 and Fe III λ1122. It shares a strong Lyα line with $z_{ab} = 2.24173$, below.

z_{ab} = *2.24173*.—As well as very strong Lyα and C IV, this system shows C I λ1277, C II λ1334, the N V doublet, Si IV λ1393, Si III λ1206, the strongest lines of Si II ($\lambda\lambda$1260, 1304, and 1190), plus possible Fe III λ1122.

z_{ab} = *2.55106*.—This system shows strong Lyα, Lyβ, Lyγ, Si III, and weak C IV λ1548, Si IV $\lambda\lambda$1393, 1402, Si II ($\lambda\lambda$1260, 1304, and 1190) and possible C II $\lambda\lambda$1036, 1334, C III λ977 and Fe III λ1122.

z_{ab} = *2.57482*.—There is no C IV detected, but there is moderate Lyα, Lyβ, Lyγ, and Lyδ. Also possible are Si III, Si IV λ1393, Fe III λ1122, and Fe II λ1144.

z_{ab} = *1.98490, 2.04240, and 2.09592*.—These are all C IV doublets outside of the Lyα forest plus strong Lyα lines. The $z = 1.98490$ system also contains Lyβ. The redshift 2.09592 system shares Lyα with 2.09428 above and probably also shows Si III.

z_{ab} = *1.93770? and 2.06117?*.—These are possible systems consisting of weak C IV λ1548 outside of the forest plus strong Lyα.

TABLE 1

ABSORPTION LINES IN KP 76

λ_{vac}(mean)	λ Range	W_{obs}	S/N	Comments
3319.05.....	3317.83–3320.11	1.26	5.08	
3329.50.....	3326.19–3333.03	3.65	11.21	Lyβ at $z_{ab} = 2.24601$
3341.56.....	3339.87–3342.91	0.83	3.98	
3350.38.....	3348.99–3352.03	1.57	7.75	
3356.49.....	3355.07–3358.11	1.00	5.57	
3398.83.....	3396.11–3401.44	0.70	4.26	
3421.52.....	3418.92–3423.48	1.08	8.95	
3444.22.....	3442.48–3446.28	0.80	7.87	
3459.10.....	3455.40–3463.00	3.48	28.51	
3473.76.....	3470.60–3476.68	2.39	23.76	
3489.34.....	3487.32–3490.94	2.14	14.90	
3492.46.....	3490.94–3494.16	2.02	13.87	Lyβ at $z_{ab} = 2.40488$?
3495.76.....	3494.93–3497.97	1.39	10.24	
3510.53.....	3508.61–3511.75	0.67	6.81	
3513.17.....	3511.75–3515.45	0.78	7.97	
3522.83.....	3521.53–3523.81	0.28	4.63	
3530.28.....	3526.85–3533.69	1.39	15.66	Lyβ at $z_{ab} = 2.44175$?
3539.68.....	3537.49–3542.05	0.71	9.91	
3545.31.....	3543.90–3546.70	0.29	4.01	Si III λ1206 at $z_{ab} = 1.93850$?
3552.88.....	3551.17–3554.21	0.25	4.36	
3556.04.....	3554.21–3558.01	1.13	19.63	
3571.37.....	3567.89–3574.73	3.00	51.07	Lyα at $z_{ab} = 1.93778$?
3579.17.....	3577.00–3581.30	0.26	3.66	
3585.40.....	3583.85–3586.89	0.28	6.28	
3594.73.....	3592.22–3596.78	1.11	22.26	
3606.45.....	3605.14–3608.18	0.33	7.07	
3629.26.....	3627.18–3630.27	0.88	12.23	
3632.31.....	3630.27–3634.78	1.79	24.88	
3648.17.....	3646.94–3649.22	0.36	7.67	
3665.74.....	3662.14–3669.74	2.08	28.54	
3674.90.....	3672.78–3677.34	1.40	25.36	
3685.26.....	3683.42–3687.23	0.36	6.96	
3691.25.....	3689.51–3692.55	0.12	4.67	
3698.20.....	3695.59–3700.91	2.17	38.95	
3704.03.....	3701.67–3706.23	0.38	6.57	
3715.88.....	3712.31–3717.49	2.62	41.12	
3718.34.....	3717.49–3720.67	1.38	21.62	
3725.59.....	3723.71–3727.51	0.49	10.04	
3735.58.....	3734.35–3737.39	0.38	8.20	
3754.77.....	3751.83–3757.15	1.15	20.50	Si III λ1206 at $z_{ab} = 2.11212$
3762.44.....	3758.67–3764.75	0.79	13.26	
3770.51.....	3768.55–3772.35	0.22	4.55	
3775.13.....	3773.20–3776.00	0.22	4.61	
3783.50.....	3779.95–3787.56	4.32	75.49	Lyα at $z_{ab} = 2.11228$
3790.19.....	3788.32–3792.12	0.33	6.83	
3799.45.....	3797.44–3801.24	0.23	4.78	
3810.12.....	3808.50–3811.71	0.24	4.99	
3814.78.....	3812.64–3817.20	2.06	42.91	
3819.87.....	3817.96–3821.76	0.63	13.01	
3831.23.....	3829.62–3833.84	0.21	4.38	
3837.03.....	3834.68–3841.52	1.88	32.37	
3850.95.....	3849.12–3852.16	0.42	9.75	
3854.04.....	3852.16–3855.96	1.14	26.00	
3860.88.....	3859.76–3862.04	0.18	4.98	
3870.98.....	3868.12–3872.85	2.21	42.77	
3874.25.....	3872.85–3875.72	1.52	29.51	
3884.97.....	3883.33–3885.54	0.37	7.69	
3887.40.....	3885.54–3889.41	1.23	25.17	
3893.54.....	3892.01–3895.05	0.13	3.99	
3897.72.....	3897.01–3899.29	0.20	6.01	
3903.20.....	3901.57–3904.61	0.26	6.83	
3909.79.....	3907.65–3910.69	0.23	5.90	
3916.30.....	3913.73–3919.05	0.61	12.57	Si III λ1206 at $z_{ab} = 2.24600$
3922.41.....	3920.57–3924.37	0.36	8.80	
3929.23.....	3926.65–3931.21	0.33	7.19	
3934.34.....	3932.55–3936.15	0.16	3.62	Si II λ1260 at $z_{ab} = 2.11198$
3939.80.....	3938.05–3940.56	1.19	19.29	
3945.20.....	3940.56–3948.69	5.84	94.70	Lyα at $z_{ab} = 2.24529$
3952.09.....	3950.21–3953.25	0.40	10.39	
3959.61.....	3957.05–3961.61	1.18	28.46	
3968.25.....	3964.65–3972.25	1.96	39.03	
3978.20.....	3975.30–3979.86	0.20	4.59	
3986.74.....	3985.18–3988.22	0.18	4.92	

TABLE 1—*Continued*

λ_{vac}(mean)	λ Range	W_{obs}	S/N	Comments
3991.43.....	3989.74–3992.15	0.33	6.02	
3995.08.....	3992.15–3997.34	1.36	24.71	
4000.30.....	3999.14–4000.89	0.23	5.59	
4003.03.....	4000.89–4004.94	0.84	20.22	
4008.79.....	4006.46–4010.80	0.95	17.57	
4011.85.....	4010.80–4013.30	0.49	9.18	
4015.61.....	4014.06–4017.10	0.13	3.57	
4026.90.....	4024.70–4029.26	1.44	37.18	
4036.02.....	4033.82–4037.08	0.74	13.36	
4038.07.....	4037.08–4038.92	0.69	12.44	
4040.72.....	4038.92–4042.94	1.47	26.52	
4051.23.....	4049.02–4052.82	0.19	4.91	
4054.42.....	4052.82–4055.63	0.43	8.90	
4057.25.....	4055.63–4059.66	0.58	11.92	
4064.97.....	4062.70–4067.26	1.20	30.32	
4068.60.....	4067.26–4069.63	0.30	6.21	
4071.21.....	4069.63–4073.35	0.45	9.52	
4078.98.....	4077.15–4080.19	0.22	3.71	
4087.73.....	4084.75–4089.84	0.65	12.38	
4092.52.....	4089.84–4094.63	0.83	15.78	
4100.97.....	4099.95–4102.23	0.13	4.60	
4104.86.....	4103.75–4106.03	0.22	8.27	
4107.39.....	4106.03–4109.07	0.20	6.38	
4113.71.....	4111.35–4115.91	0.26	7.42	Si III λ1206 at z_{ab} = 2.40438?
4129.79.....	4125.79–4132.63	0.87	21.05	
4136.64.....	4134.91–4137.33	1.26	32.32	
4139.13.....	4137.33–4141.91	2.86	73.43	Lyα at z_{ab} = 2.40481?
4142.33.....	4141.91–4143.27	0.43	10.99	
4146.47.....	4144.80–4148.49	0.16	5.61	C I λ1277 at z_{ab} = 2.24642
4153.24.....	4151.63–4155.43	0.45	16.00	C II λ1334 at z_{ab} = 2.11213, part Si III λ1206 at z_{ab} = 2.441?
4157.93.....	4156.19–4159.49	0.57	17.92	
4160.34.....	4159.49–4161.51	0.31	9.75	
4163.89.....	4162.27–4166.08	0.41	15.49	
4170.53.....	4168.36–4171.40	0.14	5.74	
4175.51.....	4173.68–4177.48	0.26	10.62	
4180.60.....	4179.00–4181.15	0.89	29.40	
4183.17.....	4181.15–4185.83	3.29	108.69	Lyα at z_{ab} = 2.44104?
4186.17.....	4185.83–4187.73	0.20	6.61	
4190.49.....	4187.73–4191.05	0.35	10.09	
4194.31.....	4191.05–4195.67	2.05	58.26	
4196.28.....	4195.67–4199.86	0.91	25.91	
4202.12.....	4199.86–4204.08	0.58	16.41	
4212.70.....	4210.92–4213.96	0.07	4.18	
4338.04.....	4335.57–4340.89	0.61	16.58	Si IV λ1393 at z_{ab} = 2.11248
4366.05.....	4363.70–4368.26	0.26	6.68	Si IV λ1402 at z_{ab} = 2.11245
4818.38.....	4816.07–4821.87	1.13	13.04	C IV λ1548 at z_{ab} = 2.11224
4826.44.....	4824.04–4829.11	0.57	6.99	C IV λ1550 at z_{ab} = 2.11228
5025.72.....	5023.22–5027.56	0.45	5.44	C IV λ1548 at z_{ab} = 2.24617

z_{ab} = 2.36526?, 2.42738?, 2.44138?, 2.45570?, 2.45801?, 2.53649?, 2.53941, 2.54356?, 2.54879?, 2.56715, and 2.59458?.—These are "possible" and probable Lyα, Lyβ pairs. The z_{ab} = 2.53941 and 2.56715 also show Lyγ. The 2.59458 system is only suspected. If this line is Lyα, one should expect to see Lyβ at 3687.04 Å. There is a marginally detected line there, at about W_{obs} = 0.3 Å, so this is plausibly consistent with λ4369.82 being Lyα.

3.1.4. *LB 9605*

z_{ab} = −0.00055.—This Galactic system is marked by the Mg II doublet, Ca II λ3934, Mg I λ2852, Al II λ1670, the four strongest lines of Fe II, two of Fe I, and three of Mn II. Note that a similar system is seen in LB 9612.

z_{ab} = 0.73825—This is composed of Lyα, β and γ, plus the C IV doublet and Si IV λ1393. All of these lines fall in the forest but appear to be unambiguous.

z_{ab} = 1.02780.—This shows Lyα, Lyβ, Lyγ, and Lyδ, the C IV doublet, Si IV λ1393, Si II λ1206, C III λ977, and a likely O VI doublet. Most of these lines are blended with components of other systems, and none land beyond the forest. (None would be expected.)

z_{ab} = 1.51350.—A weak C IV doublet lands outside the forest, while the other lines consist of Lyα, probable Lyβ, Si II λ1260, C I λ1277, and possible Fe II λ1144, Fe III λ1122, and the O VI doublet.

z_{ab} = 1.59590.—This is a strong system consisting of the first 10 Lyman series lines plus C IV λ1548. The absence of a Ly limit feature ($\tau < 0.1$) implies $N_{\rm H\,I} \lesssim 1.5 \times 10^{16}$ cm^{-2}.

z_{ab} = 0.41063.—This is a probable C IV doublet in the forest associated with a strong Lyα line.

z_{ab} = 1.19268.—This is a probable Lyα/Lyβ pair with a C IV λ1548 line beyond the forest.

z_{ab} = 1.80465.—Another strong system of the first seven Lyman series lines, it shows no metal lines.

z_{ab} = 1.01602, 1.07973, 1.30150, 1.60295, 1.68573, 1.72400?, 1.84560.—These consist of at least the first three Lyman series lines in a pure hydrogen system. Additionally, one finds Lyδ for z_{ab} = 1.30150, 1.60295, 1.07973, and 1.84560, and Lyϵ for z_{ab} = 1.07973. There is a possible C IV

TABLE 2

ABSORPTION LINES IN KP 77

λ_{vac}(mean)	λ Range	W_{obs}	S/N	Comments
3247.00.....	3241.50–3254.36	5.87	9.02	Lyα at $z_{ab} = 1.67095$?
3287.58.....	3285.98–3289.18	1.29	7.18	
3339.64.....	3337.54–3342.08	1.29	6.29	
3351.14.....	3349.64–3352.66	1.23	6.66	Part Lyγ at $z_{ab} = 2.4453$ (<0.3 Å)
3356.40.....	3354.93–3357.96	1.15	6.40	
3404.59.....	3402.57–3406.35	0.90	8.44	
3421.17.....	3419.21–3422.99	0.59	5.60	
3453.35.....	3450.97–3455.51	0.86	8.77	
3466.38.....	3464.58–3468.36	0.46	5.59	
3476.57.....	3474.41–3478.95	0.65	7.92	
3487.22.....	3485.75–3487.96	0.64	5.92	Lyβ at $z_{ab} = 2.39977$
3490.17.....	3487.96–3493.32	1.48	13.71	
3500.37.....	3497.10–3503.90	1.48	14.45	Lyα at $z_{ab} = 1.87937$, part Lyβ at $z_{ab} = 2.40966$
3509.78.....	3507.68–3512.22	1.06	13.03	O VI λ1031 at $z_{ab} = 2.40199$?
3519.64.....	3518.27–3522.05	0.35	4.50	
3525.56.....	3524.20–3527.82	0.98	14.69	
3529.20.....	3527.82–3531.35	0.60	8.97	O VI λ1037 at $z_{ab} = 2.40126$?
3533.94.....	3531.35–3532.97	0.72	10.77	Lyβ at $z_{ab} = 2.44532$
3546.28.....	3544.74–3547.76	0.71	10.15	
3552.50.....	3550.03–3554.57	1.78	20.58	Lyβ at $z_{ab} = 2.46341$?
3557.89.....	3556.84–3559.10	0.96	14.71	
3563.93.....	3562.13–3565.91	1.51	19.97	Lyβ at $z_{ab} = 2.47456$?
3571.65.....	3568.94–3574.23	1.86	24.61	
3577.52.....	3576.50–3579.52	0.30	5.29	
3586.58.....	3584.82–3588.60	0.42	7.16	Si III λ1206 at $z_{ab} = 1.97271$
3591.81.....	3590.11–3593.13	0.20	3.74	
3596.91.....	3594.65–3599.18	0.84	14.28	
3601.17.....	3599.18–3602.96	0.65	12.03	
3609.22.....	3606.74–3611.13	2.06	23.44	Artifact
3612.94.....	3611.13–3613.90	1.96	22.31	
3614.96.....	3613.90–3617.33	2.15	24.45	Lyα at $z_{ab} = 1.97364$
3619.79.....	3618.13–3621.33	0.39	4.41	Lyβ at $z_{ab} = 2.52902$
3625.85.....	3624.89–3627.13	0.51	7.77	
3629.43.....	3627.13–3630.94	0.91	13.97	
3635.67.....	3634.72–3636.99	0.18	4.28	
3638.80.....	3636.99–3640.02	0.37	7.99	
3656.69.....	3655.10–3658.17	0.17	3.63	
3659.14.....	3658.17–3659.91	0.20	3.62	
3661.25.....	3659.91–3662.70	0.36	6.30	
3667.23.....	3665.73–3670.27	0.53	9.26	
3676.04.....	3673.29–3678.58	0.70	11.12	
3682.77.....	3679.34–3686.15	1.12	16.54	
3697.59.....	3694.46–3700.51	1.33	22.94	
3708.47.....	3704.29–3711.70	5.39	80.89	Lyα at $z_{ab} = 2.05056$
3713.97.....	3711.70–3717.91	3.78	56.71	Lyα at $z_{ab} = 2.05508$
3726.45.....	3723.96–3728.49	0.87	18.58	
3737.13.....	3734.54–3739.84	0.86	17.09	
3749.76.....	3748.15–3751.93	0.44	9.92	
3755.73.....	3754.20–3756.47	0.25	7.38	
3760.82.....	3758.74–3761.77	0.24	6.20	
3764.61.....	3762.52–3765.55	0.23	5.77	
3769.54.....	3767.81–3771.60	1.37	35.88	
3777.99.....	3773.30–3780.51	0.47	8.43	
3782.51.....	3780.67–3783.80	1.08	18.47	
3785.77.....	3783.80–3788.23	1.66	28.36	
3789.97.....	3788.99–3790.84	0.38	6.64	
3792.31.....	3790.84–3793.60	0.65	11.21	
3794.43.....	3793.50–3795.79	0.41	7.18	
3799.15.....	3797.39–3800.59	0.33	5.70	
3808.74.....	3807.14–3810.54	1.03	18.89	
3812.31.....	3810.54–3813.94	1.00	18.51	
3816.16.....	3813.94–3818.47	1.33	21.74	
3820.32.....	3818.47–3823.02	1.06	17.37	
3827.99.....	3824.53–3831.34	1.93	39.05	Part Mg I λ2026 at $z_{ab} = 0.888$
3835.22.....	3833.60–3837.38	0.58	14.54	
3843.07.....	3840.41–3845.70	2.95	76.37	Lyα at $z_{ab} = 2.16128$?
3848.08.....	3846.46–3850.24	0.15	3.66	
3854.75.....	3853.26–3857.05	0.26	6.34	
3862.69.....	3860.83–3864.04	1.12	19.08	
3864.75.....	3864.08–3865.48	0.59	10.06	
3868.96.....	3865.48–3872.17	2.80	47.84	
3875.26.....	3873.68–3876.71	0.16	4.25	
3881.01.....	3879.73–3882.00	0.13	3.91	

TABLE 2—*Continued*

λ_{vac}(mean)	λ Range	W_{obs}	S/N	Comments
3888.76.....	3883.60–3890.30	0.37	8.39	
3896.11.....	3894.10–3898.64	0.37	8.39	
3902.42.....	3900.15–3903.93	0.24	5.99	
3907.29.....	3905.44–3908.47	0.39	10.88	
3916.78.....	3914.52–3918.30	0.16	4.01	
3934.36.....	3933.42–3936.45	0.14	4.05	
3938.99.....	3937.20–3940.98	0.92	24.72	
3944.24.....	3941.74–3946.43	2.56	53.56	Lyα at $z_{ab} = 2.24450$
3947.21.....	3946.43–3949.30	0.91	18.98	
3953.49.....	3951.57–3955.35	0.13	3.52	
3961.25.....	3959.13–3962.91	0.47	12.98	Fe III λ1122 at $z_{ab} = 2.52887$?
3965.67.....	3962.91–3966.94	0.18	5.31	
3970.59.....	3968.21–3973.38	1.37	30.64	
3973.91.....	3973.38–3975.01	0.26	5.77	
3983.81.....	3980.90–3986.20	0.21	4.78	
3990.11.....	3988.62–3990.66	0.75	17.22	
3992.97.....	3990.66–3995.43	3.13	72.43	
3997.69.....	3995.43–3999.97	1.12	27.84	
4007.77.....	4004.50–4010.55	1.32	29.86	
4014.75.....	4012.82–4016.60	0.21	5.45	
4025.53.....	4022.65–4027.95	0.94	22.15	
4031.76.....	4030.97–4032.27	0.15	3.50	
4034.56.....	4032.27–4037.02	0.67	14.21	
4039.68.....	4038.53–4041.56	0.22	6.25	Fe II λ1144 at $z_{ab} = 2.52829$?
4046.53.....	4044.58–4048.93	0.34	8.69	
4050.19.....	4048.93–4052.10	0.18	4.58	
4054.77.....	4052.90–4056.68	0.39	9.96	
4059.97.....	4057.44–4062.73	0.91	21.36	
4073.36.....	4070.29–4076.34	2.17	54.42	
4082.34.....	4079.37–4085.42	0.89	20.28	
4088.44.....	4086.93–4090.71	0.31	8.49	
4094.72.....	4093.74–4096.76	0.12	3.57	
4099.01.....	4097.52–4100.04	0.38	8.09	
4102.34.....	4100.04–4104.32	0.85	18.01	Si III λ1206 at $z_{ab} = 2.40020$
4107.56.....	4105.83–4110.36	0.55	15.16	
4111.01.....	4110.36–4112.60	0.13	3.53	
4133.41.....	4128.52–4136.01	3.25	69.73	Lyα at $z_{ab} = 2.40011$
4136.31.....	4136.01–4138.35	0.37	7.96	C IV λ1548 at $z_{ab} = 1.67169$
4145.02.....	4142.13–4148.94	2.16	53.01	Lyα at $z_{ab} = 2.40966$?
4149.75.....	4148.94–4151.21	0.44	10.46	
4152.88.....	4151.21–4154.23	0.24	7.57	
4156.98.....	4155.74–4158.77	0.17	5.35	
4160.34.....	4158.77–4161.79	0.25	8.22	
4166.65.....	4164.82–4168.60	0.40	11.81	
4170.71.....	4168.60–4173.14	0.55	14.89	
4178.48.....	4176.80–4180.70	0.45	12.15	
4182.18.....	4180.70–4182.81	0.59	11.20	
4187.85.....	4182.81–4191.09	4.70	89.66	Lyα at $z_{ab} = 2.44489$
4192.03.....	4191.09–4194.31	1.37	26.07	
4198.75.....	4198.09–4199.49	0.35	7.22	
4201.15.....	4199.49–4202.13	0.79	16.18	
4204.39.....	4202.13–4206.41	1.80	37.06	
4210.44.....	4208.68–4211.82	1.31	30.78	Lyα at $z_{ab} = 2.46347$?, part NV λ1238 at $z_{ab} = 2.399$
4213.52.....	4211.82–4217.17	1.61	37.96	
4217.49.....	4217.17–4219.26	0.14	3.59	
4220.94.....	4219.26–4221.19	0.36	8.48	
4223.24.....	4221.19–4227.88	2.99	70.28	Lyα at $z_{ab} = 2.47408$?
4228.12.....	4227.88–4229.09	0.16	3.67	
4243.30.....	4241.19–4244.97	0.23	8.59	
4250.65.....	4248.76–4251.41	0.20	5.23	
4254.95.....	4251.41–4257.83	0.91	24.46	
4263.28.....	4260.85–4264.64	0.27	10.81	
4269.02.....	4266.90–4271.02	0.59	19.09	
4271.92.....	4271.02–4272.95	0.26	8.60	
4275.03.....	4273.71–4277.49	0.49	20.30	
4282.32.....	4279.76–4285.05	1.01	39.32	
4289.89.....	4287.32–4292.61	1.53	66.01	Lyα at $z_{ab} = 2.52883$
4426.76.....	4424.95–4428.73	0.21	5.44	Fe II λ2344 at $z_{ab} = 0.88838$
4458.66.....	4456.71–4463.18	0.57	9.48	C IV λ1548 at $z_{ab} = 1.87990$
4465.50.....	4463.18–4468.49	0.29	4.88	C IV λ1550 at $z_{ab} = 1.87952$
4483.60.....	4482.42–4484.69	0.21	4.00	Fe II λ2374 at $z_{ab} = 0.88826$
4499.04.....	4496.79–4502.08	0.39	7.46	Fe II λ2382 at $z_{ab} = 0.88816$
4602.24.....	4601.14–4603.41	0.20	4.06	C IV λ1548 at $z_{ab} = 1.97264$
4610.36.....	4609.46–4610.97	0.16	3.56	C IV λ1550 at $z_{ab} = 1.97294$

TABLE 2—*Continued*

λ_{vac}(mean)	λ Range	W_{obs}	S/N	Comments
4722.70.....	4720.49–4723.82	1.16	11.26	C IV λ1548 at $z_{ab} = 2.05044$
4726.20.....	4723.82–4729.38	2.48	24.08	C IV λ1548 at $z_{ab} = 2.05270$
4730.25.....	4729.38–4731.23	0.68	6.60	C IV λ1550 at $z_{ab} = 2.05025$
4734.12.....	4731.23–4736.42	2.00	19.45	C IV λ1550 at $z_{ab} = 2.05275$
4781.45.....	4779.89–4782.78	0.31	5.80	
4859.91.....	4858.12–4861.74	0.57	10.75	Mn II λ2576 at $z_{ab} = 0.88597$
4884.74.....	4882.75–4886.37	0.29	5.42	Fe II λ2586 at $z_{ab} = 0.88844$
4894.87.....	4892.89–4897.24	0.62	11.48	Mn II λ2594 at $z_{ab} = 0.88663$, part C IV λ1548 at $z_{ab} = 2.1616$
4902.93.....	4900.86–4904.48	0.32	6.37	Fe II λ2600 at $z_{ab} = 0.88562$, part C IV λ1550 at $z_{ab} = 2.1616$
4909.92.....	4907.38–4911.73	0.38	7.11	Mn II λ2606 at $z_{ab} = 0.88375$
5023.13.....	5021.11–5024.73	0.27	5.12	C IV λ1548 at $z_{ab} = 2.24449$
5032.21.....	5030.52–5034.15	0.26	4.79	C IV λ1550 at $z_{ab} = 2.24497$
5265.80.....	5262.33–5269.57	1.11	15.97	C IV λ1548 at $z_{ab} = 2.40124$
5273.76.....	5272.47–5274.29	0.28	3.52	C IV λ1548 at $z_{ab} = 2.40637$?
5277.33.....	5274.29–5280.04	1.88	23.81	Mg II λ2786 at $z_{ab} = 0.88722$, C IV λ1550 at $z_{ab} = 2.401$
5281.42.....	5280.04–5282.61	0.53	6.74	C IV λ1550 at $z_{ab} = 2.40567$?
5292.78.....	5289.13–5296.37	1.40	20.12	Mg II λ2803 at $z_{ab} = 0.88790$
5303.67.....	5302.17–5305.79	0.54	10.48	
5331.72.....	5329.70–5333.32	0.24	4.54	C IV λ1548 at $z_{ab} = 2.44381$
5387.28.....	5384.75–5389.82	0.32	5.49	Mg I λ2852 at $z_{ab} = 0.88831$
5464.10.....	5460.21–5468.51	0.55	7.05	C IV λ1548 at $z_{ab} = 2.52932$
5472.96.....	5468.51–5477.60	0.40	5.49	C IV λ1550 at $z_{ab} = 2.52918$

λ1550 line at $z_{ab} = 1.30142$. The $z_{ab} = 1.72400$ system is more uncertain due to ambiguity in some of its line identifications.

$z_{ab} = 0.70010$?, 0.96730?, 1.16401?, 1.19274?, 1.42858?, 1.55105?, 1.58226?, 1.62531?, 1.68137?, 1.70001?, 1.73948?, 1.74690?, 1.75165?, 1.77245?, 1.78948?, and 1.82251?.—These are possible Lyα/Lyβ pairs; all have strong Lyα. The $z_{ab} = 1.82251$ and 0.96730 systems also show Si III λ1206.

3.1.5. *LB 9612*

$z_{ab} = -0.00040$.—Like LB 9605, this spectrum shows a strong Galactic system. It includes the Ca II and Mg II doublets, Mg I λ2853, Ca I λ2722, Fe I λ2523, and three strong lines of Fe II ($\lambda\lambda$2382, 2586, and 2600). Fe I λ2484 is lost in the Ly break at 2484 Å.

$z_{ab} = 0.25155$?.—Another possible low-redshift system consists of the Mg II doublet and Mg I λ2852, all in the forest.

$z_{ab} = 0.73690$.—This consists of Lyα, Lyβ, Lyγ, and a C IV doublet, all in the forest.

$z_{ab} = 1.05998$.—This system contains C IV and Si IV doublets, Lyα, Lyβ, and possible C I λ1656.

$z_{ab} = 1.12625$.—This shows Lyα, a C IV doublet, Si II λ1393, C I λ1656, and possible N V λ1238, Si III λ1206, and C I λ1277.

$z_{ab} = 1.30090$.—This probable system contains Lyα, β and C III λ977 confused with other systems, Si II λ1260 and, outside the forest, C IV λ1548.

$z_{ab} = 1.41451$.—This is marked by strong Lyα, a C IV doublet (outside the forest), and a Si IV doublet.

$z_{ab} = 1.42671$.—This consists of a strong Lyman series to Ly8, plus C IV λ1548. The system's Lyβ occurs at the Ly break at 2484 Å. Ly6 at 2258 Å is marginally detected.

$z_{ab} = 1.55414$.—This includes Lyα, Lyβ, a C IV doublet, and C II λ1334.

$z_{ab} = 1.72398$.—This is a very strong system with Lyman series lines up to at least Ly10, and probably includes a blend of higher terms in the series. These are associated with an $N_{\rm H\,I} \approx 4 \times 10^{17}$ cm^{-2} determined from the Ly limit drop. Metal lines include C IV λ1548, C III λ977, and C I lines ($\lambda\lambda$1277 and 1656).

$z_{ab} = 1.88690$.—In addition to a Ly series extending to Ly10 and a Ly limit break corresponding to $N_{\rm H\,I} \approx 1 \times 10^{17}$ cm^{-2}, this system shows Si III λ1206, C IV λ1548, and possible C III λ977 and O VI λ1031.

$z_{ab} = 1.75930$ and 1.79961.—These are two Ly series systems extending to Ly7 and Lyε, respectively.

$z_{ab} = 1.43510$?, 1.43964?, 1.62398?, 1.64890?, 1.70809?, and 1.71516?.—These are possible Lyα/Lyβ pairs.

Both LB 9605 and LB 9612 have significantly more identified redshift systems per unit z than do KP 76, 77, and 78, probably because of the greater wavelength coverage of these two spectra. Many of these systems would be unlikely to be recognized in the KP spectra. The consequences of this will be discussed in the next subsection.

3.2. *Lyα Line Sample*

Despite the large number of lines detected at wavelengths shorter than Lyα emission in LB 9605 and 9612, relatively few are caused by unadulterated Lyα absorption, at least below certain wavelengths. This is particularly true for LB 9612, which suffers a nearly complete loss of flux below 2490 Å because of one Ly limit system and a significant drop below 2670 Å because of another. Equally serious, however, is the contamination of a large stretch of spectrum by higher Ly series lines and metal lines, many associated with these two Ly limits. Of the 45 lines between 2490 and 2900 Å, only six are explained by uncontaminated Lyα lines, whereas above 2900 Å only 29% of the lines in the forest can be explained (even in part) by lines other than Lyα. Similar behavior, although not so drastic given the absence of Ly limit systems, is seen in LB 9605. This implies that the only useful sample of Lyα lines for comparing the Lyα distributions in LB 9605 and 9612 is in the wavelength range 2900–3445 Å ($z = 1.39$–1.83, with $\langle z \rangle = 1.62$), roughly the range between Lyβ and Lyα emission. (In practice, we use observed wavelength 2900 Å to the wavelength 1220 Å in the reference frame of the QSO, accounting for infall toward the QSO by up to 1000 km s^{-1}.)

We apply a similar constraint to the KP 76, 77, 78 triplet. In practice we consider those lines with wavelengths of 1020–1220 Å in the reference frame of the QSO, unless

TABLE 3

ABSORPTION LINES IN KP 78

λ_{vac} (mean)	λ Range	W_{obs}	S/N	Comments
3347.05.....	3345.07–3348.85	1.86	4.42	
3355.71.....	3354.14–3357.17	1.59	4.41	
3362.52.....	3360.19–3365.48	1.50	3.53	
3394.26.....	3391.95–3396.49	1.05	4.44	Part Lyδ at $z_{ab} = 2.5739$
3439.71.....	3438.08–3441.00	1.25	5.66	
3441.94.....	3441.00–3443.24	0.92	4.15	Part Lyγ at $z_{ab} = 2.5394$
3453.39.....	3451.69–3455.47	1.77	8.84	Lyγ at $z_{ab} = 2.55091$, part Lyβ at $z_{ab} = 2.3653$?
3457.30.....	3455.47–3458.49	1.15	6.42	
3460.64.....	3458.49–3461.51	0.87	4.81	
3469.66.....	3471.35–3471.06	0.77	4.74	Part Lyγ at $z_{ab} = 2.567$, part C III λ977 at $z_{ab} = 2.5512$
3473.36.....	3471.06–3475.59	1.26	7.78	Part Fe λ1122 at $z_{ab} = 2.0942$
3476.61.....	3475.59–3478.13	0.57	3.55	Lyγ at $z_{ab} = 2.57479$
3487.49.....	3485.71–3489.50	0.77	5.38	
3517.15.....	3515.20–3518.99	1.05	9.06	Part Lyβ at $z_{ab} = 2.4274$?
3526.92.....	3525.03–3528.82	0.98	8.91	
3529.89.....	3528.82–3531.08	0.48	5.49	Lyβ at $z_{ab} = 2.44137$?
3539.24.....	3537.89–3540.91	0.54	5.29	
3544.43.....	3543.18–3545.17	0.54	3.80	Lyβ at $z_{ab} = 2.45555$?
3547.00.....	3545.17–3549.23	1.33	9.46	Part Lyβ at $z_{ab} = 2.4580$?
3557.77.....	3556.04–3559.82	0.63	5.57	
3562.52.....	3565.11–3563.59	0.36	3.84	
3566.16.....	3563.59–3567.38	0.86	9.19	
3568.67.....	3567.38–3569.65	0.48	5.08	
3571.56.....	3569.65–3573.43	1.67	15.68	Lyα at $z_{ab} = 1.93794$?
3576.59.....	3573.43–3578.53	0.42	3.90	
3586.13.....	3583.50–3589.19	0.81	5.09	
3591.30.....	3589.19–3594.60	0.56	3.51	
3596.47.....	3594.60–3597.63	1.30	13.33	
3599.95.....	3598.38–3601.41	0.99	9.87	
3604.41.....	3601.41–3606.70	2.35	19.79	
3609.90.....	3608.97–3611.24	0.58	7.62	
3624.03.....	3622.58–3624.71	0.51	3.67	
3627.71.....	3624.71–3629.61	2.25	16.24	Lyα at $z_{ab} = 1.98412$, part Lyβ at $z_{ab} = 2.5365$?
3630.57.....	3629.61–3631.65	1.13	8.20	Lyα at $z_{ab} = 1.98498$, Lyβ at $z_{ab} = 2.53963$
3634.92.....	3632.95–3636.70	0.73	6.34	Lyβ at $z_{ab} = 2.54377$?
3640.07.....	3636.70–3644.51	1.39	12.03	Lyβ at $z_{ab} = 2.54879$?, part Fe III λ1122 at $z_{ab} = 2.24275$
3642.82.....	3636.95–3644.51	1.06	9.17	Lyβ at $z_{ab} = 2.55147$
3657.13.....	3655.10–3658.95	1.33	13.38	
3659.54.....	3658.95–3661.15	0.44	4.37	Lyβ at $z_{ab} = 2.56777$
3667.22.....	3664.93–3667.90	0.90	9.66	Lyβ at $z_{ab} = 2.57526$
3669.52.....	3667.90–3671.73	0.83	8.86	
3680.35.....	3678.54–3681.68	0.73	7.25	Part C II λ1036 at $z_{ab} = 2.5513$
3683.74.....	3681.68–3686.10	1.12	11.64	
3692.59.....	3690.64–3695.17	1.17	15.46	
3698.41.....	3695.17–3701.22	2.45	30.43	Lyα at $z_{ab} = 2.04228$
3705.54.....	3707.80–3713.30	0.53	6.58	
3715.67.....	3714.08–3717.10	0.71	12.02	
3721.37.....	3717.86–3724.66	3.18	49.91	Lyα at $z_{ab} = 2.06117$?
3732.70.....	3730.71–3734.77	2.04	24.42	Si III λ1206 at $z_{ab} = 2.09383$
3735.62.....	3734.77–3737.52	0.84	10.09	
3740.60.....	3737.10–3741.30	0.35	4.18	
3744.54.....	3742.06–3747.35	0.84	10.56	
3762.09.....	3756.42–3767.01	10.56	91.42	Lyα at $z_{ab} = 2.09466$
3774.66.....	3773.06–3776.55	1.33	14.29	
3778.14.....	3776.55–3779.86	1.10	11.86	
3786.19.....	3782.89–3788.94	2.78	35.78	
3794.23.....	3792.90–3796.70	0.35	3.79	
3807.42.....	3706.10–3810.00	0.47	5.10	
3815.20.....	3811.62–3819.18	4.48	55.77	
3837.41.....	3834.31–3840.36	2.80	40.10	
3857.10.....	3854.72–3860.02	1.36	21.47	Part Si II λ1190 at $z_{ab} = 2.24013$
3870.54.....	3867.58–3873.63	2.44	39.45	
3880.52.....	3878.92–3881.74	0.54	8.15	
3882.88.....	3881.74–3884.21	0.50	7.70	
3893.54.....	3891.02–3895.56	0.94	14.13	
3898.94.....	3896.31–3901.61	2.00	29.20	Part Si II λ1260 at $z_{ab} = 2.0934$
3907.74.....	3905.39–3909.92	2.29	34.30	
3911.24.....	3909.92–3912.19	0.54	9.66	Si III λ1206 at $z_{ab} = 2.24181$
3913.94.....	3912.19–3914.81	0.67	8.15	
3916.87.....	3914.81–3919.00	1.59	19.24	
3924.59.....	3922.78–3926.43	0.75	12.77	
3926.96.....	3926.43–3927.36	0.21	3.64	
3932.29.....	3930.34–3934.88	1.39	20.73	

TABLE 3—*Continued*

λ_{vac} (mean)	λ Range	W_{obs}	S/N	Comments
3940.01.....	3934.88–3944.71	5.98	69.50	Lyα at $z_{ab} = 2.24102$
3947.28.....	3946.22–3948.49	0.55	5.61	
3954.12.....	3949.49–3956.05	0.27	3.61	
3960.19.....	3957.65–3962.80	0.37	5.29	
3966.93.....	3964.37–3968.65	1.08	15.09	
3969.47.....	3968.65–3971.17	0.52	7.22	
3975.53.....	3974.50–3977.00	0.33	4.08	
3981.61.....	3977.00–3982.52	0.53	6.52	
3984.41.....	3982.52–3984.41	0.36	4.45	Part Fe III λ1122 at $z_{ab} = 2.5497$
3987.69.....	3984.41–3990.08	1.16	14.39	
3994.11.....	3991.59–3996.88	0.63	9.52	
4002.23.....	4000.66–4003.69	0.34	6.56	
4013.45.....	4012.01–4015.03	0.20	3.77	Fe III λ1122 at $z_{ab} = 2.57537$, N V λ1238 at $z_{ab} = 2.23973$
4016.52.....	4015.03–4018.06	0.23	4.39	N V λ1238 at $z_{ab} = 2.24221$
4024.74.....	4023.35–4026.37	0.30	5.72	
4028.88.....	4027.13–4030.49	0.58	8.08	Part N V λ1242 at $z_{ab} = 2.2418$
4032.12.....	4030.49–4033.18	0.63	8.91	
4038.49.....	4036.20–4040.74	2.23	39.73	
4042.83.....	4040.74–4044.94	1.35	17.78	
4046.16.....	4044.94–4048.30	0.78	10.30	
4053.59.....	4050.57–4057.20	2.22	28.12	
4058.30.....	4057.20–4060.40	0.70	8.82	
4067.55.....	4064.94–4069.48	0.24	3.91	
4075.51.....	4074.01–4076.61	0.56	8.61	
4078.38.....	4076.61–4080.06	0.90	13.87	
4084.51.....	4082.33–4088.38	0.64	12.31	Si II λ1260 at $z_{ab} = 2.24059$
4091.04.....	4088.38–4093.67	1.42	22.47	Lyα at $z_{ab} = 2.36526$?, part Fe III λ1144 at $z_{ab} = 2.5754$?
4096.59.....	4093.67–4098.97	0.39	6.04	
4100.93.....	4098.97–4102.38	0.90	13.09	
4103.98.....	4102.38–4105.77	1.00	14.48	
4112.58.....	4111.07–4114.09	0.50	9.98	
4116.14.....	4114.09–4117.87	0.30	4.32	
4119.67.....	4117.87–4120.90	0.35	6.67	
4129.03.....	4126.94–4131.48	1.50	25.91	C II λ1334 at $z_{ab} = 2.09399$
4137.98.....	4136.02–4139.14	1.16	15.32	Part C I λ1277 at $z_{ab} = 2.23977$
4140.03.....	4139.14–4143.58	0.89	11.77	C I λ1277 at $z_{ab} = 2.24137$
4150.27.....	4148.12–4151.90	1.13	15.38	
4154.04.....	4151.90–4156.44	1.48	20.12	
4162.04.....	4159.46–4164.15	2.17	26.12	
4166.56.....	4164.15–4170.05	1.83	22.05	Lyα at $z_{ab} = 2.42738$?
4175.04.....	4173.07–4176.85	0.97	16.41	
4178.61.....	4176.85–4179.88	0.78	14.11	
4183.60.....	4181.39–4185.93	1.74	9.56	Lyα at $z_{ab} = 2.44139$?
4192.34.....	4190.46–4195.00	0.42	7.03	
4201.01.....	4198.02–4202.35	2.39	38.43	Lyα at $z_{ab} = 2.45572$?
4203.80.....	4202.35–4206.34	2.59	41.75	Lyα at $z_{ab} = 2.45801$?
4209.14.....	4207.85–4210.88	0.27	5.58	
4223.29.....	4221.47–4225.10	0.47	7.06	
4227.09.....	4225.10–4229.03	0.52	7.78	Part Si II λ1190 at $z_{ab} = 2.55094$, Si II λ1304 at $z_{ab} = 2.24071$
4243.75.....	4242.10–4245.30	0.34	5.09	
4250.10.....	4248.69–4252.28	1.06	13.94	
4253.23.....	4252.28–4254.15	0.48	6.38	
4256.17.....	4254.15–4257.76	1.07	14.09	
4262.15.....	4260.79–4263.81	0.88	19.16	
4266.85.....	4265.32–4269.10	0.95	18.83	
4273.85.....	4272.89–4275.15	0.73	18.15	
4279.32.....	4277.42–4281.96	1.30	18.13	
4284.34.....	4281.96–4287.25	1.32	18.40	Part Si III λ1206 at $z_{ab} = 2.55105$
4290.60.....	4288.05–4291.25	0.25	3.55	
4299.20.....	4297.08–4300.66	2.10	29.36	Lyα at $z_{ab} = 2.53649$?
4302.76.....	4300.66–4305.95	3.02	42.19	Lyα at $z_{ab} = 2.53941$
4307.68.....	4305.95–4309.94	1.64	22.93	Lyα at $z_{ab} = 2.54346$?
4313.56.....	4310.69–4315.08	2.46	41.27	Lyα at $z_{ab} = 2.54830$?, part Si III λ1206 at $z_{ab} = 2.5753$ Si IV λ1393 at $z_{ab} = 2.09492$
4316.91.....	4315.08–4319.77	2.96	49.62	Lyα at $z_{ab} = 2.55105$
4323.45.....	4320.60–4323.32	0.22	3.62	C II λ1334 at $z_{ab} = 2.23967$
4326.46.....	4323.32–4329.60	0.53	8.86	C II λ1334 at $z_{ab} = 2.24193$
4332.03.....	4329.60–4334.53	1.90	31.82	Lyα at $z_{ab} = 2.56694$
4335.54.....	4334.53–4337.16	0.77	12.94	
4340.19.....	4338.67–4342.45	1.40	34.14	Si IV λ1402 at $z_{ab} = 2.09401$
4345.51.....	4343.21–4348.53	1.61	33.71	Lyα at $z_{ab} = 2.57458$
4349.27.....	4348.53–4350.01	0.52	8.66	
4356.58.....	4354.55–4358.79	0.88	14.65	
4359.60.....	4358.79–4361.36	0.32	5.33	
4362.96.....	4361.36–4364.39	0.46	9.00	

TABLE 3—*Continued*

λ_{vac} (mean)	λ Range	W_{obs}	S/N	Comments
4365.09.....	4364.39–4365.50	0.23	4.40	
4369.82.....	4365.50–4373.46	2.47	60.17	Lyα at $z_{ab} = 2.59458$[a]
4376.87.....	4374.30–4378.85	0.09	3.50	
4379.78.....	4378.75–4381.02	0.21	8.10	
4385.64.....	4383.29–4387.82	0.64	19.59	
4475.62.....	4473.27–4477.81	0.32	6.05	Si II λ1260 at $z_{ab} = 2.55089$
4515.75.....	4513.35–4517.74	0.99	11.54	Si IV λ1393 at $z_{ab} = 2.23999$
4518.70.....	4517.74–4520.64	0.48	5.62	Si IV λ1393 at $z_{ab} = 2.24211$
4544.50.....	4541.50–4545.89	0.36	5.03	Si IV λ1402 at $z_{ab} = 2.23966$
4547.72.....	4545.89–4549.80	0.47	6.61	C IV λ1548 at $z_{ab} = 1.93742$?, Si IV λ1402 at $z_{ab} = 2.2196$
4559.46.....	4557.60–4560.80	0.35	4.93	
4622.26.....	4620.70–4623.60	0.62	5.87	C IV λ1548 at $z_{ab} = 1.98557$
4630.08.....	4628.67–4631.57	0.48	4.59	C IV λ1550 at $z_{ab} = 1.98566$, Si II λ1304 at $z_{ab} = 2.5496$
4710.35.....	4709.07–4711.25	0.35	4.18	C IV λ1548 at $z_{ab} = 2.04246$
4718.36.....	4716.80–4720.10	0.37	5.27	C IV λ1550 at $z_{ab} = 2.04258$
4739.29.....	4736.60–4741.67	0.72	5.88	C IV λ1548 at $z_{ab} = 2.06116$?, part C II λ1334 at $z_{ab} = 2.5513$
4789.77.....	4786.11–4791.82	1.89	9.81	C IV λ1548 at $z_{ab} = 2.09376$
4792.93.....	4791.82–4794.34	1.03	5.33	C IV λ1548 at $z_{ab} = 2.09580$
4797.06.....	4794.34–4800.23	1.85	9.57	C IV λ1550 at $z_{ab} = 2.09333$
4801.37.....	4800.23–4803.97	0.66	3.53	C IV λ1550 at $z_{ab} = 2.09611$
4949.39.....	4947.39–4951.01	0.40	4.17	Si IV λ1393 at $z_{ab} = 2.55112$, part Si II λ1526 at $z_{ab} = 2.2419$
4981.25.....	4979.98–4982.88	0.38	4.38	Si IV λ1393 at $z_{ab} = 2.57398$, Si IV λ1402 at $z_{ab} = 2.55101$
5014.99.....	5012.58–5016.22	1.62	9.93	C IV λ1548 at $z_{ab} = 2.23923$
5018.86.....	5016.22–5022.15	3.48	21.37	C IV λ1548 at $z_{ab} = 2.24173$
5023.38.....	5022.15–5024.69	1.29	7.94	C IV λ1550 at $z_{ab} = 2.23927$
5027.21.....	5024.69–5030.69	2.49	15.24	C IV λ1550 at $z_{ab} = 2.24174$
5168.70.....	5166.87–5171.22	0.58	5.47	Al II λ1670 at $z_{ab} = 2.09357$
5497.83.....	5495.73–5500.07	0.56	5.14	C IV λ1548 at $z_{ab} = 2.55111$

[a] If this line at 4369.82 Å is Lyα, one should expect to see Lyβ at 3687.04 Å. There is a marginally detected line there, with $W_{obs} \approx 0.3$ Å, so 4369.82 Å is plausibly consistent with being Lyα.

explicitly stated otherwise. While their spectra below Lyβ emission are not so obviously contaminated by non-Lyα lines, this might be caused by our ignorance of further metal-line systems because of the smaller wavelength coverage in these spectra compared to the LB pair. The Lyβ to α emission line range from above constrains these samples such that all three overlap for redshifts 2.02–2.48.

For lines at redshifts lower than $z = 2.02$, the sensitivity of our data is also declining, but for some purposes, sensitivity cutoffs as large as $W_0 = 0.4$ Å are useful. Also, for some purposes, we might be less worried about metal-line contamination, especially since we show that the metal-line system redshifts are weakly correlated between sight lines. In a limited number of specified cases, we impose a cutoff at $\lambda = 3350$ Å (or $z = 1.756$), below which the sensitivity in KP 78 drops below $W_0 = 0.4$ Å. Given a line-of-sight number density evolution $N(z) \propto (1 + z)^{\gamma}$, with an assumed $\gamma = 2.1$ (see § 4.3), we study an average $\langle z \rangle = 2.25$ for the generally used restrictive sample, and $\langle z \rangle = 2.14$ for the less used, larger redshift range.

We take as Lyα lines all those between the wavelengths listed above and not otherwise identified as a metal line (although they can be the Lyα component of a metal-line redshift system). This is the "pure" Lyα sample. The "contaminated" sample is one in which a detectable contribution is suspected from a metal line from another redshift system, but the presence of a Lyα line is inferred from the strength of the actual line above that of the inferred metal line.

For unresolved Lyα lines in the KP triplet sample, then, the completeness cutoff (the 3.5 σ threshold plus another 2 σ to assure completeness) in each 1020–1220 Å region is about $W_0 = 0.19$, 0.09, and 0.15 Å, respectively. For LB 9605 and 9612, the sample reaches $W_0 \approx 0.12$ and 0.13 Å, respectively (except for a small interval $1.691 < z < 1.768$ for LB 9605, where the threshold is as high as 0.4 Å), with the same caveats regarding uncrowded and unresolved lines. In some of our treatment below, we will discuss thresholds as low as $W_0 = 0.1$ Å, knowing that this falls slightly short of our completeness condition, but most interesting results apply to cutoffs of $W_0 = 0.2$ Å, 0.4 Å, or higher. The sensitivity of the spectra and our various Lyα samples are further described in Table 6.

4. RESULTS

These higher quality data allow us to improve several unique measurements made in Crotts (1989) using the KP triplet, plus several new tests that we apply for the first time. Sections 4.1, 4.2, and 4.3 deal with tests originally developed for the triplet in Crotts (1989), and § 4.4 applies cloud size techniques developed in Papers II and III to the LB pair for the first time, as well as the improved triplet data set. For this reason we reserve detailed discussion of techniques for § 4.5 and later and refer the reader to these previous papers for earlier developments.

4.1. *Lyα Velocity Cross Correlation*

Following Crotts (1989), we can compute the spatial two-point function of Lyα absorbers by cross-correlating in velocity the distribution of Lyα lines ("pure" and "contaminated"). The resulting pairs are binned at 50 km s^{-1} intervals with cutoffs of, alternately, $W_0 > 0.1$, 0.2, 0.4, and 0.8 Å. For the triplet (all three sight-line pairs summed together) and the pair, the resulting cross-correlation pair count as a function of velocity difference Δv is shown in Figures 6*a* and 6*b*, respectively. For the triplet, the $\langle z \rangle = 2.25$ sample is shown.

In Figure 6*a* for the triplet, there is no apparent structure

TABLE 4

ABSORPTION LINES IN LB 9605

λ_{vac} (mean)	λ Range	W_{obs}	S/N	Comments
1669.79.....	1668.39–1670.90	0.81	3.79	Al II λ1670 at $z_{ab} = -0.00060$
1691.70.....	1690.62–1692.77	0.93	4.92	Part Lyγ at $z_{ab} = 0.738$
1697.99.....	1696.72–1699.23	0.97	5.15	
1714.77.....	1713.21–1716.44	1.21	6.17	Lyα at $z_{ab} = 0.41056$?
1724.98.....	1723.97–1725.77	0.65	3.85	
1731.96.....	1731.14–1732.58	0.46	3.54	
1743.65.....	1741.90–1745.13	0.65	3.63	Lyβ at $z_{ab} = 0.69992$?
1780.02.....	1779.20–1780.63	0.42	3.72	
1782.94.....	1780.99–1784.93	1.57	9.39	Lyβ at $z_{ab} = 0.73823$
1793.71.....	1792.11–1794.97	0.96	6.41	
1803.33.....	1801.79–1805.02	1.10	6.97	
1838.92.....	1837.29–1840.52	0.64	3.77	
1843.96.....	1842.67–1845.18	0.72	5.18	
1856.93.....	1855.58–1858.45	0.82	5.52	
1885.09.....	1883.19–1886.78	0.85	5.44	
1894.79.....	1893.95–1895.74	0.58	4.97	
1926.51.....	1924.79–1928.37	0.98	7.14	Part Lyδ at $z_{ab} = 1.028$
1950.10.....	1948.81–1951.68	0.80	5.72	Lyϵ at $z_{ab} = 1.07943$
1960.38.....	1959.57–1961.01	0.40	3.93	Lyγ at $z_{ab} = 1.01574$
1974.04.....	1970.69–1977.14	1.99	10.31	Part Lyδ at $z_{ab} = 1.080$, part Lyγ at $z_{ab} = 1.028$
1980.19.....	1978.58–1981.81	0.79	5.40	Part C III λ977 at $z_{ab} = 1.028$?
1986.06.....	1985.39–1987.19	0.97	8.64	
2017.73.....	2016.23–2018.74	0.68	5.80	Lyβ at $z_{ab} = 0.96713$?
2022.45.....	2020.18–2024.12	1.47	10.05	Lyγ at $z_{ab} = 1.07956$
2030.74.....	2030.22–2031.29	0.51	6.05	
2044.21.....	2043.48–2044.92	0.66	7.69	
2065.47.....	2064.64–2066.53	0.93	7.26	
2067.77.....	2066.53–2069.30	1.10	8.57	Part Lyβ at $z_{ab} = 1.01592$, Lyα at $z_{ab} = 0.70020$?
2079.90.....	2077.91–2081.86	1.37	12.44	Lyβ at $z_{ab} = 1.02774$
2091.59.....	2090.46–2092.97	0.60	6.47	O VI λ1031 at $z_{ab} = 1.02689$
2103.69.....	2102.66–2104.81	0.36	4.24	O VI λ1037 at $z_{ab} = 1.02743$
2106.07.....	2104.81–2107.32	0.53	5.69	
2113.37.....	2110.90–2116.28	2.69	25.69	Lyα at $z_{ab} = 0.73844$
2122.67.....	2121.66–2123.81	0.32	3.87	
2133.16.....	2130.27–2135.29	1.69	15.81	Lyβ at $z_{ab} = 1.07967$
2145.41.....	2144.25–2146.76	0.30	3.61	
2157.78.....	2156.09–2159.31	0.62	7.01	
2161.75.....	2161.11–2162.54	0.24	3.93	
2184.19.....	2182.98–2185.85	0.66	8.61	Part Lyδ at $z_{ab} = 1.301$, C IV λ1548 at $z_{ab} = 0.41079$?
2187.63.....	2186.57–2188.72	0.29	4.02	C IV λ1550 at $z_{ab} = 0.41067$?
2219.94.....	2218.12–2222.07	1.36	17.02	Lyβ at $z_{ab} = 1.16427$?
2222.95.....	2222.07–2223.86	0.38	6.49	
2231.24.....	2229.60–2233.46	0.63	7.43	
2238.26.....	2235.51–2240.62	0.64	6.91	Lyγ at $z_{ab} = 1.30147$
2249.23.....	2247.78–2250.34	0.26	3.60	Lyβ at $z_{ab} = 1.19283$
2254.53.....	2253.41–2255.96	0.32	4.47	
2273.37.....	2271.30–2275.91	0.75	7.91	
2278.59.....	2276.42–2280.51	1.03	11.39	
2284.17.....	2282.55–2285.62	0.37	4.62	
2306.76.....	2305.05–2308.12	0.41	4.36	
2342.94.....	2341.36–2344.43	0.39	4.29	Fe II λ2344 at $z_{ab} = -0.00054$
2354.42.....	2353.12–2355.68	0.65	6.03	
2360.87.....	2359.26–2362.32	0.98	9.30	Lyβ at $z_{ab} = 1.30167$
2367.....				No Ly limit ($\tau < 0.1$)
2373.83.....	2371.53–2376.64	0.88	6.29	Si III λ1206 at $z_{ab} = 0.96753$?
2381.62.....	2379.71–2384.31	0.71	5.43	Fe II λ2382 at $z_{ab} = -0.00048$
2386.86.....	2385.80–2389.40	0.71	5.60	Part Ly10 at $z_{ab} = 1.596$
2391.51.....	2389.43–2393.52	1.10	9.53	Part Ly9 at $z_{ab} = 1.596$, Lyα at $z_{ab} = 0.96724$?
2396.27.....	2394.69–2395.90	0.57	4.96	Ly8 at $z_{ab} = 1.59575$
2403.82.....	2402.21–2405.79	0.62	5.68	Ly7 at $z_{ab} = 1.59529$
2415.72.....	2414.49–2417.55	0.54	5.33	Ly6 at $z_{ab} = 1.59546$
2422.54.....	2421.64–2423.69	0.42	4.94	Si IV λ1393 at $z_{ab} = 0.73814$
2434.15.....	2432.89–2435.96	0.70	5.82	Lyϵ at $z_{ab} = 1.59559$
2445.28.....	2443.63–2447.21	1.23	11.65	Part Si II λ1206 at $z_{ab} = 1.028$
2448.77.....	2447.72–2449.26	0.64	7.72	
2451.14.....	2449.26–2452.84	1.29	13.14	Lyα at $z_{ab} = 1.01629$
2455.94.....	2455.39–2456.42	0.40	6.30	
2463.15.....	2462.04–2463.46	0.40	3.54	
2465.33.....	2463.46–2468.18	2.39	21.31	Lyα at $z_{ab} = 1.02796$, part Lyδ at $z_{ab} = 1.596$
2471.89.....	2471.25–2472.78	0.36	5.05	Lyδ at $z_{ab} = 1.60269$
2479.80.....	2478.41–2481.47	0.61	6.89	
2483.36.....	2482.50–2484.03	0.35	4.95	Fe I λ2484 at $z_{ab} = -0.00027$
2490.79.....	2489.40–2492.90	0.48	6.84	Lyβ at $z_{ab} = 1.42833$?

TABLE 4—*Continued*

λ_{vac} (mean)	λ Range	W_{obs}	S/N	Comments
2524.37.....	2522.38–2526.43	1.52	12.03	Part Fe I λ2523 at $z_{ab} = 0.000$, Lyγ at $z_{ab} = 1.59565$
2528.85.....	2526.43–2532.61	2.41	19.05	Lyα at $z_{ab} = 1.08021$, part Lyγ at $z_{ab} = 1.603$
2539.93.....	2537.94–2541.30	0.36	4.54	
2558.29.....	2556.64–2559.71	0.64	8.05	
2577.64.....	2574.54–2580.17	1.13	11.21	Part Mn II λ2576 at $z_{ab} = 0.000$, part Lyβ at $z_{ab} = 1.513$
2584.38.....	2582.21–2586.30	0.78	8.65	Part Fe II λ2586 at $z_{ab} = 0.000$
2592.94.....	2590.39–2595.00	0.58	6.35	Mn II λ2594 at $z_{ab} = -0.00061$, O VI λ1031 at $z_{ab} = 1.51272$
2598.41.....	2595.51–2600.62	1.11	12.14	Part Ly7 at $z_{ab} = 1.805$, part Fe II λ2600 at $z_{ab} = 0.000$
2607.95.....	2606.25–2609.14	0.92	6.63	Mn II λ2606 at $z_{ab} = 0.00057$, part O VI λ1037 at $z_{ab} = 1.51341$
2610.42.....	2609.14–2612.90	0.64	4.56	Ly6 at $z_{ab} = 1.80465$
2612.98.....	2612.90–2614.41	0.64	4.61	Lyγ at $z_{ab} = 1.68676$
2617.23.....	2614.41–2620.05	1.27	9.11	Lyϵ at $z_{ab} = 1.80480$, part Lyβ at $z_{ab} = 1.551$?
2625.59.....	2622.10–2628.24	0.94	9.38	
2630.35.....	2628.24–2632.96	1.27	10.35	Lyα at $z_{ab} = 1.16370$?
2634.20.....	2632.96–2635.38	0.60	4.90	
2636.81.....	2635.38–2638.46	0.73	5.92	
2646.67.....	2645.11–2647.68	0.48	4.63	
2648.68.....	2647.68–2651.25	0.47	4.58	Lyβ at $z_{ab} = 1.58226$?, part Lyγ at $z_{ab} = 1.725$?
2662.63.....	2659.43–2664.36	2.31	23.15	Lyβ at $z_{ab} = 1.59586$, part Lyδ at $z_{ab} = 1.804$
2665.62.....	2664.36–2668.63	1.67	16.80	Lyα at $z_{ab} = 1.19272$
2670.99.....	2670.17–2672.72	0.76	11.20	Lyβ at $z_{ab} = 1.60401$
2679.32.....	2676.81–2682.44	1.62	17.33	
2685.40.....	2684.49–2687.55	0.99	12.81	
2690.98.....	2689.09–2691.86	0.80	7.02	C IV λ1548 at $z_{ab} = 0.73813$
2692.68.....	2691.86–2693.76	0.75	6.59	Lyβ at $z_{ab} = 1.62515$?
2696.06.....	2693.76–2698.29	1.59	13.98	Part C IV λ1550 at $z_{ab} = 0.738$
2699.88.....	2698.80–2700.81	0.31	4.33	
2701.95.....	2700.81–2702.38	0.38	5.27	Lyδ at $z_{ab} = 1.84493$
2712.95.....	2711.59–2714.15	0.40	4.58	
2719.32.....	2717.73–2720.79	0.27	3.87	
2727.88.....	2725.91–2730.00	1.21	17.18	Lyγ at $z_{ab} = 1.80491$
2734.80.....	2733.20–2736.40	0.22	4.15	
2737.81.....	2736.40–2739.71	0.22	4.22	
2740.62.....	2739.71–2741.25	0.28	5.41	
2750.55.....	2747.38–2753.08	1.68	16.99	Lyβ at $z_{ab} = 1.68157$?
2754.56.....	2753.08–2756.08	0.72	7.31	Lyβ at $z_{ab} = 1.68548$
2765.67.....	2763.24–2768.35	0.86	10.87	Lyγ at $z_{ab} = 1.84377$
2770.97.....	2769.37–2772.44	0.59	9.66	Lyβ at $z_{ab} = 1.70148$?
2781.60.....	2780.11–2783.18	0.32	4.91	
2787.30.....	2785.74–2788.80	0.33	5.05	
2794.73.....	2792.90–2795.65	1.11	10.99	Mg II λ2796 at $z_{ab} = -0.00058$, Lyβ at $z_{ab} = 1.72465$?
2797.78.....	2795.65–2800.04	1.75	17.31	Lyα at $z_{ab} = 1.30143$
2801.97.....	2800.04–2804.15	1.50	14.81	Part Mg II λ2803 at $z_{ab} = -0.00056$
2805.81.....	2805.17–2807.21	0.37	6.63	
2809.95.....	2808.75–2811.30	0.33	5.56	Lyβ at $z_{ab} = 1.73948$?
2817.59.....	2815.91–2819.49	0.39	5.49	Lyβ at $z_{ab} = 1.74693$?
2821.96.....	2820.51–2823.58	0.27	4.05	Fe III λ1122 at $z_{ab} = 1.51393$, Lyβ at $z_{ab} = 1.75116$?
2827.21.....	2826.13–2828.18	0.28	4.86	Part Si IV λ1393 at $z_{ab} = 1.028$?
2843.59.....	2841.99–2845.57	0.29	3.76	Lyβ at $z_{ab} = 1.77228$?
2851.00.....	2849.66–2852.21	0.25	4.05	Mg I 2852 at $z_{ab} = -0.00069$
2860.76.....	2858.86–2862.44	0.49	6.99	Lyβ at $z_{ab} = 1.78902$?
2869.61.....	2868.00–2871.32	0.33	4.53	
2876.94.....	2874.20–2879.83	1.76	22.90	Lyβ at $z_{ab} = 1.80479$, part Fe II λ1144 at $z_{ab} = 1.514$
2894.06.....	2891.59–2896.19	0.59	8.15	Lyβ at $z_{ab} = 1.82195$
2916.24.....	2914.60–2918.18	0.68	11.26	Lyβ at $z_{ab} = 1.84311$
2923.25.....	2921.76–2924.21	0.62	9.88	
2924.71.....	2924.21–2925.74	0.33	5.19	
2926.44.....	2925.74–2927.85	0.22	3.51	
2930.97.....	2929.94–2931.99	0.19	3.84	
2935.48.....	2934.54–2936.59	0.37	7.42	
2944.10.....	2943.24–2944.77	0.22	4.87	
2952.50.....	2950.40–2954.49	1.07	16.80	Lyα at $z_{ab} = 1.42870$?
2963.21.....	2959.09–2966.25	1.00	10.64	
2977.97.....	2976.48–2979.03	0.33	5.13	
2988.55.....	2987.22–2989.77	0.30	4.57	
2999.63.....	2995.40–3002.56	0.92	9.34	
3003.71.....	3002.56–3005.62	0.26	3.71	
3051.53.....	3050.62–3052.67	0.23	3.67	
3055.27.....	3053.18–3057.27	1.26	18.05	Lyα at $z_{ab} = 1.51324$
3077.11.....	3075.17–3079.26	0.43	5.31	
3093.03.....	3091.53–3094.60	0.49	6.91	
3101.24.....	3098.69–3102.53	1.55	16.44	Lyα at $z_{ab} = 1.55105$?
3103.51.....	3102.53–3105.85	1.17	12.38	
3127.73.....	3125.79–3129.37	0.71	8.84	
3131.51.....	3129.37–3133.98	0.85	9.39	

TABLE 4—*Continued*

λ_{vac} (mean)	λ Range	W_{obs}	S/N	Comments
3139.51.....	3136.02–3143.41	2.84	23.37	C IV λ1548 at $z_{ab} = 1.02784$, Lyα at $z_{ab} = 1.583$
3145.19.....	3143.41–3146.76	1.29	10.63	C IV λ1550 at $z_{ab} = 1.02814$
3156.05.....	3153.41–3158.87	3.30	35.75	Lyα at $z_{ab} = 1.59614$
3159.63.....	3158.87–3161.08	0.86	9.34	
3163.73.....	3161.08–3165.98	1.43	13.54	Lyα at $z_{ab} = 1.60246$
3167.11.....	3165.98–3168.75	0.72	6.79	Si II λ1260 at $z_{ab} = 1.51274$
3191.61.....	3188.18–3195.85	1.55	15.44	Lyα at $z_{ab} = 1.62539$?
3203.26.....	3201.99–3204.54	0.49	7.33	
3210.14.....	3209.15–3211.66	0.29	3.86	C I λ1277 at $z_{ab} = 1.51333$?
3215.93.....	3214.69–3217.72	0.46	5.81	
3241.63.....	3240.42–3242.44	0.34	5.42	
3249.00.....	3248.49–3249.50	0.24	4.93	
3259.47.....	3257.07–3262.61	2.00	23.05	Lyα at $z_{ab} = 1.68121$?
3264.57.....	3262.61–3266.64	1.53	16.16	Lyα at $z_{ab} = 1.68541$
3283.39.....	3282.25–3284.85	2.28	6.64	Lyα at $z_{ab} = 1.70089$?
3285.62.....	3284.85–3286.61	1.20	3.55	
3310.86.....	3309.40–3312.80	1.12	4.58	Lyα at $z_{ab} = 1.72349$?
3318.61.....	3317.65–3319.59	0.86	4.77	
3330.30.....	3328.80–3331.22	1.05	5.82	Lyα at $z_{ab} = 1.73948$?
3339.33.....	3337.53–3341.89	1.97	9.65	Lyα at $z_{ab} = 1.74690$?
3345.10.....	3343.83–3346.26	0.98	6.45	Lyα at $z_{ab} = 1.75165$?
3365.96.....	3365.17–3367.11	0.61	5.21	
3370.41.....	3369.05–3371.96	1.15	8.48	Lyα at $z_{ab} = 1.77247$?
3391.24.....	3389.41–3393.85	1.68	11.46	Lyα at $z_{ab} = 1.78961$?
3394.46.....	3393.85–3396.69	0.87	5.93	C IV λ1548 at $z_{ab} = 1.19257$
3404.54.....	3403.18–3405.87	0.47	3.70	Si III λ1206 at $z_{ab} = 1.82183$?
3407.19.....	3405.87–3407.74	0.71	5.60	
3409.70.....	3407.74–3413.17	2.57	20.12	Lyα at $z_{ab} = 1.80454$
3420.62.....	3419.48–3421.42	0.20	3.64	
3429.73.....	3427.72–3431.60	1.07	16.15	Lyα at $z_{ab} = 1.82127$
3434.43.....	3433.54–3435.48	0.21	4.38	
3440.20.....	3438.39–3442.27	0.61	10.87	
3449.11.....	3447.37–3450.77	0.21	3.80	
3456.64.....	3454.88–3458.76	1.53	31.53	Lyα at $z_{ab} = 1.84340$
3485.66.....	3483.97–3487.37	0.35	5.75	
3568.98.....	3567.38–3570.29	0.31	4.09	C IV λ1550 at $z_{ab} = 1.30142$?
3756.50.....	3749.18–3763.14	1.05	6.25	Continuum error?
3891.41.....	3889.75–3892.79	0.42	6.45	C IV λ1548 at $z_{ab} = 1.51350$
3897.89.....	3896.59–3898.87	0.27	4.59	C IV λ1550 at $z_{ab} = 1.51351$
3928.13.....	3926.98–3929.26	0.22	3.97	
3933.11.....	3931.54–3934.58	0.22	3.57	Ca II λ3934 at $z_{ab} = -0.00042$
4019.20.....	4017.39–4021.19	0.29	4.39	C IV λ1548 at $z_{ab} = 1.59604$

NOTE.—A line at 4404.56 Å is uncertain because of rapid change in continuum in the C IV emission line.

for weaker lines, e.g., samples with cutoffs at $W_0 = 0.1$ or 0.2 Å, but structure is apparent for lines with $W_0 > 0.4$ or 0.8 Å. For $W_0 > 0.4$ Å, there are an average of 2.97 pairs per 50 km s^{-1} bin in the first 3000 km s^{-1} of Δv (and 2.83 per bin over 3000 km s^{-1} $< \Delta v <$ 6000 km s^{-1}), so that the appearance of eight pairs (or more) in the first 50 km s^{-1} bin as a random fluctuation is ruled out at the 99.0% level. (This is the Poisson confidence level for excluding the hypothesis that there is no intrinsic excess in the first bin, as might be substantiated by larger samples.) There are also 20 pairs in the first 200 km s^{-1}, which is ruled out as a random fluctuation at the 98.4% level. Thus there is evidence for a cross-correlation signal in the smallest velocity bins for pairs of $W_0 > 0.4$ Å lines, at about the 2.5 σ level. This can be described by a two-point correlation function, averaged over proper separations of 496–720 h^{-1} kpc and with $\langle z \rangle = 2.25$ of $\xi = 0.72^{+0.48}_{-0.38}$ (68% confidence limits—*not* directly translatable into Gaussian standard deviations for such a small sample). For the extended $\langle z \rangle = 2.14$ sample, the clustering signal is stronger, both in magnitude and statistical significance: 29 pairs in the first 200 km s^{-1} bin versus 15.6 expected, implying $\xi = 0.86^{+0.41}_{-0.28}$, inconsistent with $\xi = 0$ at the 99.92% level. When only "pure" Lyα lines are considered, there are 26 in the first bin with 11.7 expected, implying $\xi = 1.23^{+0.53}_{-0.36}$, inconsistent with zero at the 99.991% level.

How important is the elimination of all Lyα lines with associated metal lines at the same z? We did this for the extended, $\langle z \rangle = 2.14$ sample and found 21 pairs in the first 200 km s^{-1} bin versus 7.3 expected, giving $\xi = 1.88^{+0.78}_{-0.50}$, which is inconsistent with the no-clustering hypothesis at the 99.999% level. Hence, the exclusion of the metal-containing systems makes the signal marginally stronger.

There is a weak signal for larger Δv and stronger lines. Nine $W_0 > 0.8$ Å pairs land within $\Delta v <$ 600 km s^{-1}, versus the mean expectation of only 3.6, a result expected in only 1.2% of random cases. Both of these results, for $W_0 > 0.8$ and 0.4 Å lines, are very similar to results found by Crotts (1989) for a significantly smaller sample.

For the LB pair, the results are less impressive. For $W_0 >$ 0.4 Å, there are no pairs in the first 50 km s^{-1} bin and only three pairs in the first 200 km s^{-1} bin, versus a mean expectation of 1.9. In the first 300 km s^{-1}, there are six pairs versus 2.8 expected, which is ruled out as being random at only the 93.5% level. There is a larger excess in the $W_0 > 0.2$ Å sample, nine pairs versus 6.0 mean expectation in the first 200 km s^{-1}, but it is even less statistically significant.

We conclude that the $\Delta v <$ 150–200 km s^{-1} cross-

TABLE 5

ABSORPTION LINES IN LB 9612

λ_{vac} (mean)	λ Range	W_{obs}	S/N	Comments
1687.67.....	1686.32–1688.83	1.47	4.05	Part Lyγ at $z_{ab} = 0.737$
1781.15.....	1779.91–1782.42	1.16	4.28	Lyβ at $z_{ab} = 0.73648$
1807.35.....	1806.81–1807.89	0.62	3.73	
1884.37.....	1883.55–1885.34	1.54	6.36	
1901.40.....	1900.76–1902.56	0.99	4.05	
2111.21.....	2109.47–2112.70	1.68	5.86	Lyα at $z_{ab} = 0.73666$, part Lyβ at $z_{ab} = 1.060$
2212.....				No Ly break ($\tau < 0.1$)
2240.36.....	2238.57–2242.15	1.12	4.65	Ly8 at $z_{ab} = 1.42687$[a]
2247.65.....	2246.25–2249.31	1.02	4.94	Ly7 at $z_{ab} = 1.42668$,[a] C III λ977 at $z_{ab} = 1.30050$
2275.30.....	2273.86–2276.93	1.09	5.01	Lyϵ at $z_{ab} = 1.42620$[a]
2304.33.....	2303.01–2305.56	1.02	4.95	Lyδ at $z_{ab} = 1.42627$[a]
2360.20.....	2358.23–2361.81	1.99	5.65	Part Lyγ at $z_{ab} = 1.426$,[a] part Lyβ at $z_{ab} = 1.300$?
2381.71.....	2380.22–2382.78	1.07	3.51	Fe II λ2382 at $z_{ab} = -0.00044$
2484.....				Ly break ($\tau \approx 2.1$)
2496.44.....	2495.00–2498.20	0.83	6.90	Lyβ at $z_{ab} = 1.435$?, Ly blend at $z_{ab} = 1.724$
2501.54.....	2500.39–2502.44	0.48	4.02	Part Lyβ at $z_{ab} = 1.439$?, Ly blend at $z_{ab} = 1.724$
2505.10.....	2503.46–2506.53	1.00	7.91	Part Ly10 at $z_{ab} = 1.72486$, Lyα at $z_{ab} = 1.060$
2508.90.....	2508.06–2509.60	0.67	6.50	Ly9 at $z_{ab} = 1.72421$
2515.14.....	2513.69–2516.25	0.53	4.70	Ly8 at $z_{ab} = 1.72452$, part Fe I λ2523 at $z_{ab} = 0.000$[b]
2523.64.....	2521.87–2525.45	0.79	6.18	Ly7 at $z_{ab} = 1.72465$
2536.15.....	2534.66–2538.24	0.90	7.54	Ly6 at $z_{ab} = 1.72485$
2555.07.....	2553.06–2557.16	1.04	8.42	Part Lyϵ at $z_{ab} = 1.724$, part Ly7 at $z_{ab} = 1.759$
2567.90.....	2566.36–2569.43	0.57	5.18	Ly6 at $z_{ab} = 1.75896$
2586.78.....	2583.75–2589.88	1.98	14.04	Part Lyδ at $z_{ab} = 1.724$, part Lyϵ at $z_{ab} = 1.759$, part Fe II λ2586 at $z_{ab} = 0.000$, Lyα at $z_{ab} = 1.127$
2599.39.....	2598.06–2601.13	0.70	6.56	Fe II λ2600 at $z_{ab} = 0.000$
2609.03.....	2608.29–2609.83	0.37	4.44	
2613.77.....	2612.38–2615.45	0.48	4.41	
2619.67.....	2617.50–2621.59	1.16	10.20	Part Lyδ at $z_{ab} = 1.759$, Lyβ at $z_{ab} = 1.55398$
2625.88.....	2624.15–2627.72	1.22	11.86	Part Lyϵ at $z_{ab} = 1.800$
2632.....				Ly break ($\tau \approx 0.6$)
2632.74.....	2630.79–2635.40	1.12	9.59	Part N V 1238 at $z_{ab} = 1.127$?
2649.61.....	2648.18–2651.76	0.97	9.76	Lyγ at $z_{ab} = 1.72443$
2655.15.....	2653.80–2657.38	0.54	5.53	Ly10 at $z_{ab} = 1.88807$, part Si III λ1206 at $z_{ab} = 1.127$?
2658.71.....	2657.38–2660.45	1.00	7.42	Ly9 at $z_{ab} = 1.88688$, part Lyδ at $z_{ab} = 1.800$
2661.77.....	2660.45–2663.10	0.75	5.59	C III λ977 at $z_{ab} = 1.72450$
2664.44.....	2663.10–2666.59	0.76	5.65	Ly8 at $z_{ab} = 1.88625$
2674.28.....	2671.70–2676.81	1.85	20.36	Part Ly7 at $z_{ab} = 1.886$
2683.94.....	2682.95–2684.86	0.64	4.92	Lyγ at $z_{ab} = 1.75973$
2686.52.....	2684.86–2688.00	1.16	8.88	Ly6 at $z_{ab} = 1.88641$
2689.89.....	2688.00–2692.16	1.48	11.37	C IV λ1548 at $z_{ab} = 0.73743$, part Lyβ at $z_{ab} = 1.624$?
2694.20.....	2692.16–2696.25	0.78	8.10	C IV λ1550 at $z_{ab} = 0.73733$
2707.00.....	2704.94–2709.03	0.85	9.67	Lyϵ at $z_{ab} = 1.88653$
2716.75.....	2714.66–2718.32	0.85	6.32	Lyβ at $z_{ab} = 1.64862$?, C I 1277 at $z_{ab} = 1.12704$
2719.27.....	2718.32–2720.66	0.52	3.85	
2723.33.....	2720.66–2725.40	1.00	7.42	Part Ca I λ2722 at $z_{ab} = 0.000$, part Lyγ at $z_{ab} = 1.800$
2741.74.....	2740.23–2743.80	1.11	14.42	Lyδ at $z_{ab} = 1.88682$
2770.12.....	2767.84–2771.24	0.66	6.82	
2771.95.....	2771.24–2772.95	0.42	4.36	
2777.75.....	2776.02–2779.09	0.44	5.49	Lyβ at $z_{ab} = 1.70809$?
2782.67.....	2781.65–2784.00	0.43	3.85	
2785.55.....	2784.00–2787.78	0.92	8.26	Lyβ at $z_{ab} = 1.71570$?
2794.36.....	2791.36–2796.99	2.06	21.52	Mg II λ2796 at $z_{ab} = -0.00071$, Lyβ at $z_{ab} = 1.72429$, Lyα at $z_{ab} = 1.300$?
2802.11.....	2799.54–2804.66	1.09	11.13	Mg II λ2803 at $z_{ab} = -0.00051$
2807.69.....	2805.68–2810.28	1.43	16.32	Lyγ at $z_{ab} = 1.88698$
2820.51.....	2818.98–2822.04	0.43	5.36	C III λ977 at $z_{ab} = 1.88683$?
2830.90.....	2828.18–2833.29	0.85	9.04	Lyβ at $z_{ab} = 1.75991$
2852.09.....	2850.68–2853.75	0.30	3.85	Mg I λ2852 at $z_{ab} = -0.00031$
2871.73.....	2869.60–2873.69	0.97	10.40	Lyβ at $z_{ab} = 1.79971$, Si IV λ1393 at $z_{ab} = 1.06000$
2889.81.....	2887.50–2892.10	0.44	4.20	Si IV λ1402 at $z_{ab} = 1.06007$
2899.14.....	2897.73–2900.28	0.52	6.90	Si II λ1260 at $z_{ab} = 1.30013$
2906.12.....	2905.40–2907.95	0.30	4.06	
2929.82.....	2928.41–2930.98	0.86	7.51	
2935.00.....	2930.98–2938.12	2.97	25.94	Lyα at $z_{ab} = 1.41431$
2945.81.....	2943.75–2950.57	0.80	6.95	
2950.17.....	2950.57–2953.98	3.28	28.52	Lyα at $z_{ab} = 1.42679$[a]
2960.28.....	2956.53–2963.18	2.53	28.20	Lyα at $z_{ab} = 1.435$?, part Lyβ at $z_{ab} = 1.88604$
2965.80.....	2963.69–2967.78	1.08	14.06	Lyα at $z_{ab} = 1.43964$?, part Si II λ1393 at $z_{ab} = 1.127$
2977.90.....	2975.45–2980.57	1.27	15.37	Part O IV λ1031 at $z_{ab} = 1.886$?
3001.81.....	3000.51–3003.07	0.25	3.76	
3026.33.....	3025.06–3027.61	0.29	4.17	
3044.47.....	3042.95–3045.51	0.47	5.86	
3063.32.....	3061.87–3065.06	0.69	6.23	

TABLE 5—*Continued*

λ_{vac} (mean)	λ Range	W_{obs}	S/N	Comments
3066.52.....	3065.06–3068.01	0.58	5.21	
3082.73.....	3080.28–3085.40	0.76	7.53	
3104.97.....	3101.76–3108.41	2.27	22.81	Lyα at $z_{ab} = 1.55412$
3155.24.....	3153.92–3156.15	0.50	4.94	
3157.55.....	3156.15–3159.03	0.77	7.60	
3176.35.....	3174.38–3177.95	0.61	6.29	
3182.70.....	3180.51–3184.60	0.85	8.71	
3187.82.....	3185.62–3188.10	0.65	5.60	
3189.90.....	3188.10–3191.76	1.07	10.51	Lyα at $z_{ab} = 1.62398$?, part C IV λ1548 at $z_{ab} = 1.060$
3194.54.....	3192.78–3195.85	0.44	4.93	C IV λ1550 at $z_{ab} = 1.05996$
3198.19.....	3196.88–3199.94	0.55	6.27	
3201.80.....	3200.97–3203.01	0.36	4.74	
3220.43.....	3218.22–3222.19	1.08	9.64	Lyα at $z_{ab} = 1.64910$?
3222.87.....	3222.19–3224.28	0.41	3.71	
3250.34.....	3248.99–3251.01	0.34	4.79	
3261.58.....	3258.58–3264.15	0.74	5.65	
3284.97.....	3283.22–3286.61	0.90	8.49	
3292.14.....	3289.04–3294.86	1.62	11.90	Lyα at $z_{ab} = 1.70809$?, part C IV λ1548 at $z_{ab} = 1.127$
3297.33.....	3295.83–3297.85	0.58	3.78	C IV λ1550 at $z_{ab} = 1.12625$
3300.55.....	3297.85–3303.59	3.04	19.73	Lyα at $z_{ab} = 1.71500$?
3311.46.....	3309.40–3313.77	2.29	20.52	Lyα at $z_{ab} = 1.72398$
3321.09.....	3319.10–3323.47	0.50	4.54	
3338.93.....	3338.01–3339.95	0.42	5.83	
3342.62.....	3341.89–3343.35	0.19	2.96	
3353.12.....	3351.11–3354.99	1.12	12.35	Lyα at $z_{ab} = 1.75825$
3365.81.....	3364.20–3367.10	0.71	6.80	Si IV λ1393 at $z_{ab} = 1.41492$
3368.24.....	3367.10–3371.47	0.63	6.04	
3378.79.....	3378.26–3380.20	0.34	6.27	
3387.15.....	3386.50–3387.96	0.28	6.14	Si IV λ1402 at $z_{ab} = 1.41462$
3391.61.....	3390.38–3392.81	0.34	6.38	
3395.06.....	3393.78–3396.20	0.43	8.36	
3397.38.....	3396.20–3398.63	0.28	5.35	
3403.36.....	3401.05–3405.42	2.03	33.77	Lyα at $z_{ab} = 1.79958$
3408.76.....	3407.36–3409.78	0.56	11.97	C II λ1334 at $z_{ab} = 1.55427$
3414.38.....	3412.69–3415.60	0.36	7.06	Part C I λ1656 at $z_{ab} = 1.060$?
3439.59.....	3438.39–3440.82	0.18	4.34	
3455.79.....	3453.91–3457.30	0.35	7.86	
3466.93.....	3465.55–3468.45	0.22	5.86	
3471.76.....	3470.40–3473.30	0.46	12.34	
3480.08.....	3479.12–3480.63	0.18	4.29	C I λ1277 at $z_{ab} = 1.72468$
3482.01.....	3480.63–3483.97	0.46	10.87	Si III λ1206 at $z_{ab} = 1.88604$
3486.48.....	3484.94–3487.85	0.31	9.59	
3489.95.....	3488.34–3492.22	0.34	9.85	
3499.39.....	3497.07–3500.94	0.26	7.81	Mg II λ2796 at $z_{ab} = 0.25141$?
3503.25.....	3500.94–3504.67	0.12	3.58	
3509.22.....	3506.76–3511.61	2.44	90.10	Lyα at $z_{ab} = 1.88665$, part Mg II λ2803 at $z_{ab} = 0.251$?
3519.18.....	3516.46–3520.03	0.19	4.83	
3522.60.....	3520.03–3526.16	0.65	16.26	C I λ1656 at $z_{ab} = 1.12598$
3562.26.....	3559.62–3564.95	0.17	4.85	C IV λ1548 at $z_{ab} = 1.30090$?
3571.23.....	3569.80–3572.71	0.15	5.70	Mg I λ2852 at $z_{ab} = 0.25176$?
3738.17.....	3735.51–3740.83	1.66	28.66	C IV λ1548 at $z_{ab} = 1.41452$
3744.45.....	3741.59–3747.67	1.37	21.95	C IV λ1550 at $z_{ab} = 1.41457$
3757.09.....	3754.50–3759.06	0.25	4.53	C IV λ1548 at $z_{ab} = 1.42674$
3863.55.....	3861.64–3865.43	0.19	4.01	
3925.88.....	3923.18–3929.26	0.23	4.18	
3933.23.....	3930.78–3936.10	0.36	7.02	Ca II λ3934 at $z_{ab} = -0.00039$
3954.45.....	3953.57–3955.85	0.17	4.17	C IV λ1548 at $z_{ab} = 1.55422$
3960.58.....	3958.89–3961.93	0.13	3.61	C IV λ1550 at $z_{ab} = 1.55394$
3968.30.....	3966.49–3969.53	0.14	3.51	Ca II λ3969 at $z_{ab} = -0.00033$
4140.65.....	4138.96–4142.00	0.19	4.92	
4217.86.....	4215.70–4219.50	0.17	3.91	C IV λ1548 at $z_{ab} = 1.72436$
4470.26.....	4466.44–4474.03	0.27	5.37	C IV λ1548 at $z_{ab} = 1.88739$
4517.89.....	4515.27–4518.87	0.36	6.01	C I λ1656 at $z_{ab} = 1.72667$?[c]

[a] The $z = 1.426$ system's Lyβ occurs at the Ly break at 2484Å. Ly6 at 2258Å for $z = 1.426$ is marginally detected.
[b] Fe I λ2484 is also lost in the Ly break at 2484 Å.
[c] The wavelength and strength of the 4517.89 Å line are more uncertain than implied by the S/N given the uncertainty in the continuum on the C IV emission line.

correlation signal obvious in Figure 4 of Paper III, for QSO pairs closer than 400 h^{-1} kpc persists to over 700 h^{-1} kpc in the KP triplet, despite the weakness of the signal seen in the LB pair at separation $S \approx 430\ h^{-1}$ kpc.

4.2. *Large-Scale Structure in the Lyα Distribution*

As discussed in Crotts (1989), the distributions of the three Lyα forests in the triplet can be combined into a single

TABLE 6

Lyα Samples from QSO Triplet and Pair

Parameter	QSO				
	1623+2651A (KP 76)	1623+2653 (KP 77)	1623+2651B (KP 78)	1517+2357 (LB 9605)	1517+2356 (LB 9612)
Sensitivity Ranges[a]					
z range, $W_0 \geq 0.1$ Å	1.88–2.47	1.90–2.53	1.94–2.61	1.79–1.84	1.32–1.90[b]
z range, $W_0 \geq 0.2$ Å	1.78–2.47	1.78–2.53	1.82–2.61	0.73–1.84[c]	1.06–1.90[d]
z range, $W_0 \geq 0.4$ Å	1.72–2.47	1.70–2.53	1.75–2.61	0.47–1.84	1.05–1.90
z range, $W_0 \geq 0.8$ Å	1.68–2.47	1.65–2.53	1.70–2.61	0.36–1.84	0.50–1.90
Samples used[e] for $\lambda_{\rm rest} = 1020$–$1220$ Å[f]					
≥ 0.1 Å, $N_{\rm lines,\,``pure''}$	54	60	60	34	30
≥ 0.1 Å, $N_{\rm lines,\,contaminated}$	54	62	68	35	34
≥ 0.2 Å, $N_{\rm lines,\,``pure''}$	33	39	40	26	17
≥ 0.2 Å, $N_{\rm lines,\,contaminated}$	33	41	45	27	20
≥ 0.4 Å, $N_{\rm lines,\,``pure''}$	17	19	21	15	6
≥ 0.4 Å, $N_{\rm lines,\,contaminated}$	17	19	24	16	9
≥ 0.8 Å, $N_{\rm lines,\,``pure''}$	5	8	7	4	3
≥ 0.8 Å, $N_{\rm lines,\,contaminated}$	5	8	7	3	3
Samples used[e] for extended $W_0 \geq 0.4$ Å[g]					
$N_{\rm lines,\,``pure''}$	24	24	29	...	...
$N_{\rm lines,\,contaminated}$	26	28	36	...	...

[a] Range in redshifts over which unresolved line is detected at 5.5 σ.
[b] Missing redshift range 1.690–1.723.
[c] Missing redshift range 1.689–1.756.
[d] Plus additional redshift range 0.834–0.900.
[e] Samples also described in text.
[f] For the KP triplet, the range of z overlap is 2.02–2.48 and $\langle z \rangle$ of the overlap is 2.25. For the LB pair, the range of z overlap is 1.44–1.84 and $\langle z \rangle$ of the overlap is 1.65.
[g] For the KP triplet, the range of z overlap is 1.76–2.47 and $\langle z \rangle$ of the overlap is 2.14.

probe of structures much larger than their sight-line separations of 0.5–0.7 h^{-1} Mpc. These are constructed by running bins of different widths along complete Lyα line lists, counting the number of lines in each bin. The results are shown in Figures 7*a* and 7*b* for the $W_0 > 0.4$ Å and $W_0 > 0.1$ Å samples, respectively. The bin width alternates between 15, 30, and 45 h^{-1} Mpc (for $q_0 = \frac{1}{2}$), and the bin center is stepped in redshift every $\frac{1}{4}$ of the bin width. In

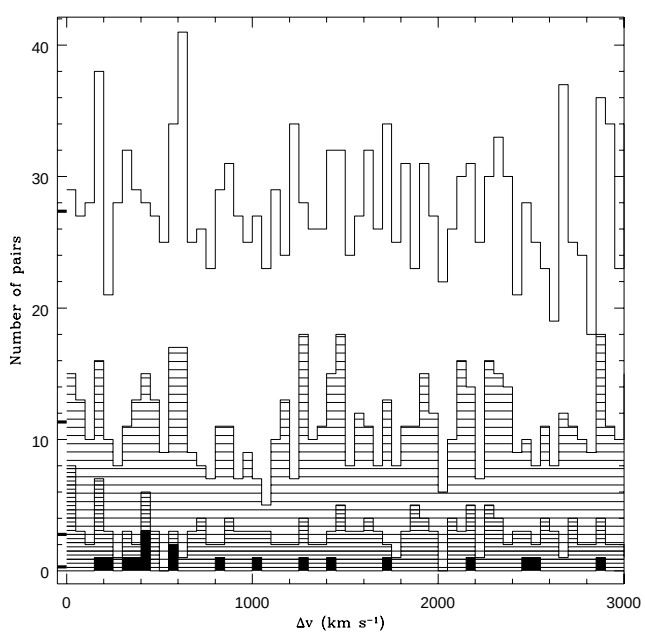

FIG. 6*a*

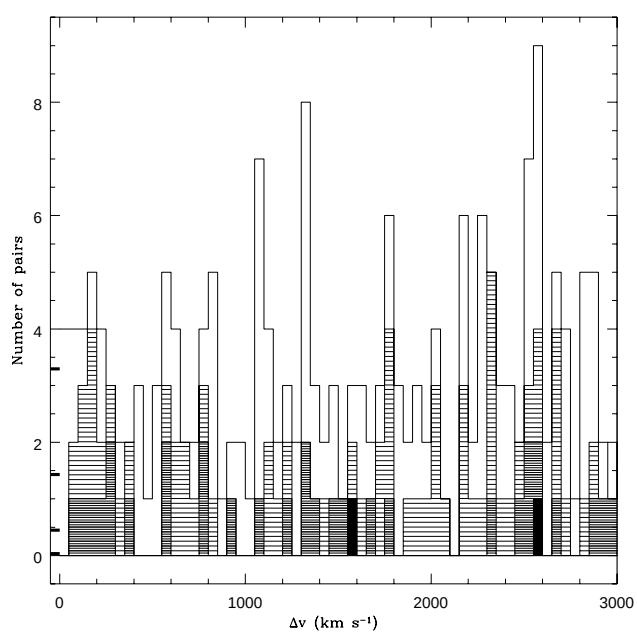

FIG. 6*b*

FIG. 6.—(*a*) Lyα forest two-point velocity cross-correlation function for all three sight-line pairs among KP 76, 77, and 78, plotted as a histogram of the number of pairs in 50 km s^{-1} bins versus velocity difference Δv. The solid bars indicate pairs where both Lyα lines are stronger than rest equivalent width $W_0 = 0.8$ Å. The densely shaded, lightly shaded, and unshaded bars show the same function for samples with $W_0 > 0.4$, 0.2, and 0.1 Å, respectively. The random pair count level for each of the W_0 levels, as $\Delta v \to 0$, is indicated by the four dark tick marks on the left edge of the graph. (*b*) Same as (*a*), but for LB 9605 and LB 9612.

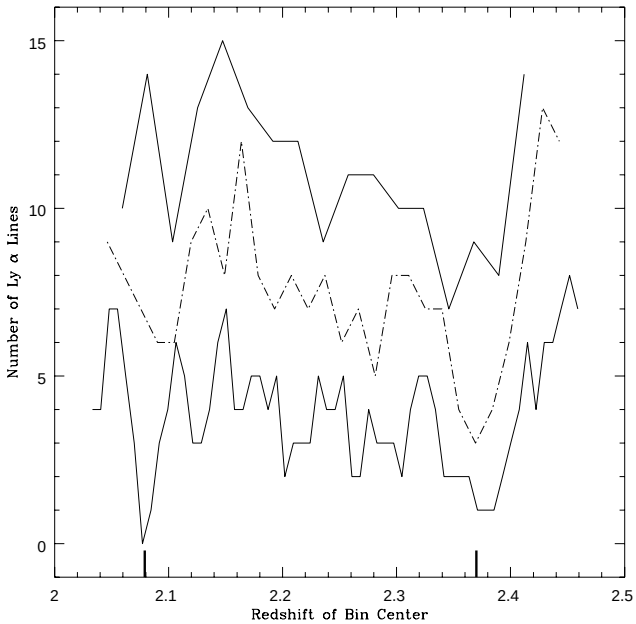

FIG. 7*a*

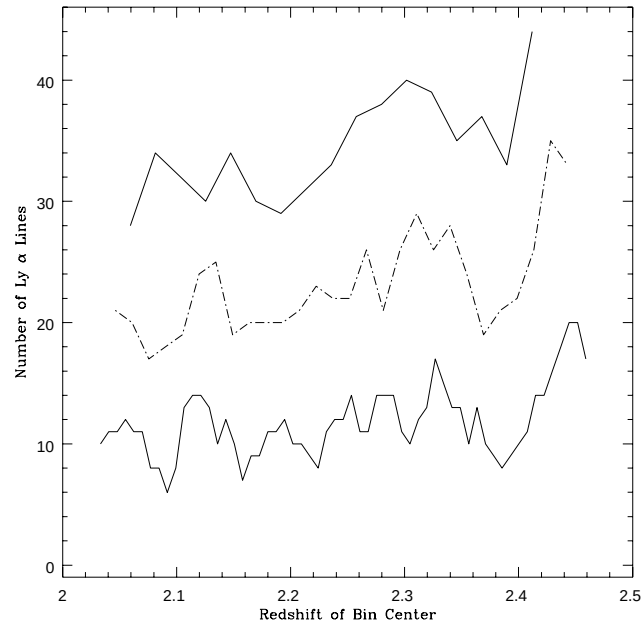

FIG. 7*b*

FIG. 7.—(*a*) Number of Lyα forest lines stronger than $W_0 = 0.4$ Å found in bins of width 15, 30, and 45 h^{-1} Mpc (*bottom solid curve*, *dashed curve*, and *top solid curve*, respectively) along the combined sight lines to KP 76, 77, and 78. The bins are stepped in redshift by 1/4 of each bin width. Note the depressions in line counts at $z \approx 2.08$ and $z \approx 2.37$, referred to in the text and indicated by the dark tick marks. (*b*) Same as in (*a*), but for lines stronger than $W_0 = 0.1$ Å.

Figure 7*a*, two prominent underdensities occur, one at $z = 2.08$ and another at $z = 2.37$; from the bin width plot in which they are most prominent, they appear to have widths of about 15 and 30 h^{-1} Mpc, respectively. How statistically significant are they? The first dips to 0 counts when the mean is 4.5 and represents one bin among 15 independent bins across the total redshift range, leading to an a priori probability of finding a void this marked because of random fluctuation at about the 17% level. The $z = 2.37$ feature drops to a count of three versus an average of eight in one 30 h^{-1} Mpc bin (versus seven independent ones), for an a priori probability of 30%.

Note that these features are of roughly the same size as underdensities seen toward other QSOs: 0420−388 (Crotts 1987; Rauch et al. 1992) and 0302−0019 (Dobrzycki & Bechtold 1991). Note that the same sort of plot for $W_0 > 0.1$ Å line (Fig. 7*b*) shows no new features, and the previously mentioned underdensities are washed out. If such structures are real, they are traced more by the stronger lines, in a way similar to the small-scale structure seen in § 4.1.

Neither of these features is significant enough to stand by itself as a detection. It is interesting nonetheless to ask if they are associated with foreground QSOs, as might be expected if several bright QSOs sit in the foreground of this triplet and thereby destroy the neutral hydrogen at their redshift, or, if voids might exist as in the galaxy distribution, bounded by walls of more condensed objects, such as, perhaps, QSOs. A search of recent QSO catalogs (see, e.g., Hewitt & Burbidge 1993) reveals one faint, possible QSO (KP 70) at $z = 2.1$(?) and another at $z = 2.4$(?) (KP 73). Both have $V \gtrsim 20$ and sit too far from the triplet in the sky (angular distances corresponding to about 6 h^{-1} Mpc and 3 h^{-1} Mpc proper separation, respectively) to be likely causes for such large voids (unless the flux we see is not representative of the flux experienced by observers in other directions, either because of variability of the QSOs or anisotropic radiation patterns). These do not seem likely to produce such underdensities because of a foreground QSO proximity effect; for this reason we are searching for other QSOs in the field (Crotts 1998).

4.3. *Foreground QSO Proximity Effect*

A more direct approach (Crotts 1989; Bajtlik et al. 1988; with correction found in Crotts 1989) to estimating the effects of QSOs on the absorbers along the sight lines to background sources is to compute the radiation field from the known, bright QSOs in the foreground and their effects on neutral hydrogen in their vicinity. This can be compared to the actual number density of lines seen toward the three background QSOs in the triplet, and the model can thus be tested. Over the relevant redshift range of interest (see Table 7), all QSO spectra are sensitive to $W_0 = 0.1$ Å. These foreground QSOs include the triplet and the $z = 2.183$, $V = 19.6$ QSO KP 79, sitting about 1.2 h^{-1} Mpc in proper distance to one side (closest to KP 77 and 78). We make the assumption that the Lyα clouds are distributed uniformly except for the general evolution of line-of-sight number density with redshift, $n(z) = N_*(1 + z)^\gamma$, where only lines with $W_0 > 0.1$ Å are counted, $\gamma = 2.1$ (intermediate between the two recent determinations of Bechtold 1994 and Lu, Wolfe, & Turnshek 1991), and N_* is adjusted to maintain equal total lines in the model and triplet sample (for $1.99 < z < 2.49$). (The measured number lands within 10% of predictions from the literature, after adjusting for different sample sensitivities.) We ignore momentarily the possibility that the proximity effect is modified by large-scale structure influencing the local number density of Lyα lines (Loeb & Eisenstein 1995).

To illustrate the correlation of observed $n(z)$ with predicted deficits of lines due to the proximity effect, we present Figure 8, which shows the general evolution of $n_\gamma(z)$ (*dotted line*) absent the effects of local radiation, the altered $n_p(z)$ (*solid curve*) predicted by the proximity model of Bajtlik et al. (1988) assuming $J_{21} = 1$, and the actually observed

TABLE 7

FOREGROUND QSO PROXIMITY EFFECT: PREDICTED VERSUS OBSERVED DENSITIES OF $W_0 > 0.1$ Å Ly α LINES

QSO	Redshift Range	Number of Lines (n)	Proximity Prediction ($\int wn_p\, dz$)	Null Model Prediction ($\int wn_\gamma\, dz$)	Observed Value ($\sum_{i=1}^{n} w_i$)	Variance ($\sum_{i=1}^{n} w_i^2$)
KP 76	2.175–2.191	2	0.150	0.163	0.166	0.014
KP 77	2.173–2.193 2.425–2.485	14	1.562	2.532	3.657	1.461
KP 78	2.173–2.193 2.435–2.574	23	4.038	7.708	7.561	3.679
KP triplet combined	(above ranges)	39	5.750	10.403	11.384	5.154
LB 9612	1.815–1.857	2	0.609	1.047	0.286	0.047
All 4 QSOs	(above ranges)	41	6.359	11.450	11.670	5.201

density of lines n_o in redshift bins selected to be equally spaced in redshift but well-placed with respect to foreground QSOs (crosses showing z intervals and 1 σ error bars in n_o). Figure 9 shows the same information for LB 9612, which has LB 9605 in the foreground, as well as a minor contribution from the $V = 18.2$, $z = 1.818$ LB 9615 sitting 9 h^{-1} Mpc to one side. Note that there is some correlation with the model n in the LB pair, but in most cases the counts and model are *anticorrelated* for the triplet. The signal involved is still small compared to the errors, so we weight the data in a more optimal way, first explained in Crotts (1989), and repeated below.

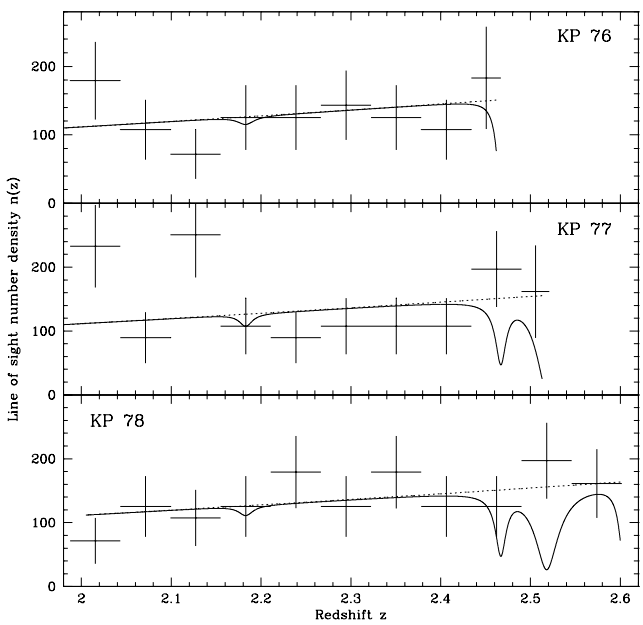

FIG. 8.—Foreground proximity effect for each QSO in the KP triplet, expressed as the number of lines per unit z as a function of redshift. The crosses show the z bin width and the 1 σ errors in the number of lines per bin as a function of midbin z. The slanted dashed line shows the mean number of lines per unit z, $n_\gamma(z)$, from a large sample of many sight lines. The solid curve shows $n_p(z)$, the expected number of lines once the ionization of foreground QSOs is included. A background ionizing flux density of $J_{21} = 0.1$ is assumed.

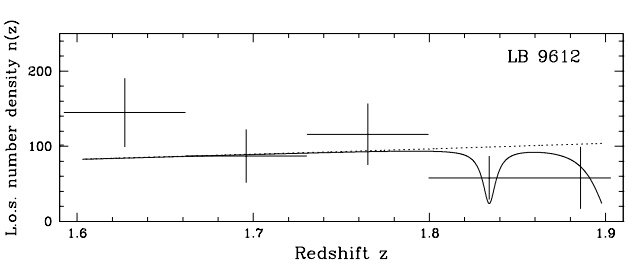

FIG. 9.—Same information as in Fig. 8, but for LB 9612

The weighting factor, applied to each line observed in the redshift interval with significant $n_\gamma - n_p$, is just the line density deficit $w = 1 - n_p/n_\gamma$ at that redshift (*not* ω from Bajtlik et al. 1988). The sum over observed lines is compared to predictions from the two models: w integrated over $n_\gamma(z)$, and w integrated over $n_p(z)$. Lines are considered and integrals calculated only over regions where $w > 0.1$. The results are shown in Table 7.

As in Crotts (1989), the observed signal is consistent with the no-proximity model and lends no support to the model including foreground ionization, being discrepant with that model at the 2.4 σ level. This result persists despite the new spectroscopy, inclusion of lines with 0.1 Å $< W_0 <$ 0.2 Å, and the addition of LB 9612. Two other papers, Dobrzycki & Bechtold (1991) and Fernández-Soto et al. (1995), bear on the foreground-QSO proximity effect. The latter detects a marginally significant signal consistent with a foreground effect, while the phenomenon seen by Dobrzycki & Bechtold is much too strong to be explained by a simple interpretation of QSO ionization effects for the brightness seen for the foreground QSO. As Loeb & Eisenstein (1995) point out, the proximity effect in the case of a single QSO can be altered by the effects of large-scale structure in the immediate vicinity of the QSO, in the sense that cluster produces more Lyα lines near the QSO's Lyα emission. This effect is strongest for faint QSOs, where ionization is weak.

Even though the QSOs studied here tend to be faint because of the requirement that they reside in close pairs, the Loeb & Eisenstein result does not explain why these might be so discrepant with the Bajtlik et al. (1988) model while bright QSOs are not. Furthermore, we have chosen a value of J_{21} that is often regarded as low. One should recall that anisotropic radiation by the QSO or long-term variability on timescales of about 10^5 yr (Crotts 1989) are potential means by which the foreground QSO proximity effect can produce a signal that is out of proportion with the observed flux, while the direct (single QSO) proximity effect involves Lyα clouds along the observed sight line to the ionizing source and photons emitted at the same time as the ionizing photons. If these factors are manifest here, a much larger sample will be needed to reveal them. The current sample does not lend additional support to the ionization interpretation of the proximity effect by way of the foreground QSO test.

4.4. *Lyα Absorber Size Estimates*

The power of QSO pairs in providing transverse information is crucial to finding the size of absorption clouds, particularly in the forest. We (Papers II and III) have constructed a simple statistical measure of cloud size based on the working assumption that Lyα are unclustered spheres of uniform radius. In Paper III, however, we show that this assumption cannot be completely accurate because the inferred cloud radius R is a function of the QSO pair separation S, contrary to the basic assumption. Much of this failure is based on the behavior of absorbers in the KP QSO triplet, which we reexamine here. Furthermore, Dinshaw et al. (1995) also consider the pair Q0107−0234/0107−0235, which is of much lower redshift than the other pairs that have been studied, and suggest that the cloud size increases with lower z. The LB pair allows us to test this possibility.

Our technique consists of an analysis of "hit" statistics, a hit consisting of a line above a set W_0 threshold detected in both sight lines of a QSO pair, with a velocity difference between the two absorption line redshifts less than a velocity difference cutoff. Figure 4 of Paper III shows that a cutoff of $\Delta v = 150$–200 km s^{-1} is strongly suggested by the presence of a strong cross-correlational signal between all published sight lines up to the scale of the KP triplet's separations and is further borne out in § 4.3 by the clustering feature at $\Delta v < 200$ km s^{-1} seen in the triplet.

When a line is seen in one QSO spectrum, but no line above the W_0 threshold is seen within 200 km s^{-1} in the other (and this can be established with greater than 3.5 σ certainty), it is registered as a "miss." (If such a situation is not established with 3.5 σ certainty, it is "null.") We assume in turn one of three cosmological models: (Ω_0, $\Lambda_0 = \Lambda/3H^2$) = (1,0), (0.1, 0), and (0.1, 0.9). In all three cases, for the relevant ranges of redshifts, we can consider the separation between sight lines to be nearly constant, with an order-unity ratio between sight-line separations (listed in Fang et al. 1996 for all QSO pairs considered here except the LB pair) for the three cosmological cases. For the LB pair, multiply the (1, 0) value by 1.38 for (0.1, 0) and 1.9 for (0.1, 0.9).

We limit our sample to lines with $W_0 \geq 0.4$ Å for all QSOs and include the "contaminated" Lyα lines for the triplet and LB pair. In Table 8, we show the Lyα forest redshift ranges, angular separations, proper separation range for (1, 0), hit and miss counts, inferred 95% confidence intervals, and median predicted cloud radii ($q_0 = 1/2$) for the QSO pairs Q1343+2640 (Papers II and III), Q0307−1931/0307−1932 (Shaver & Robertson 1983), Q0107−0234/0107−0235 (Dinshaw et al. 1995), and new values for Q1623+2651A/1623+2653/1623+2651B and Q1517+2357/1517+2356 and Q1026−0045 (see note added in proof).

The estimates for the KP triplet were computed by taking each pair of QSOs separately; strictly speaking they are not quite independent. Also, for these samples there are significant numbers of accidental hits; these are corrected as follows: we assume a Poisson distribution for the number of random hits, with the mean of $N_{\rm rand} = 11.6/3 = 3.87$ random hits per QSO pair. The number of "real" (nonrandom) hits, $N_{\rm real}$, are given by the observed number minus the random component. Since the real component must be nonnegative, that part of the distribution with $N_{\rm rand}$ greater than N_h is included in the $N_{\rm real} = 0$ bin. Each $N_{\rm real} > 0$ produces its own probability density distribution in $\mathscr{P}(R)$ (as in Paper III) while cases in which $N_{\rm real} \leq 0$ produce only an upper limit in R. [The probability distributions for cases where $N_{\rm real} \leq 0$ are taken as constant in R: $\mathscr{P}(R) = \{^{0,\ R<S/2}_{\text{constant},\ R\geq S/2}$. Fortunately, these cases are a small fraction of the total.] The median R value and corresponding R confidence intervals are computed by taking an average of the probability distributions corresponding to a different $N_{\rm real}$, weighted by this truncated Poisson distribution. The results are slightly smaller in median R, and with smaller errors, than those derived from Crotts (1989) data in Paper III.

The LB pair is particularly interesting because it lands midrange in the span of S values from preexisting pair observations but is at significantly lower redshift than average. Unlike the lower redshift pair Q0107−0234/0107−0235 (Dinshaw et al. 1995), however, it does not imply R values significantly higher for pairs at lower redshift.

Figure 10 shows the median R and confidence intervals in R (corresponding to ± 1 σ) for all QSO pairs, as a function of S. As discovered in Paper III, there is a significant trend of median estimated R with S, contrary to our assumed model. The slope in a linear fit of R versus S is 0.43 ± 0.08 for all QSO pairs. If, noting that Q0107−0234/0107−0235 appears to be discrepant, one leaves it out, one finds that the trend of R with S is almost unchanged at 0.043 ± 0.08. The other lower redshift QSO pair, Q1517+2357/1517+2356, falls *below* the trend set by higher redshift QSOs (as does Q1026−0045A/B).

With the $R(S)$ dependence removed, one finds the Q0107−0234/0107−0235 point sitting 2.3 σ above the minimum χ^2 linear fit of R versus z, with Q1517+2357/1517+2356 0.9 σ below and Q1026−0045A/B 0.8 σ below. There is only a marginally significant trend of size decrease with z (best fit $\partial R/\partial z = 21$ kpc per unit z, with an error of

TABLE 8

Lyα Cloud Radius Estimates from QSO Pairs

QSO Pair	Angular Separation (arcsec)	Lyα Range (z)	Proper Separation S (h^{-1} kpc)	N_h	N_m	95% Confidence Interval in R (h^{-1} kpc)	Median Radius R (h^{-1} kpc)
1343+2640A/B	9.5	1.756–2.035	39–40	7	1	77–841	237
1026−0045A/B	36	0.830–1.438	149–154	1	5	95–306	148
0307–1931/32	56	1.690–2.122	226–236	4	12	165–434	246
0107–0234/35	86	0.481–0.952	301–364	4	6	286–918	501
1517+2356/57	102	1.390–1.830	425–438	3	28	226–429	283
1623+2651A/B	127	2.025–2.467	493–522	6	32	264–520	340
1623+2651A/53	147	1.958–2.467	571–604	8	26	323–757	461
1623+2653/51B	177	2.025–2.526	683–721	5	36	357–675	442

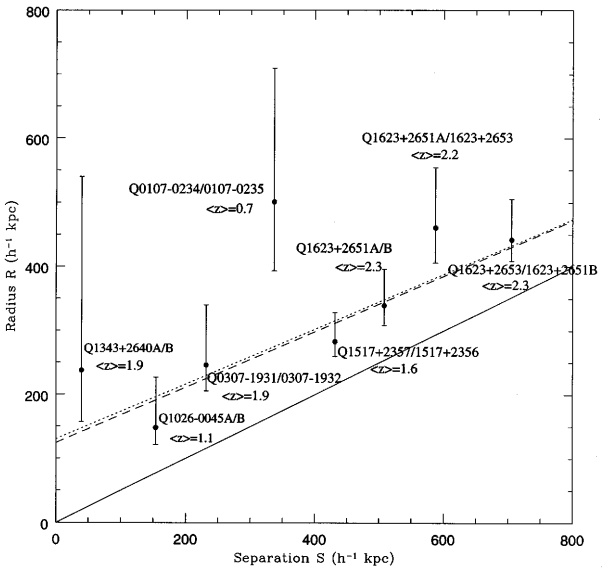

FIG. 10.—Inferred cloud radius R (and 1 σ confidence intervals) from a model assuming uniformly sized, unclustered spherical clouds, as a function of QSO pair sight-line separation S. The data from this paper for the four largest S pairs is shown, along with that of Q1343+2640A/B (Paper II), Q0107−0234/0107−0235 (Dinshaw et al. 1995), and Q0307−1931/0307−1932 (Shaver & Robertson 1983). All points must sit above the solid diagonal line if they show a significant detection, as $R > S/2$ in order for such clouds to span the sight lines. The best linear fit to $R(S)$ is shown by the dotted line for all six pairs, and by the dashed line once the lowest z pair Q0107−0234/0107−0235 is excluded.

35 kpc per unit z). While Q0107−0234/0107−0235 suggests a trend of R with z, this trend is not supported by any other data, and Q0107−0234/0107−0235 alone is insufficient to establish an effect. Perhaps $R(z)$ changes more rapidly at smaller z than at larger, but more data from close, low-redshift QSO pairs would be needed to substantiate this.

Paper III shows that there are at least three viable alternatives for the dependence of R on S: small scale clustering, elongated clouds (filaments) and a nonuniform R value among the clouds. From a few QSO pairs alone, it is very difficult to distinguish which of these, or which combination, is in play. The triplet data, however, is used below to probe the shape of Lyα forest clouds.

4.5. *Elongated Absorbers*

It is also possible to use "hit" statistics to test directly the nonspherical models. For instance, we can ask if Lyα absorbers are elongated by simulating the projection of a simple shape against the sky in an isotropic collection of orientations. Paper III suggests elongation of the clouds into filaments as one of several possible explanations for a dependence of inferred cloud size R from our Bayesian model on sight-line separation S. Furthermore, numerical models of intergalactic objects in the early Universe (Zhang et al. 1995; Katz et al. 1996; Miralda-Escudé et al. 1996) tend to find elongated structures on the scale of several hundred kpc as those with properties most similar to those of Lyα clouds. This should be contrasted to purely gravitational simulations, e.g., Shandarin et al. (1995), which tend to produce sheetlike structures first. The triplet is ideal for determining whether the hit statistics deviate from an S-independent R due primarily to elongated clouds; single, long, thin filaments are incapable of intercepting all three sight lines. QSO triplets carry with them the potential to measure the aspect ratio of filaments, $a = l/2R$, and R independently (where R is the cross-sectional radius, and l is the length of the filament).

One possibility that we do not discuss in this subsection are sheets or disks ($a < 1$), since their behavior in terms of hit statistics is similar to that of spheres of slightly smaller radius (Paper III) in the case of sight-line pairs. This is still true for triple sight-line hits. As $a \to 0$, the utility of the triple sight-line approach is to distinguish the face-on projected shape of the disk, which we judge to be a less interesting problem. We discuss other test for disklike structure in §§ 4.7 and 4.8. Here we pursue the following question: are the two- and three-way hit statistics in the QSO triplet consistent with elongated, circular–cross sectioned rods of some radius R and aspect ratio a? This is motivated by the realization that long, thin filaments cannot span all three sight lines (if the minimum distance across their triangle projected onto the sky is larger than the width of the filament), whereas a circular cloud of the same volume as the filament might easily do so. Such an effect should be expressible as the probability of clouds of a given shape and size hitting two or all three sight lines whenever they hit one. This is accomplished by, first, measuring in the actual spectra's line lists the probabilities P_{ab}, P_{ac}, P_{bc}, and P_{abc}, (defined as P_{ab} being the probability of a line in A resulting in a hit in B, or vice versa, and likewise for the other probabilities) and, secondly, simulating the same probabilities by a numerical simulation of cylindrical rods of various a and R values oriented in an isotropic distribution and intercepting (or not) two or three sight lines with the same spacings as those between KP 76, 77, and 78 (sight lines "A," "B," and "C," respectively).

For this test, we need the largest sample possible, hence for $W_0 > 0.4$ Å, the $\langle z \rangle = 2.14$ sample. As a preliminary indication, consider that of the 29 $W_0 > 0.4$ Å hits, some 15.6 are expected at random. Consider also the large number of "multiple hits" of two or three pairs between all three sight lines involving the same Lyα clouds, at $z = 1.938$ (three pairs involving three lines in all three QSO spectra), $z = 2.042$ (three pairs, three lines, three QSOs), $z = 2.113$ (three lines, two pairs, three QSOs), $z = 2.138$ (three lines, three pairs, three QSOs), and $z = 2.183$ (three lines, three pairs, three QSOs), for a total of fourteen pairs. In other words, the entire excess in $\Delta v < 200$ km s^{-1}, $W_0 > 0.4$ Å pairs might be due to these five groupings. This, even by itself, argues for clouds that are not simply long, thin filaments (in comparison to the sight-line separations), since such clouds cannot span the three sight lines.

The probabilities P_{ab}, P_{ac}, and P_{bc} are computed by counting the number of relevant pairs and dividing by the geometric mean of the number of lines in each sight line's sample that is involved (23, 24, and 29 in KP 76, 77, and 78, respectively, for $W_0 > 0.4$ Å), eliminating the fraction of pairs that are expected at random (reduced to a fraction of 13.4/29 of the original). Errors are computed from the Poisson distribution around a mean equaling the actual number of observed hits. For three-way hits (P_{abc}), since any given line has a 35% chance of being accidentally involved in a hit, the probability is reduced by this fraction. Errors are computed to first order by considering the Poisson statistics for the multiple hits (since they are likely not chance events) and in the sample size, then adding in quadrature

the error in false hits, leading to the 68% confidence interval (corresponding to $\pm 1\ \sigma$) assigned to each probability: $P_{ab} = 0.30^{+0.19}_{-0.15}$, $P_{ac} = 0.18^{+0.16}_{-0.12}$, $P_{bc} = 0.06^{+0.14}_{-0.10}$, and $P_{abc} = 0.16^{+0.14}_{-0.10}$. Formally, P_{bc} cannot be less than zero, nor can it be smaller than P_{abc}; its small value appears to be a result of an unusually small number of random hits in BC. If we compute the probabilities in a different way, by recognizing that triple hits are almost certainly real (not accidental) and that the remaining number of real hits must be nonnegative, this produces a new set of probabilities for the pairs of sight lines: $P'_{ab} = 0.24^{+0.20}_{-0.13}$, $P'_{ac} = 0.12^{+0.13}_{-0.12}$, and $P'_{bc} = 0.15^{+0.13}_{-0.11}$. Normally (if the clouds are oriented isotropically and parcels of gas within the cloud have a two-point correlation function that decreases monotonically with separation), one should expect $P'_{ac} \geq P'_{ab} \geq P'_{bc}$. The probability P'_{ac} disobeys this most significantly; we will encounter this again below.

As a comparison, we produce a model of a single, rotating, translating cylinder (of circular cross section) that is stepped in a fine grid (10 h^{-1} kpc in two orthogonal directions perpendicular to the sight line) across three sight lines with the same spacing as the triplet. The rod is "hard edged" with no variation in W_0 over its projected shape. The rod is made to point in 1280 isotropically distributed directions at each grid point. This simulation is done for rods with cross-sectional radii R that are positive multiples of 25 h^{-1} kpc up to 500 h^{-1} kpc (in proper coordinates), and for aspect ratios (length divided by diameter) of positive integral values up to 20. For each rod shape, size, orientation, and translation, the hit on one, two, or three sight lines, A, B, C, AB, AC, BC, or ABC, is evaluated. For each translational grid, the number of one-way hits are required to be all equal, $N_a = N_b = N_c$. The probabilities are computed for each rod shape and size by $P_{ab} = N_{ab}/N_a$, ..., $P_{abc} = N_{abc}/N_a$. Example contour plots (unsmoothed) of two of these probabilities, P_{ab} and P_{abc}, respectively, are shown in Figures 11*a* and 11*b*. P_{ac} and P_{bc} resemble P_{ab}, qualitatively, while P_{abc}, containing information about the shape, is more distinct, going to zero for $2R < 406\ h^{-1}$ kpc, the minimum distance across the triangle described by the triplet. The contours at $P = 0.01$ show a few ripples at the level of about 0.002, indicating the degree of discreteness error in the model.

The contours for the calculated value for each probability P_{ab}, etc. (*solid curves*) and a confidence interval (68%; *dotted curves*) are plotted in Figure 12*a*. The same for P'_{ab}, etc., is plotted in Figure 12*b*. The probability P_{abc} is inconsistent with the mean of the two-way probabilities P_{ab}, P_{ac}, P_{bc} at a level greater than 1 σ for any aspect ratio $a > 4$ (accounting for the errors in all P). For $a \lesssim 2$, in both plots, P_{abc} is consistent with P_{ab} and P_{bc} (or P'_{ab} and P'_{bc}) at a level less than 1 σ. For P_{ac} (or P'_{ac}), however, the disagreement with P_{abc} is of the order of 1–2 σ even for $a \lesssim 2$. As noted above, P_{ac} is anomalously low relative to the other probabilities, and this is reflected here. Also, the statistical significance of the difference between large and small a is not great, decreasing from a maximum 1.2 σ for large a to 0.6–0.7 σ for $a < 2$. Nevertheless, all probabilities have best agreement for $1 < a < 3$ and 198 h^{-1} kpc $< R < 510\ h^{-1}$ kpc (larger R at smaller a), where $\sigma < 0.8$ (weighting the three two-way probabilities at two-thirds that of P_{abc}).

The result that the longest dimension across these absorbers exceeds somewhat 700 h^{-1} kpc is guaranteed by the observation that there are significant numbers of hits between the sight lines, plus the assumptions of the model. The derived shape and size must span the sight lines; however, the way in which it does so—by long, thin clouds or large near-spheres—depends on the relative number of three-way hits. We conclude that unclustered filaments alone are less likely to explain our shape information on the $W_0 > 0.4$ Å Lyα forest. The absorbers are more likely to be nearly circular in cross section (disks or spheroids), or, if elongated, their hit behavior on the scale of hundreds of kiloparsecs must be dominated by clustering of filaments, not the shape of the filaments themselves.

Obviously, given Figure 6, no such $\Delta v \leq 200$ km s^{-1} triple hits exist for the $W_0 > 0.8$ Å sample. Expanding the velocity interval corresponding to a hit to 600 km s^{-1}, the interval of possible $W_0 > 0.8$ Å clustering seen in Figure 6, we find one triple hit ($z = 2.05665$, $W_0 = 0.86$ Å in KP76; $z = 2.05506$, $W_0 = 1.24$ Å and $z = 2.05056$, $W_0 = 1.77$ Å in KP77; $z = 2.06117$ Å in KP78), being composed of four lines, not just three. This feature is completely independent of the $\Delta v \leq 200$ km s^{-1}, $W_0 > 0.4$ Å triple hits above and contributes one hit to the P_{ab}, $W_0 > 0.4$ Å signal. It is spread over 1040 km s^{-1}; this is about 6 times the Hubble flow

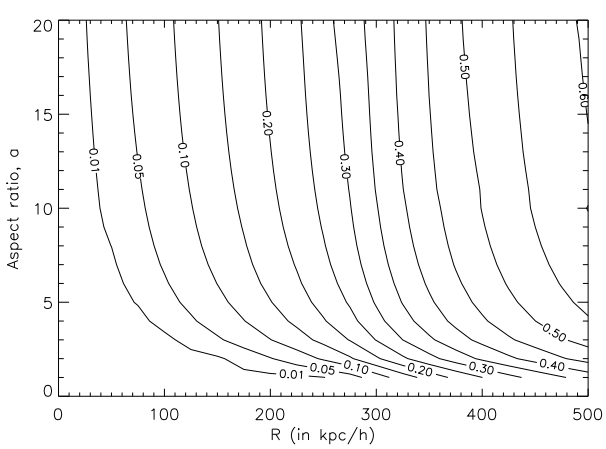

FIG. 11*a*

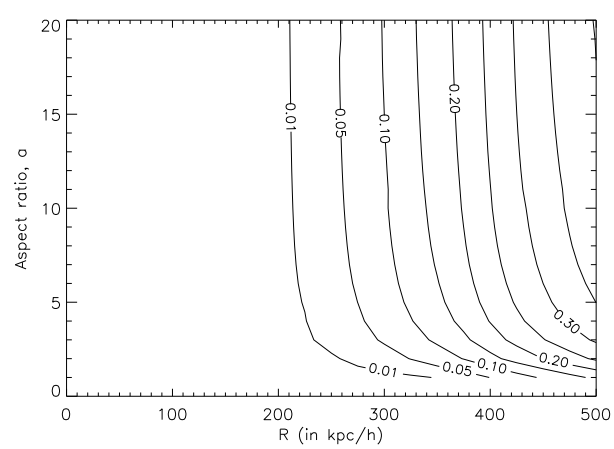

FIG. 11*b*

FIG. 11.—(*a*) Contour plot of the probability P_{ab} of a cloud intercepting both the KP 76 and 77 sight lines if it is a cylinder of cross-sectional radius R and aspect ratio $a = l/2R$ for cylinder length l. (*b*) Same as (*a*), but for the probability P_{abc} of a cloud intercepting all three sight lines to KP 76, 77, and 78.

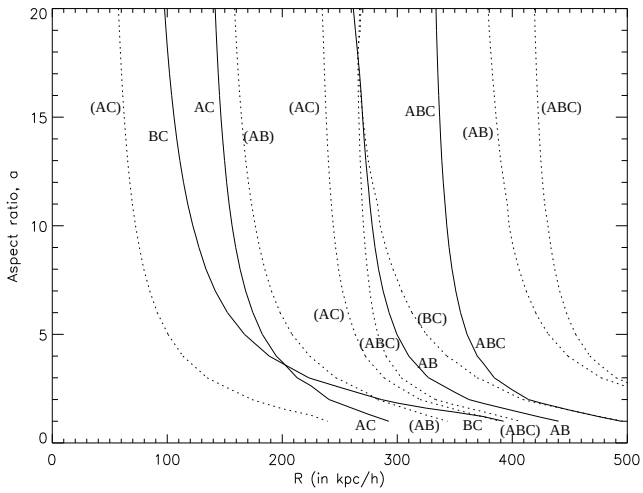

FIG. 12*a*

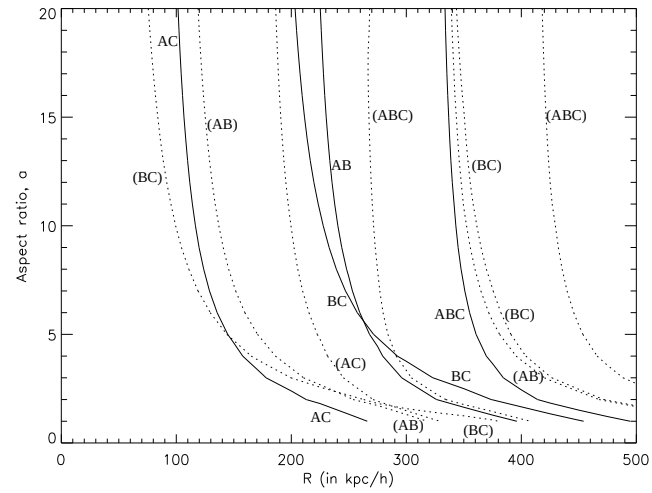

FIG. 12*b*

FIG. 12.—(*a*) Measured values and 68% confidence intervals for P_{ab}, P_{ac}, P_{bc}, and P_{abc} plotted on the same contours as shown in Fig. 11. (*b*) Measured values and 68% confidence intervals for P'_{ab}, P'_{ac}, P'_{bc}, and P_{abc} plotted on the same contours as shown in Fig. 11.

across the transverse dimension of the QSO triplet. We should note, however, that we would expect approximately 2.1 such triple hits at random in this sample, so there is little to be concluded from this datum.

Likewise, even though there is a statistically insignificant excess in two-way hits in the $0.2 < W_0 \leq 0.4$ Å sample, this might mask a more significant three-way signal. In truth, there is a slight deficit in such three-way hits compared to the random expectation, so we can conclude little, except that P_{abc} is likely smaller for 0.2 Å $< W_0 \leq 0.4$ Å than for the $W_0 > 0.4$ Å sample.

4.6. *Consistency of Triplet Hits with Spherical Absorbers*

Are spheres of different R required to explain P_{ab}, P_{ac}, P_{bc}, and P_{abc}? Or is a distribution of spheres of different radii even consistent with the data? Figure 13 shows how the four probabilities vary for a given uniform R value common to the whole population of spherical clouds. A single R value should be consistent with the 95% upper limits on all three P' values and P_{abc}. This implies an upper limit $R < 468\ h^{-1}$ kpc from P'_{ac}. On the other hand, all of the two-way probabilities (P_{ab}, P_{ac}, P_{bc}, P'_{ab}, P'_{ac}, P'_{bc}) are roughly equal, a condition of large ($R > 600\ h^{-1}$ kpc) clouds. For such large clouds, however, P values are much larger ($\gtrsim 0.3$). In order for both the ratio in P values and their rough magnitudes to be satisfied by a distribution of spheres of varying radii, a subpopulation of $R > 600\ h^{-1}$ kpc clouds must be diluted by a larger portion ($\sim$50%–70% of the total cross section) of smaller clouds that do not span the sight lines and hence do not contribute significantly to hit counts. These reduce all P values by the proportion between the cloud subpopulations' total cross section but keep the ratios of various P values intact at their $R > 600\ h^{-1}$ kpc ratios. Such a spectrum of cloud sizes is consistent with our previous constraints (Paper III) on a power-law distribution of spherical cloud radii, which we do not rederive here. We have not yet managed to challenge this hypothesis on the basis of measured cloud parameters.

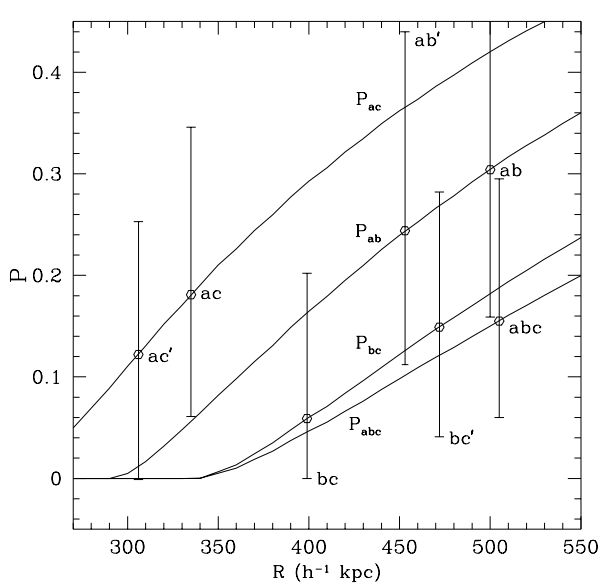

FIG. 13.—Measured values and 68% confidence intervals for probabilities P_{ab}, P_{ac}, P_{bc}, P'_{ab}, P'_{ac}, P'_{bc}, and P_{abc} as a function of spherical cloud radius.

4.7. *Kinematics of Flattened Absorbers in the Hubble Flow*

While it is difficult with hit statistics to distinguish disks from spheres, we can use the Hubble expansion to probe the probable shape of a cloud. Starting as an object expanding nearly as fast as the rest of the Universe, the absorber may collapse in one or two dimensions while still expanding in an orthogonal one. We can then distinguish a filamentary or sheetlike object by the tilt of the direction of expansion relative to the line of sight, with one side expanding toward the observer while the other recedes.

The three sight lines of the triplet rest on a circle 189″.7 in diameter, separated in the sky by 90°, 110°, and 160° with respect to the center, close enough to equilateral to always sense most of the velocity shear across the circle for an expanding absorber. For the five triple-hit objects, we find the best fit in magnitude and angle of the line of nodes for this shear pattern, and we find maximum velocities across the circle's radius of 20, 35, 175, 65, and 95 km s^{-1} (to the nearest 5 km s^{-1}) for the $z = 1.938$, 2.043, 2.113, 2.138, and 2.183 objects, respectively.

In comparison, the Hubble expansion across this radius at $z \approx 2.1$ is about 165 km s^{-1} (to within about 20% for the cosmological models we consider), whereas various inclination angles i can project this to zero or nearly infinite velocities. Figure 14 shows the expected cumulative distribution of shear velocities for a sheet expanding in the Hubble flow, for a random distribution of i values, and for our three cosmological models. A mean measurement uncertainty of 20 km s^{-1} is folded into the $v_{\max}$ distribution.

Figure 14 allows us to use a one-sample Kolmogorov-Smirnov (K-S) test to determine whether the observed $v_{\max}$ distribution is consistent with theoretical expectation. For the three cosmological models, (1, 0), (0.1, 0), and (0.1, 0.9), respectively, the null hypothesis (consistency with Hubble expansion within sheets or disks), cannot be rejected, at levels of 50%, 70%, and 99%, in the sense that (0.1, 0.9) is more consistent. The K-S test does not reject a model based on expanding sheets, while elongated filaments encounter difficulty in § 4.5. Likewise, we cannot reject a simple Gaussian distribution of velocities. We need a few times as many such measurements to discriminate between these two models.

A further prediction of the sheet model is a correlation between $v_{\max}$ and W_0, which might be evident unless the perpendicular column density through different absorbers or along different sight lines in the same cloud shows scatter greater than about order unity. Such a correlation should be a proportionality, or at least monotonic, and hence susceptible to a rank-order test. We choose the median W_0 value of all lines contributing to the triple hit objects. The results from Spearman's Rank Correlation test shows that the $W_0 > 0.4$ Å sample is consistent with a monotonic $v_{\max}(W_0)$ at the 72% confidence level. When the $W_0 > 0.8$ Å triple hit is included, however, the confident level becomes 93%, suggestive of the tilt of the absorber being an important parameter. We should note that when the same test is applied to two-way hits, however, no such correlation is seen. This may suggest that three-way hits must be required to bring this correlation out of the noise, or that the objects that span the three sight lines are sheetlike.

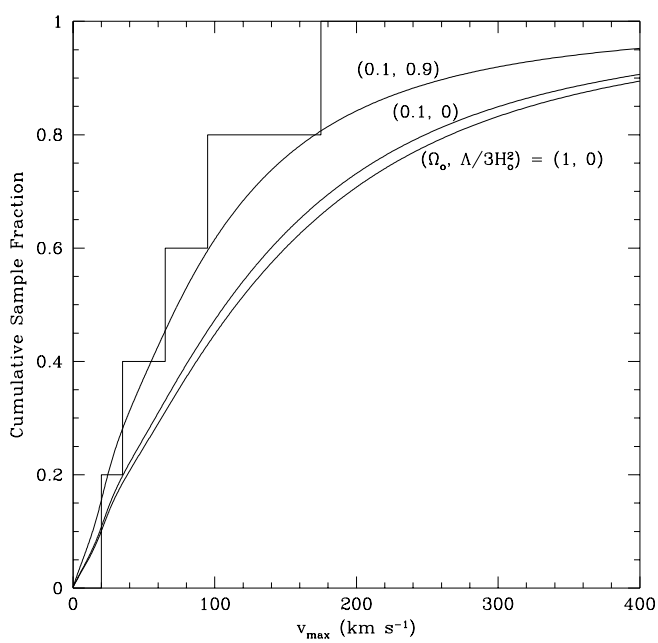

FIG. 14.—Cumulative histogram plot of the shear velocity $v_{\max}$ inferred for the four objects spanning the KP triplet sight lines as a function of $v_{\max}$, along with the expected plots of the same quantity expected for sheets expanding in the Hubble flow according to three Freidman cosmological models.

4.8. *Other Tests of Lyα Absorber Shape, Size, and Clustering*

In the § 1, we review the several recent theoretical works proposing observational tests involving pairs of sight lines. Most of these can be applied to the current data, and we consider them in turn.

Many of these tests involve figures published in the four theoretical works. While we present our data here in a form that can be compared most directly to these other results, we avoid reproducing all of their relevant figures, and refer the reader to the original papers (Cen & Simcoe 1997; Charlton et al. 1995, 1997; Miralda-Escudé et al. 1996). Additionally, Charlton et al. (1997) discuss other kinematical tests similar to those considered in the previous sections, which we will not rediscuss here.

4.8.1. *Correlated Flux between Sight Lines (Miralda-Escudé et al. 1996)*

Miralda-Escudé et al. (1996) consider the correlation of Lyα absorption as a function of transverse separation between adjacent sight lines. This is expressed purely in terms of the correlation of the transmitted flux between sight lines, not correlated line detections as in this paper. They define a correlation coefficient $\xi_f(\Delta v, \Delta r)$ (*not* a two-point correlation function as usually defined) which describes the correlation between the transmitted flux F in two adjacent sight lines: $\xi_f(\Delta v, \Delta r) = \langle [F(r, v_0) - \langle F(r, v)\rangle_v][F(r + \Delta r, v_0 + \Delta v) - \langle F(r + \Delta r, v)\rangle_v]\rangle_r / (\langle F^2\rangle_{v,r} - \langle F\rangle^2_{v,r})$, where, for instance, $\langle F(r, v)\rangle_v$ refers to the expectation value of F along a sight line at location r on the sky, averaging over the sight line (which is parameterized by velocity v along the sight line. Note that Δr corresponds to our S.) Necessarily, $-1 < \xi_f < 1$ and $\xi_f \to 1$ for $\Delta v \to 0$ and $\Delta r \to 0$. They show (in their Fig. 13) that $\xi_f(\Delta v, \Delta r)$ drops to about 0.5 of its peak ($\Delta v = 0$) value at $\Delta v \approx 60$–120 km s^{-1} for various Δr and drops close to zero for $\Delta v \gtrsim 250$ km s^{-1} (less than 0.1 for $\Delta v \gtrsim 130$ km s^{-1}), regardless of Δr. The peak at $\Delta v = 0$ falls to 0.5 at 100 h^{-1} kpc (proper separation) and to 0.17 at the largest Δr shown, 418 h^{-1} kpc. While this prediction does not quite extend to Δr values for the KP triplet, 496–720 h^{-1} kpc, it is reasonably securely extrapolated to $\xi_f \approx 0.06$ at $\Delta r = 599$ h^{-1} kpc, the mean for the triplet. All of these values apply at $z = 3$.

Since we do not resolve most of the Lyα forest, we cannot compute ξ_f directly. We take this opportunity to note that analysis of theoretical models of the high-redshift neutral hydrogen distribution should continue to consider the alternative approach of correlated line detections. Here and in many potential cases in the future, QSOs in close pairs are sufficiently faint that lines can be detected but not usefully resolved, even with 8–10 m class telescopes. Nevertheless, we can compute the statistical moments of F, e.g., $\langle F(r, v)\rangle_v$ and $\langle F^2(r, v)\rangle_v$, since we also have high-resolution Keck HIRES data for KP 77 (Crotts et al. 1997), finding $\langle F\rangle_v = 0.725$ and $\langle F^2\rangle_v = 0.807$. (Note that we cannot take the expectation over r, of course.) For the $W_0 \geq 0.4$ Å lines in this sample, not all covered by the HIRES data, we attempt to translate our data on absorption lines into measures of the correlation of actual flux, treating Lyα forest spectra as continuous functions in wavelength rather than discrete

lines. This is accomplished by considering only the lines with $W_0 \geq 0.4$ Å, since the rest are uncorrelated. These lines are replaced with Voigt profiles of the same W_0 and an assumed value of the Doppler parameter $b = 30$ km s^{-1}. (The result is fairly insensitive to the adopted b value.) This results in the value measured from our $\langle z \rangle = 2.14$, $W_0 \geq 0.4$ Å KP sample of $\xi_f(\Delta v = 0, \Delta r = 599\ h^{-1}$ kpc$) = 0.069$, with 1 σ errors of about 0.01. This value is consistent with the theoretical $\xi_f \approx 0.06$.

When we attempt the same calculation for the close pair 1343+2640A/B at $\langle z \rangle = 1.86$, we find $\xi_f(\Delta v = 0, \Delta r = 40\ h^{-1}$ kpc$) \approx 0.40$, with 1 σ errors of about 0.05. This should be compared to a model prediction of about 0.8. This difference is due in part to the fact that we have ignored weaker lines, but even in 1343+2640A/B these are more weakly correlated, as we consider in the § 5. Most likely, the measured value remains smaller than predicted, most likely $\xi_f(\Delta v = 0, \Delta r = 40\ h^{-1}$ kpc$) \lesssim 0.6$.

4.8.2. *Fraction of Coincident Lines versus* Δr and Δv (*Cen & Simcoe 1997*)

Cen & Simcoe (1997) use the same simulation as Miralda-Escudé et al. (1996) to study the nature of individual clouds of H I, over redshifts $2 < z < 4$. They study clouds as defined by regions isolated by different threshold baryonic density cuts expressed in terms of mean baryonic density $\rho(x)/\langle \rho \gg \rho_{\rm cut} = 3$, 10, or 30, values chosen by the authors. They find clouds that are relatively round and small (mean radii $\approx 23\ h^{-1}$ kpc for $\rho_{\rm cut} = 10$ and 33 h^{-1} kpc for $\rho_{\rm cut} = 30$, and commonly with axis ratios of about 1:2:4 or, a smaller fraction of the time, closer to spherical). They also argue that on scales larger than these mean diameters, any observed hits in adjacent sight lines are due to clustering of clouds, not cloud structure itself. Nevertheless, it is clear from the contours at lower ρ that larger, more sheetlike or filamentary chains of clouds are also present in the simulation, on scales up to nearly the simulation box size of 2.5 h^{-1} Mpc (proper) at $z = 3$. For comparison with observations, they state that $\rho_{\rm cut} = 10$ in their simulation corresponds to $N_{\rm H\,I} = 1.1 \times 10^{14}$ cm^{-2}, or $W_0 = 0.29$ Å for $b = 30$ km s^{-1}, which together with the corresponding value for $\rho_{\rm cut} = 30$, $W_0 = 0.47$ Å, straddles our limit $W_0 = 0.4$ Å.

In close analogy to our Figure 10 and Table 8, Cen & Simcoe present their Figure 9, which describes the fraction (compared to all lines) of lines coincident between QSO sight lines as a function of proper transverse separation Δr and velocity "hit" window width Δv. We find that the line correspondence ratio (corresponding to the ordinate of their Fig. 9) is $N_{\rm co}/N_{\rm tot} = 0.93 \pm 0.06$, 0.29 ± 0.17, 0.40 ± 0.11, 0.57 ± 0.13, 0.18 ± 0.06, 0.38 ± 0.07, 0.27 ± 0.07, and 0.22 ± 0.06, respectively, for the pairs listed in Table 8, in order of increasing separation, with rms binomial error shown. This is computed considering that a hit corresponds to two lines in the sample. A comparison with the $\Delta v = 150$ km s^{-1}, $\rho_{\rm cut} = 10$ or 30 curves from Figure 9 of Cen & Simcoe shows that all pairs, with the possible exception of Q1026−0045A/B and the LB pair (with $N_{\rm co}/N_{\rm tot} = 0.18$ at $\Delta r = 432\ h^{-1}$ kpc, which falls off of the graph in Δr), lie at least 1 σ above the highest corresponding theoretical curve. (The KP points are also off of the graph but seem to lie at least 1 σ above, as well.) While we use $\Delta v = 200$ km s^{-1} in Table 8, the effect of this over $\Delta v = 150$ km s^{-1} is small compared to the difference between theoretical and measured results. Furthermore, Cen & Simcoe's Figure 9 applies to $z = 3$, but their Figure 10 shows that $N_{\rm co}/N_{\rm tot}$ does not grow at all between $z = 3$ at the typical redshifts $z \approx 2$ of the sample in Table 8. The simulated absorption lines are less correlated between sight lines than the observed ones.

This general result for $N_{\rm co}/N_{\rm tot}$ is consistent with the small $\xi_f(\Delta v = 0, \Delta r = 40\ h^{-1}$ kpc) result of Miralda-Escudé et al. (1996), which is not surprising given their use of the same model. Casting this in terms of the small clouds delineated by Cen & Simcoe (1997), one tends to conclude that more power is needed in their model on wavelengths of $\sim$100–1000 h^{-1} kpc, which is slightly smaller than the proper size of the simulation volume of 2.5 h^{-1} Mpc at $z = 3$.

4.8.3. *Spatial Clustering of Ly*α *Absorbers* (*Cen & Simcoe 1997*)

Cen & Simcoe (1997) plot the cloud two-point correlation function $\xi(r)$, where r is the comoving separation between absorbers, in their Figure 14. Our measurement of clustering in the KP triplet at separations $\langle S \rangle = 599\ h^{-1}$ kpc, plus a line-of-sight component $\Delta v = 200$ km s^{-1} yields a typical proper separation of 625 h^{-1} kpc. At $z = 3$ this produces $\xi = 0.19$ and 0.27, for $\rho_{\rm cut} = 10$ and 30, respectively. Our measurement of ξ was made at a different redshift $\langle z \rangle = 2.14$, but Figure 15 of Cen & Simcoe (1997) allows us to account for the evolution of clustering power from $z = 3$ to 2.14, between which the correlation length r_0 increases by about 10%. Given a correlation function $\xi \propto r^{-1.8}$, the value of ξ at a proper separation of 625 h^{-1} kpc should increase by about 18%. Since we measure a value at this separation of $\xi = 1.88^{+0.78}_{-0.50}$, we find that the $\rho_{\rm cut} = 30$ model result and the actual measurement are inconsistent at about the 3 σ level. This may also be due to the lack of longer wavelength modes in the clustering power spectrum, as Cen & Simcoe (1997) also speculated.

4.8.4. *Fraction of Coincident Lines versus* Δr *and* Δv (*Charlton et al. 1997*)

Like Cen & Simcoe (1997), Charlton et al. (1997) consider model simulations (Zhang et al. 1995) to construct statistical measures that can be compared to observations. Also like Cen & Simcoe, they discuss how the fraction of common lines varies with sight-line separation S (their D). Their Figure 2*e* corresponds most closely to our sample, with $z = 2$ and a curve at $N_{\rm H\,I} = 10^{14}$ cm^{-2}. This value of $N_{\rm H\,I}$ is slightly smaller than our $W_0 = 0.4$ Å cutoff for typical b values. The values of $N_{\rm co}/N_{\rm tot}$ (their $f_{\rm co}$) listed above for $z \approx 2$ samples (excluding 0.57 for 0107−0234/35) all scatter within 1 σ of the theoretical curve, except for 1517+2356/57, which is too low, and the adjacent value, 1623+2651A/B, which is too high. All six QSO pairs, taken together, are consistent with this curve and have residuals that are might arise from a reasonable χ^2 distribution.

4.8.5. *Median Absorber Size Implied from Hit Statistics* (*Charlton et al. 1997*)

Charlton et al. (1997) study how the sizes of clouds implied by hit statistics change with pair separation for the structures within the numerical model (Anninos et al. 1994, 1997). This implied size depends on whether one assumes a sphere or thin-disk shape as a working model for the clouds. Figure 3 of Charlton et al. (1997) corresponds closely to our Figure 10. Unfortunately, none of their subfigures correspond exactly, but their Figure 3*f* is a close match, using

$\Delta v = 150$ km s^{-1} instead of 200 km s^{-1} and disks instead of spheres. From Paper III, however, results for spheres can be converted to disks by multiplying by a factor of about 1.5. With this adjustment, all $z \approx 2$ pairs fall within about 1 σ of the theoretical curve, with the small S curve slightly undercutting the observed values.

4.8.6. *Line-Strength Correlation between Sight Lines (Charlton et al. 1995, 1997)*

In Charlton et al. (1995) a codistribution of column densities (N_a and N_b) for adjacent sight lines a and b of various separations is considered for various idealized disk-shape cloud models, whereas in Charlton et al. (1997) the same test is applied to the model simulation of Zhang et al. (1995). In the first case, they consider separations up to the cloud diameter, with the best discrimination occurring for separation less than about the cloud radius. In the second paper, they consider proper separations up to 200 h^{-1} kpc. Given the separation range of the theoretical effect, 1343+2640A/B and 0307−1931/32 are most valuable comparison among observed pairs. We will also consider the KP triplet. Following Paper III, it is wise to consider only those lines thought to be unlikely to be contaminated by interloping metal lines, and with a S/N = 3.5 cutoff imposed.

Again, our data are expressed in terms of W_0, not $N_{\rm H\,I}$, so we must assume a value for b (of 30 km s^{-1}), which will introduce scatter into the transformation between W_0 and $N_{\rm H\,I}$. Fortunately, Charlton et al. (1997) also recompute the effect in terms of the difference of equivalent widths $|W_a - W_b|$ versus the strength of the strongest line max (W_a, W_b) (their Fig. 5), which is directly comparable to Figure 2*b* of Paper III (except for the two distributions corresponding to slightly different S values, 40 h^{-1} kpc for the observed pair 1343+2640A/B and 50 h^{-1} kpc for model). The tight theoretical correlation is supported by the observed values, with none of the observed W_0 locii for uncontaminated lines being inconsistent with the theoretical result, and with the potentially contaminated lines also being in reasonable agreement. As Charlton et al. (1997) note, a larger data set would be desirable.

We also consider the pair 0307−1931/32 at $S = 231$ h^{-1} kpc separation. Figure 15*a* shows the distribution of $|W_a - W_b|$ versus max (W_a, W_b) for 0307−1931/32, analogous to Figure 2*b* of Paper III for 1343+2640A/B. (Since we could not reanalyze this spectrum, we do not attempt to remove Lyα potentially contaminated by superimposed metal lines.) In general, the points in Figure 15*a* must lie below the $|W_a - W_b| = \max(W_a, W_b)$ diagonal, and the farther they fall from this line, the more homogeneous they are. Unlike the idealized models of Charlton et al. (1995), with analogous results presented in their Figure 1, there is still a close agreement between the observed wide-pair locus and the locus predicted for very close pairs (see, e.g., Fig. 5 of Charlton et al. 1997). We draw no interesting conclusion from this comparison.

The results for $|W_a - W_b|$ versus max (W_a, W_b) are more interesting for the KP triplet, as shown in Figure 15*b*. Because of the density of points, we do not present error bars, which are typically much less than 0.1 Å (hence about the size of the point symbols). Each point represents a Lyα forest line coincidence ($\Delta v < 200$ km s^{-1}) free of probable metal-line contamination (from systems at different redshifts) and without associated metal lines (from the same redshift system). This figure's distribution of points seems to fall at least as far below the $|W_a - W_b| = \max(W_a, W_b)$ line as those in Figure 5 of Charlton et al. (1997) for the close pair 1343+2640A/B. The points flagged by the three-legged crosses denote absorbers spanning all three KP sight lines (with $W_0 > 0.4$ Å). While this minimum W_0 selection guarantees that the points sit at least 0.4 Å below the $|W_a - W_b| = \max(W_a, W_b)$ line, it is significant that those objects that span all three sight lines appear to be the most uniform of any in the S/N ≥ 3.5, uncontaminated, Lyα-only sample. Separate from this selection effect, one can still state that the most homogeneous, strong lines also span all three

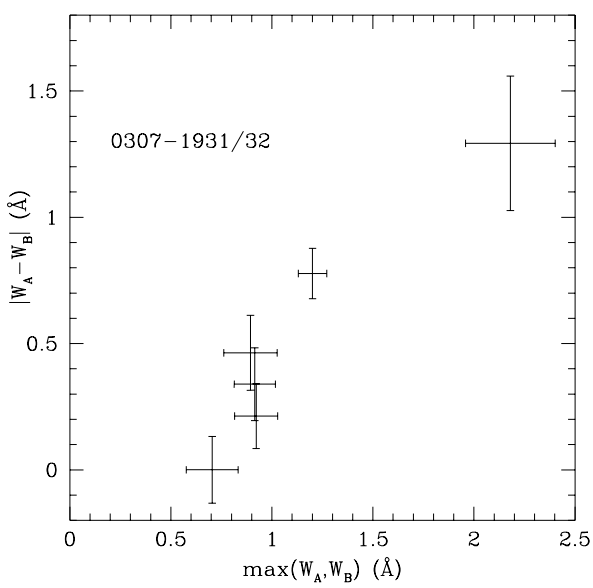

FIG. 15*a*

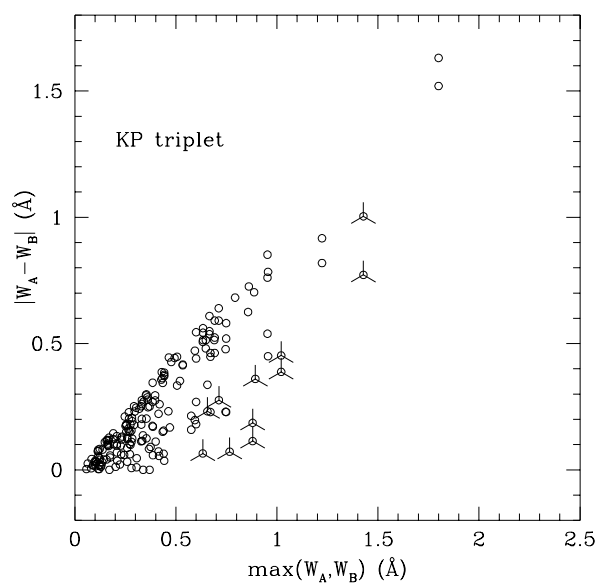

FIG. 15*b*

FIG. 15.—(*a*) Comparison of line strengths within the Lyα forest of 0307−1931/32 (proper separation of 231 h^{-1} kpc) showing the difference in rest equivalent width $|W_A - W_B|$ for hits within 200 km s^{-1} vs. the strength of the stronger of the two lines. All Lyα line detections stronger than 3.5 σ are considered. Error bars are ± 1 σ. (*b*) Similar to (*a*), but for the KP triplet, taken one QSO pair at a time. Because of the density of points, no error bars are shown, but errors are much smaller than in (*a*), typically the size of the round symbols. The tripods mark lines involved in objects that span all three sight lines.

sight lines. This argues that these compose a well-defined class of objects and are not produced by random superposition. Furthermore, the uniformity in W_0 argues against these pairs being produced simply by clustering of smaller objects and indicates some coherence in the H I distribution on 0.5–0.8 h^{-1} kpc scales, such as sheets of gas, and not filaments.

4.8.7. *Distribution of $N_{\rm H\,I}$ among Anticoincident Lines (Charlton et al. 1995, 1997)*

Charlton et al. (1995) present the shape of the distribution f of column densities of lines *not* participating in hits within close pairs (N_{ac}) as a sensitive discriminator of absorber shape, e.g., disks versus spheres. This difference appears most strongly at the high $N_{\rm H\,I}$ end, where spheres show a sharp cutoff at a position dependent on the size of the clouds relative to S, whereas disks show a gradual reduction at all $N_{\rm H\,I}$ values, with only a slow change in the slope of log (f) versus log (N_{ac}). Charlton et al. suggest this test for a set $N_{\rm H\,I}$ cutoff in the line strength of the "missing" line. (Lines weaker than this can produce anticoincidences in neighboring sight lines.) We impose a cutoff $W_0 > 0.3$ Å, which corresponds to log ($N_{\rm H\,I}$ cm^{-2}) = 14.16 for $b = 30$ km s^{-1}. One then studies the distribution f of $N_{\rm H\,I}$ in the remaining line. We plot this function in Figure 6 for 0307−1931/32, 1517+2356/57, and the KP triplet. The distributions are renormalized to have the same number of lines at log ($N_{\rm H\,I}$ cm^{-2}) = 13.5, below which the sample is grossly incomplete. (1343+2640A/B has so few anticoincident lines that f is poorly defined.) This results in a total of 18 anticoincident lines in 0307−1931/32, 17 in 1517+2356/57, and 41 from sight-line pairs among the KP triplet.

The behavior of the anticoincident $N_{\rm H\,I}$ distribution in Figure 16 differs from that in Figure 2 of Charlton et al. The observed distribution f is broader and present at stronger $N_{\rm H\,I}$ for closer QSO pairs than in wider pairs, the opposite of the behavior predicted for spheres or disks. It is less discrepant with the more gradual increase in strength with increasing S found in disks. It is also less discrepant with the behavior of lines in simulations (Fig. 7 of Charlton et al. 1997) but is not in good agreement.

This puzzling behavior may simply be due to small number statistics. The critical difference in the shape of f for disks versus spheres occur over the high $N_{\rm H\,I}$ tail containing only 1%–10% of the lines. We need several times as many data to adequately test these predictions.

4.9. *Metal-Line Absorber Clustering*

The data on these five QSOs, especially the KP triplet, now includes enough space probed with closely spaced sight lines through the absorber distribution that one can begin to ask how C IV absorbers cluster in space, as measured by the cross-correlation of the absorber distribution between sight lines, as opposed to autocorrelating the distribution along single sight lines. The latter approach, which has been presented in many works, carries with it the danger that spatial clustering signals may be mixed with velocity correlations due to internal velocity splittings within isolated absorbing objects. This is circumvented in the case of sight-line cross-correlations; multiple absorber redshifts per object simply are reflected in an increase in the number of correlation pairs equally on all scales, not just for small separations such as those internal to an absorber. Such an increase in pairs cancels in the two-point correlation function ξ.

Figure 17 shows the number of cross-correlation pairs, binned in relative velocity (as in Fig. 6 for Lyα clouds) but in this case for all C IV absorbers identified for the KP triplet. The solid curve shows all such C IV pairs and the dotted

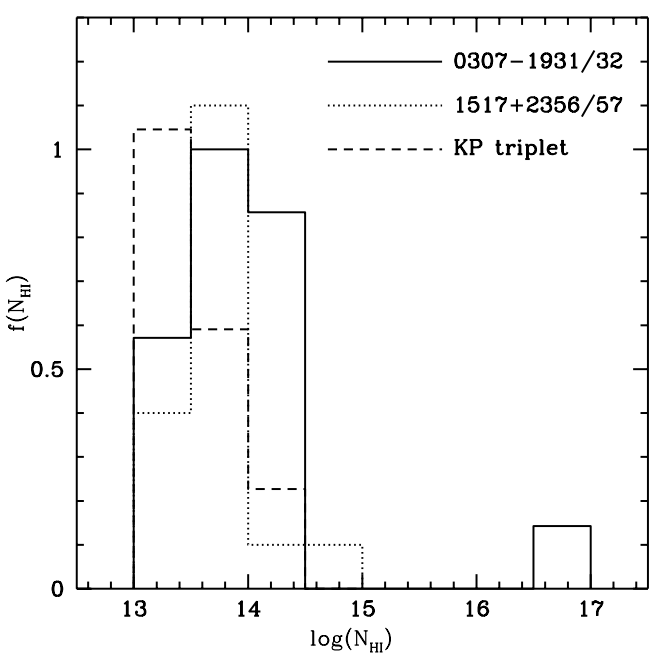

FIG. 16.—Distribution of anticoincident lines (all lines stronger than 3.5 σ detections, but missing a neighbor stronger than $W_0 = 0.3$ Å within 200 km s^{-1} in the adjacent sight line). In the case of the KP triplet, each sight-line pair is considered individually, rest equivalent width has been converted to $N_{\rm H\,I}$ by assuming thermal widths of $b = 30$ km s^{-1}, and the distributions are normalized to be equal at log ($N_{\rm H\,I}$ cm^{-2}) = 13.5.

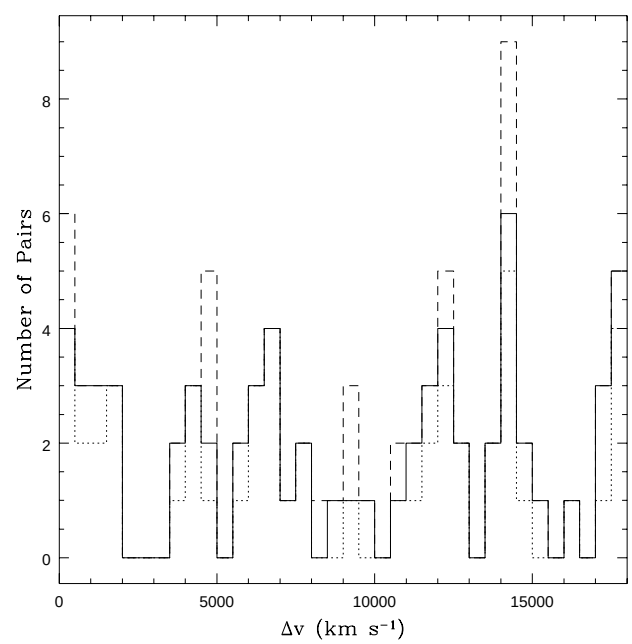

FIG. 17.—C IVλ1548 absorber two-point velocity cross-correlation function for three different samples, plotted as a histogram of the number of pairs in 200 km s^{-1} bins vs. velocity difference Δv. The dotted bars indicate only those pairs composed of "definite" or "probable" C IVλ1548 absorbers among the three KP triplet sight lines, while the solid bars indicate pairs including "possible" KP triplet absorbers. The dashed bars include pairs from Q1517+2357/1517+2356 and Q0307−1931/0307−1932 (Shaver & Robertson 1983).

curve only those pairs involving both absorbers in the "probable" or "definite" categories, with detected C IV λ1548. The dashed curve in Figure 17 shows the same information, but for all C IV absorbers in the LB pair, the Q0307−195 pair, and the KP triplet (where each sight line is cross-correlated only with its partners in the same pair or triplet). Q1343+2640 is excluded since its separation may be smaller than the size of individual C IV galaxy cross sections, and Q0107−025 is at much lower redshift. The first 500 km s^{-1} bin in Figure 16 shows more pairs than any other except one (which shows nine at 14,000 km s^{-1} < Δv < 14,500 km s^{-1}). Furthermore, the first 2000 km s^{-1} interval shows more pairs than any other 2000 km s^{-1} interval in the entire Δv range. The average number of pairs per 500 km s^{-1} bin is 1.97, so the Poisson probability of the first bin having the observed six pairs (or more) is 1.5%, and the probability of the first four bins having the observed 15 pairs is also 1.5%. The probability of the second observation given the first is 14%, so the signal in the first bin is most significant, as long as we consider the first bin to be uniquely special, a priori. (If we do not, there are approximately 100 such equivalent bins, so the probability of such a random occurrence in some bin is nearly unity.) There is no obvious substructure in Δv within the first bin, but the contribution from the triplet is due to a single cluster at $z \approx 2.243$. Specifically, the signal arises in the LB pair at $\Delta v = 233$ km s^{-1} and $z = 0.7376$, in the Q0307−195 pair at $\Delta v = 306$ km s^{-1} and $z = 2.0337$, and in the KP triplet at $\Delta v = 100$, 261, 360, and 490 km s^{-1} at redshifts 2.2419, 2.2431, 2.2437, and 2.2451, respectively. This is the most statistically significant signal ever seen showing that C IV clustering exists on small scales within sight-line cross-correlations. It corresponds to a two-point correlation function $\xi = 2.05^{+1.82}_{-1.21}$ (68% confidence limits, as for the Ly$\alpha\xi$ in § 4.3), over proper separations of 220–720 h^{-1} kpc, approximately (for $q_0 = 1/2$), neglecting the distance component along the line of sight. Including this component, it corresponds to distances up to about 1.05 h^{-1} Mpc. With $q_0 = \frac{1}{2}$, this would correspond to velocity differences as large as 690 km s^{-1} in the Hubble flow.

While the statistical significance of this C IV cross-correlation result is not large, it should be compared to the single–sight line auto-correlation function (Sargent, Steidel, & Boksenberg 1988), which shows, for single–sight line splittings of 200 km s^{-1} < Δv < 600 km s^{-1}, a two-point function of variously $\xi = 5.7 \pm 0.6$ or $\xi = 11.5 \pm 1.3$ depending on whether or not a cutoff of $W_0 = 0.15$ Å is imposed on C IV λ1548 (in the second case), with both cases excluding lines within 5000 km s^{-1} of the QSO emission redshift. The first case is inconsistent with our data at the 2 σ level; the second is even more inconsistent. Our sample is more heterogeneous, not being defined by a specific cutoff on W_0 or Δv with respect to the emission redshift, but of the 38 C IV λ1548, only eight have $W_0 < 0.10$ Å and 14 have $W_0 < 0.15$ Å. None of the lines contributing to the ξ signal are within 5000 km s^{-1} of the emission redshift. Our sample is closer to the second sample from Sargent et al. (1988) and is inconsistent with the results obtained from it. This suggests that some of the power in ξ seen by Sargent et al. is not caused by spatial clustering, but by internal motion within absorbers.

Measuring structure on larger scales by cross-correlation of sight lines is interesting and unprecedented for unbiased samples (except for the full-sky cross-correlational study of Crotts 1985 and the recent paper of Williger et al. 1996). Tytler et al. (1987), Heisler, Hogan, & White (1989), and Quashnock, Vanden Berk, & York (1996) suggest structure up to 100 h^{-1} Mpc comoving scales in their studies of single–sight line metal-line autocorrelations. This is consistent with the power we see at $\Delta v \approx 14{,}000$ km s^{-1}, but we would need a larger sample to be sure. In general, however, the cross-correlational technique is most interesting on smaller scales, where internal velocities may be important. (Or it may be interesting for obtaining very dense, random samples, as suggested for the Lyα forest in § 4.2, or for studying certain preselected anomalies, e.g., in the region around a close damper Lyα absorber pair [Francis et al. 1996] and the $\approx$100 Mpc absorber cluster in the Tololo QSO sample near 1037−27 [Ulrich & Perryman 1986; Jakobsen et al. 1986; Jakobsen, Perryman, & Christiani 1988; Robertson 1987; Cristiani, Danziger, & Shaver 1987; Sargent & Steidel 1987; Jakobsen & Perryman 1992; Dinshaw & Impey 1996].) We are in the process of acquiring more such QSO pair data to study the clustering properties of C IV absorbers on Mpc scales.

5. DISCUSSION

Returning to the clustering behavior of Lyα forest, one should note that in both their contributions to large-scale and small-scale structure, the $W_0 > 0.4$ Å Lyα sample and weaker lines differ in their behavior. Both in the small-scale two-point correlation function, and in the presence of large-scale underdensities, the $W_0 > 0.4$ Å sample reveals more significant features (see Figs. 6 and 7) that are washed out in larger, lower W_0 cutoff samples. This might lead one to believe that these two populations are distinct. There is some evidence contradicting this, however, in that our original data from Q1343+2640A/B includes some lines weaker than $W_0 = 0.4$ Å, and these also show signs of being associated with large absorbers. Whereas the entire S/N > 3.5 σ sample shows 11 hits and four misses, the $W_0 > 0.4$ Å subsample (see Table 8), once removed, leaves $N_h = 3$ and $N_m = 4$ for the remaining $W_0 < 0.4$ Å lines (typically 0.2 Å < W_0 < 0.4 Å, albeit not complete to $W_0 =$ 0.2 Å). This implies that these weaker absorbers have a median predicted radius $R = 63$ h^{-1} kpc (assuming unclustered, constant-radius spheres, and with 95% confidence bounds 35 h^{-1} kpc $< R <$ 146 h^{-1} kpc), which, while possibly smaller than the size in the $W_0 > 0.4$ Å sample, still indicates absorbers that are much larger than the visible sizes of galaxies and are within about a factor of 2.5 of the size of low column density H I galaxy halos at low z (Lanzetta et al. 1995). Compared to C IV absorbers as well (Steidel & Sargent 1991; Paper I), these are still large absorbers.

It is apparent, however, that the $W_0 > 0.4$ Å absorbers are large enough, at least in two dimensions, to span the gap between the triplet sight lines, while the weaker lines may not. It is interesting then, at this point, to examine the differences between those objects spanning all three sight lines and those $W_0 > 0.4$ Å clouds that do not. Of the five $W_0 >$ 0.4 Å triple-hit objects, we note that two are associated with C IV absorbers, while another probably is. Furthermore, of the two that are not, one occurs at the same redshift of KP 79, the $z = 2.183$ QSO some 1.5 h^{-1} Mpc away from the triplet sight lines (in proper coordinates). In the rest of the $W_0 > 0.4$ Å Lyα sample, only 17 out of 144 absorbers have detected C IV absorption. These two populations are dis-

crepant at the 3 σ level. Absorbers with strong C IV may be associated with larger objects than strong Lyα absorbers without strong C IV. The average velocity spacing between these groups of lines corresponds to 35 h^{-1} Mpc (with $q_0 = \frac{1}{2}$), roughly the scale of sheets between the voids in the $z \approx 0$ galaxy distribution. This correspondence echoes a suggestion long ago by Oort (1981) that Lyα absorbers correspond to superclusters. These data suggest something rather different, that a small subsample may detect sheetlike structures on such scales. It is not clear to us that such structures are evident the current numerical simulations of the Lyα forest, nor is it clear that they necessarily should be given the small volumes simulated by these models.

6. CONCLUSIONS

The strongest results indicated here are that the redshift correspondences between Lyα absorbers in closer sight line pairs persist for proper separations up to 0.5–0.8 h^{-1} Mpc for lines stronger than $W_0 = 0.4$ Å. There is an indication that the shape of the clouds responsible for this signal is not very elongated (aspect ratio $a < 4$, probably). There is weaker evidence, however, of expansion of these clouds with the Hubble flow in a way consistent with sheets or disks and evidence of sheets of relatively uniform gas density spanning 0.5–0.7 h^{-1} Mpc transverse separations. This suggests that at least a large fraction of high column density absorbers arise in expanding sheets. While we do not have such a measurement for weaker lines, there is data from Q1343+2640A/B (Paper I) that indicates that 0.2 Å $\lesssim W_0 <$ 0.4 Å clouds are probably at least 35 h^{-1} kpc in radius (95% confidence) and are probably closer to 63 h^{-1} kpc in radius, still very large compared to the luminous size of galaxies and, probably, C IV absorbers.

Despite the strong leverage in redshift with the inclusion of the LB pair and Q0107−0234/0107−0235 and Q1026−0045A/B, the evidence for any evolution on the size of $W_0 > 0.4$ Å Lyα absorbers is not significant.

Our theoretical models to which the small-scale structure data are compared here are intentionally crude. Detailed comparison with numerical models incorporating hydrodynamics and ionization, as well as gravity, at high redshift lead to poor agreement in some cases and better in others, perhaps because of absence of clustering power on scales comparable to the simulation box size. It would appear that our current data may be inconsistent with the long filaments ($a \geq 10$) that are produced in these models, but detailed comparison of model and observation on as close a corresponding, quantitative basis as possible are required to minimize the systematic errors involved in analyzing the two forms of data differently.

In this paper, C IV absorbers are shown to cluster in space as well as velocity on small scales ($\lesssim 1$ h^{-1} Mpc) for the first time, and while this signal is weak, it seems inconsistent with the same sort of measurement via single–sight line two-point correlation measurements. The simplest explanation for this difference is additional splittings within the absorbers themselves on velocity scales up to 600 km s^{-1}. This is hard to explain as the internal motions within galaxy halos (Sargent et al. 1988) but may indicate large velocity flows due to nongravitational acceleration of gas, perhaps by shocks caused by star formation processes,

With the exception of strong clustering seen on sub-Mpc scales and some indication of large, smooth sheets of gas, none of the new conclusions from these data is stronger than about 3 σ, and many more indications are less certain than this. This calls for more QSO sight-line pairs on scales of separations less than about 1 h^{-1} Mpc proper separation. Since most of these will be at lower redshift than even the KP triplet, it also calls for UV-sensitive instrumentation on large telescopes. (However, if the behavior of only stronger lines is nonrandom, higher S/N data will reveal no new effects.) In the long term, both practical developments seem likely, but they are the limiting factors at present.

We thank Richard Green for providing the Lyα forest data on LB 9605 and LB 9612 published in Elowitz et al. 1995. We very much appreciate the advice of Donald York in interpreting the complex absorption line spectra of these objects. We acknowledge the forethought of Foltz et al., who arranged for the *HST* observations of LB 9605 and LB 9612. We would like to acknowledge support of the NSF under grant AST 90-22586 and express our gratitude to the David and Lucile Packard Foundation for A. C.'s fellowship.

REFERENCES

Bajtlik, S., Duncan, R. C., & Ostriker, J. P. 1988, ApJ, 327, 570
Bechtold, J. 1994, ApJS, 91, 1
Bechtold, J., Crotts, A. P. S., Duncan, R. C., & Fang, Y. 1994, ApJ, 437, L79 (Paper II)
Carswell, R. F., & Rees, M. J. 1987, MNRAS, 224, 13
Cen, R., Miralda-Escudé, J., Ostriker, J. P., & Rauch, M. 1994, ApJ, 437, L9
Cen, R., & Simcoe, R. A. 1997, ApJ, 483, 8
Charlton, J. C., Anninos, P., Zhang, Y., & Norman, M. L. 1997, ApJ, 485, 26
Charlton, J. C., Churchill, C. W., & Linder, S. M. 1995, ApJ, 452, 81
Cristiani, S., Danziger, I. J., & Shaver, P. A. 1987, MNRAS, 227, 639
Crotts, A. P. S. 1985, ApJ, 298, 732 (erratum 305, 581)
———. 1987, MNRAS, 228, 41P
———. 1989, ApJ, 336, 550
———. 1998, in preparation
Crotts, A. P. S., Bechtold, J., Fang, Y., & Duncan, R. C. 1994, ApJ, 437, L79 (Paper I)
Crotts, A. P. S., Burles, S., & Tytler, D. 1997, ApJ, 489, L7
Dinshaw, N., Foltz, C. B., Impey, C. D., Weymann, R. J., & Morris, S. L. 1995, Nature, 373, 223
Dinshaw, N., & Impey, C. D. 1996, ApJ, 458, 73
Dinshaw, N., Impey, C. D., Foltz, C. B., Weymann, R. J., & Chaffee, F. H. 1994, ApJ, 437, 87
Dobrzycki, A., & Bechtold, J. 1991, ApJ, 377, L69
Duncan, R. C., Ostriker, J. P., & Bajtlik, S. 1989, ApJ, 345, 39
Elowitz, R. M., Green, R. F., & Impey, C. D. 1995, ApJ, 440, 458
Fang, Y., & Crotts, A. P. S. 1994, BAAS, 185, 13.03
Fang, Y., Duncan, R. C., Crotts, A. P. S., & Bechtold, J. 1996, ApJ, 462, 77 (Paper III)
Foltz, C. B., Weymann, R. J., Röser, H.-J., & Chaffee, F. H., Jr. 1984, ApJ, 281, L1
Fernández-Soto, A., Barcons, X., Carballo, R., & Webb, J. K. 1995, MNRAS, 277, 235
Francis, P. J., et al. 1996, ApJ, 457, 490
Heisler, J., Hogan, C. J., & White, S. D. 1989, ApJ, 347, 52
Hewitt, A., & Burbidge, G. 1993, ApJS, 87, 451
Jakobsen, P., & Perryman, M. A. C. 1992, ApJ, 392, 432
Jakobsen, P., Perryman, M. A. C., & Cristiani, S. 1988, ApJ, 326, 710
Jakobsen, P., Perryman, M. A. C., Di Serego Alighieri, S., Ulrich, M. H., & Macchetto, F. 1986, ApJ, 303, L27
Katz, N., Hernquist, L., Weinberg, D. H., & Miralda-Escudé, J. 1996, ApJ, 457, 51
Lanzetta, K. M., Bowen, D. B., Tytler, D., & Webb, J. K. 1995, ApJ, 442, 538
Loeb, A., & Eisenstein, D. J. 1995, ApJ, 448, 17
Lu, L., Wolfe, A. M., & Turnshek, D. A. 1991, ApJ, 367, 19
Miralda-Escudé, J., Cen, R., Ostriker, J. P., & Rauch, M. 1996, ApJ, 471, 582
Oort, J. H. 1981, A&A, 94, 359
Quashnock, J. M., Vanden Berk, D. E., & York, D. G. 1996, ApJ, 472, L69
Rauch, M., & Haehnelt, M. G. 1995, MNRAS, 275, 76
Rauch, M., et al. 1992, ApJ, 390, 387
Robertson, J. G. 1987, MNRAS, 227, 635

Sargent, W. L. W., & Steidel, C. C. 1987, ApJ, 322, 142
Sargent, W. L. W., Steidel, C. C., & Boksenberg, A. 1988, ApJS, 68, 359
Shandarin, S. F., Melott, A. L., McDavitt, K., Pauls, J. L., & Tinker, J. 1995, Phys. Rev. Lett., 75, 7
Shaver, P. A., & Robertson, J. G. 1983, ApJ, 268, 57
Smette, A., Robertson, J. G., Shaver, P. A., Reimers, D., Wisotzki, L., & Koehler, T. 1995, A&AS, 113, 199
Smette, A., et al. 1992, ApJ, 389, 39
Steidel, C. C., & Sargent, W. L. W. 1991, AJ, 102, 1610
Tytler, D., Boksenberg, A., Sargent, W. L. W., Young, P., & Kunth, D. 1987, ApJS, 64, 667
Ulrich, M. H., & Perryman, M. A. C. 1986, MNRAS, 220, 429
Williger, G. M., Hazard, C., Baldwin, J. A., & McMahon, R. G. 1996, ApJS, 104, 145
Zhang, Y., Anninos, P., & Norman, M. L. 1995, ApJ, 453, 57

Note added in proof.—Q1026−0045A/B (P. Petitjean, J. Surdej, A. Smette, P. Shaver, J. Mücket, & M. Remy, A&A, 334, L45 [1998]), like Q1517+2357/1517+2356, are two low-redshift QSOs in a close pair observed by the FOS on *HST* using the G270H grating. These data are now included in Table 8, Figure 10, and the results of this section. We have reanalyzed the linelist and spectra of this pair, imposing the same $W_0 = 0.4$ Å cutoff as for the other pairs, which coincidentally results in a somewhat smaller R value than do the W_0 cutoffs used by Petitjean et al. Nonetheless, adopting their values does not change the results of § 4.4 significantly.